The Structure of the Neutron-Rich ^{22}O and ^{23}F Nuclides

Luke Tetley

Doctor of Philosophy

University of York
Physics

August 2022

Abstract

This thesis reports on the measurements of the nuclear structure of the light neutron-rich ^{22}O and ^{23}F nuclides. The excited states of ^{23}F were studied via a one-neutron removal reaction, using the high-resolution γ-ray detector array, GRETINA, coupled to the S800 spectrometer at NSCL. Several new transitions have been observed in the γ-ray spectrum and by performing γ-γ coincidence analysis, an extended level scheme has been built for ^{23}F. Additionally, the relative populations of the excited states and branching ratios were studied using detailed Monte Carlo GEANT4 simulations and the spin assignments were determined through the analysis of the γ-ray angular distributions. These findings were compared to the calculations from the phenomenological USD-type interactions, where it was found that the USDB calculations were the most consistent with the experimental data on the structure of ^{23}F.

The experiment to measure the electromagnetic transition rates in ^{22}O was carried out at ANL, using the GRETINA array coupled to the FMA. A novel ^{10}Be target was developed in order to populate the excited ^{22}O recoils via the ^{14}C(^{10}Be,2p)^{22}O fusion-evaporation reaction. The molecular plating technique was used to prepare the ^{10}Be target on a thin platinum backing, however a low deposition yield of about 20% significantly reduced the ^{10}Be content to be between 22-32 μg/cm^2. The measured rates of the ^{22}O recoils were too low for the DSAM technique, with a potential 3199 keV transition of 14 $\pm$ 5 counts being observed in a single experimental setting. The analysis of the stronger exit channels of the fusion-evaporation reaction, namely ^{21}O and ^{22}Ne, suggested that the low rates of the ^{22}O could be primarily attributed to the low recoil acceptance into the FMA.

Contents

Abstract **3**

List of Figures **9**

List of Tables **12**

Acknowledgements **13**

Declaration **15**

1 Introduction **17**

1.1 Descriptions of the Nuclear System 18

1.1.1 The Nuclear Shell Model 19

1.1.2 Shell-Model Formalism 22

1.1.3 USD-Type Interactions 23

1.1.4 Interactions from Chiral Effective Field Theory 24

1.1.5 Ab Initio Approaches 26

1.2 Light Neutron-Rich Nuclei 28

1.2.1 The Oxygen Isotopic Chain 29

2 Background **31**

2.1 Gamma Decay 31

2.1.1 Transition Probabilities and Lifetimes of Nuclear States 33
2.2 Radiation Interaction with Matter 35
2.2.1 Interactions of Heavy Ions 35
2.2.2 Interactions of γ rays 37
2.3 γ-ray Spectroscopy 42
2.3.1 Relativistic Doppler Shift 44
2.4 Lifetime Measurements 46
2.4.1 Doppler Shift Attenuation Method 47

3 Nuclear Structure of ^{23}F Following a One-Neutron Removal Reaction 50

3.1 Experimental Setup 51
3.1.1 A1900 Fragment Separator 52
3.1.2 S800 Spectrograph 53
3.1.3 GRETINA 56
3.1.4 Germanium Detectors 58
3.1.5 GRETINA Tracking 60
3.2 Data Analysis 61
3.2.1 Particle Identification 62
3.2.2 GRETINA Energy Calibration and Efficiency 64
3.2.3 Doppler Correction 66
3.2.4 γ-ray Spectrum Analysis 69
3.2.5 γ - γ Coincidence Analysis 71
3.2.6 γ-ray Angular Distributions 73
3.2.7 GEANT4 Simulations 77
3.2.8 Simulation Spectra Fit 80

3.2.9 Simulation Angular Distribution Analysis 82
3.3 Results 84
3.3.1 γ-ray Spectroscopy Results 84
3.3.2 γ - γ Coincidence Results 85
3.3.3 γ-ray Angular Distribution Results 90
3.3.4 Summary 94
3.4 Discussion 97
3.4.1 Previous Experimental Works 97
3.4.2 Shell-Model Calculations 100
3.4.3 The 2909 keV, 3826 keV, 4908 keV and 5534 keV States 103
3.4.4 The 2241 keV, 3964 keV States and 4065 keV States 105
3.4.5 The 3368 keV, 4624 keV and 7762 keV States 106
3.4.6 Summary 107

4 Measurement of the Electromagnetic Transition Rates of ^{22}O 109

4.1 Experimental Details 110
4.1.1 ATLAS 113
4.1.2 GRETINA 114
4.1.3 FMA 114
4.2 Development of a Novel ^{10}Be Target 116
4.2.1 Extraction and Isolation of ^{10}Be 117
4.2.2 Target Development 117
4.2.3 Final Target Preparation 121
4.3 Results 123
4.3.1 Search for ^{22}O 126

4.4 Discussion 129

4.4.1 Target Composition 129

4.4.2 ^{22}Ne Discussion 131

4.4.3 ^{21}O Discussion 134

4.4.4 Future Work 137

4.4.5 Summary 138

5 Conclusion **139**

Bibliography **141**

List of Figures

1.1 Experimental and SEMF binding energy difference 19

1.2 Single-particle states for the Woods-Saxon and spin-orbit potentials 21

1.3 Hierarchy of nuclear forces from chiral EFT 25

1.4 Neutron-rich nuclei and the oxygen anomaly 29

2.1 Stopping power curve of helium ions in silicon 37

2.2 Schematic illustration of the γ-ray interaction processes 39

2.3 Contributions of each interaction process to the γ-ray attenuation 40

2.4 Polar plot of the γ-ray scattering angle probabilities 41

2.5 Annotated sketch of a γ-ray spectrum 42

2.6 Relativistic Doppler shift plots 45

2.7 Effective regions of lifetime measurement methods 47

2.8 Doppler shift attenuation method (DSAM) diagrams 48

3.1 Shell structure of ^{23}F 51

3.2 A1900 fragment separator 53

3.3 S800 and focal plane detectors 54

3.4 Schematic drawing of the CRDCs 55

3.5 Sketch of GRETINA modules and crystals 57

3.6 Photograph of open hemisphere of GRETINA 57

3.7 Sketch of electronic band structure in semiconductors 59

3.8 Illustration of an n-type HPGe coaxial detector 60

3.9 Incoming particle identification plot 62

3.10 Dispersive corrections on S800 63

3.11 Outgoing particle identification plot 64

3.12 ^{56}Co and ^{152}Eu source measurements for GRETINA calibration 65

3.13 GRETINA calibration quality 65

3.14 GRETINA relative efficiency curve 66

3.15 Lab-frame γ-ray spectrum 68

3.16 Doppler corrected γ-ray spectrum 68

3.17 Gaussian peak fitting example 70

3.18 γ-γ coincidence matrix for ^{23}F 72

3.19 γ-γ coincidence analysis example 72

3.20 Momentum distribution gating 75

3.21 Division of angular detection range 76

3.22 Simulated GRETINA geometry 77

3.23 Simulated GRETINA efficiencies 78

3.24 GRETINA energy resolution fit 79

3.25 Simulated lab-frame and Doppler corrected background 80

3.26 Simulation fit for total γ-ray spectrum 81

3.27 Simulation fit for angular intervals 83

3.28 First set of γ-ray coincidence spectra 86

3.29 Second set of γ-ray coincidence spectra 87

3.30 The γ-ray angular distributions 92

3.31 New ^{23}F level scheme 95

3.32 Previous experimental ^{23}F level schemes 98

3.33 Comparison of relative populations to previous measurement 99

3.34 Theoretical excited states for the USD-type Hamiltonians 101

4.1 Experimental and theoretical B(E2) values of oxygen nuclei 110

4.2 Schematic drawing of the experimental setup at ATLAS 111

4.3 PACE4 fusion-evaporation reaction cross sections 112

4.4 ATLAS floor plan 113

4.5 DOSTAL DOSY droplet deposition device 119

4.6 Coffee ring residue formation 120

4.7 Molecular plating chamber schematic 122

4.8 Final target images 123

4.9 ANL source spectra 125

4.10 ANL GRETINA energy and efficiency calibrations 125

4.11 Time gatings and IC gatings for ^{22}O 126

4.12 ^{22}O mass gatings 127

4.13 ^{22}O Doppler corrected γ-ray spectrum 128

4.14 ^{22}Ne PID plots 132

4.15 Doppler corrected ^{22}Ne γ-ray spectrum 132

4.16 ^{22}Ne recoil kinematics 134

4.17 ^{21}O atomic number gate 135

4.18 ^{21}O mass gates 135

4.19 Doppler corrected ^{21}O γ-ray spectrum 136

4.20 Comparison of ^{21}O and ^{22}O recoil kinematics 136

List of Tables

2.1 Reduced forms of the γ-decay rate formulae 34

3.1 The γ-ray energy and relative intensity measurements 85

3.2 The γ-ray coincidences summary table 88

3.3 Summary of the γ-ray angular distribution fit parameters 93

3.4 Full summary of the ^{23}F measurements 96

3.5 Experimental measurements compared to shell-model calculations 102

3.6 Comparison of shell-model calculations 103

4.1 Major experimental run settings 124

4.2 RBS target composition results 130

4.3 PACE4 ^{22}Ne reaction pathways 131

Acknowledgements

There are number of people I would like to acknowledge, without whom this work would not have been possible. First and foremost, I would like to thank my supervisor Marina Petri for providing the opportunity to work on an interesting set of projects. The weekly meetings and guidance were invaluable throughout the PhD. I would also like to express my gratitude to all of the collaborators I have worked with, who so freely gave their time and advice when it was needed. In particular I would like to acknowledge Emilio Andrea Maugeri for offering his wealth of experience in the target preparation techniques, as well as the opportunity to work at the lab in PSI. I look back fondly on those times in the lab, out of my depth and trying to not break the tiny carbon foils.

I would also like to extend additional thanks to the members of the nuclear physics group at York, both past and present. The weekly meetings and discussions have given me a much broader sense of the field. A special thanks also goes out to Sebastian Heil and Ryo Taniuchi, whose help particularly in the early stages of the PhD was invaluable to getting started with the analysis myself.

On a more personal note, I would like thank the members of the group who came to the lockdown discord and drinks evenings, the laughs made a tough time much easier. Of course a huge thanks goes to my parents, as well as Matty and Lauren and the rest of my family, for providing an ever open door and a comfortable space to decompress during the difficult times. The final and biggest thanks go to my wonderful partner Nettie, whose continued belief and support helped drive me across the finish line and will always be appreciated.

Declaration

I declare that this thesis is a presentation of original work and I am the sole author. This work has not previously been presented for an award at this, or any other, University. All sources are acknowledged as References.

Chapter 1

Introduction

The atomic nucleus is at the heart of the atoms from which all of the visible matter in the known universe is comprised; from everything here on Earth, to the stars and planets throughout all of the galaxies. Though small in size, with diameters of 100,000 times less than the atoms themselves, the nucleus contains 99.9% of the atomic mass and drives some of the most far-reaching and cataclysmic phenomena in existence; from stellar evolution, to supernovae and the origin of the elements. The atomic nucleus itself is a complex quantum many-body system, and constitutes an ideal laboratory for the study of the fundamental interactions and dynamics of the elementary particles, from which emerge the basic structures of matter.

Since the atomic nucleus was discovered over a century ago in Rutherford's pivotal α-particle scattering experiment [1], the study of nuclear physics as a field has come a long way. Indeed, far from the charged, point-like, featureless particles they were originally understood to be, it is now known that they are quantum mechanical objects with intricate structures, that are comprised of protons and neutrons, which themselves are made up of quarks bound by the force-carrying gluons. It is from these underlying interactions between the elementary components of matter that the complexity emerges, with 118 possible atomic elements and over 3100 known isotopes. One of the overarching goals of the field of nuclear structure as a whole, is to construct a coherent framework in which the properties of these nuclei, their reactions and decays, can all be consistently described [2].

1.1 Descriptions of the Nuclear System

To that end, throughout the history of the field, a number of models and frameworks have been developed which present a simplified picture of the nuclear system, yet still contain the necessary physics to make predictions that are grounded in reality and provide some physical insight. What follows, will be a brief tour through some of the noteworthy models, which will not only put into context some of the more recent developments, such as the ab initio many-body methods, but will also serve to contextualise the work presented within this thesis.

The liquid drop model was one of the earliest nuclear models to be developed, framing the nuclear system as a small drop of high-density, incompressible fluid, to understand the nuclear binding energy; acknowledging that the nucleons near the surface would be less bound by the nuclear force than those in the bulk [3]. For such a simplified picture the liquid drop model has proved remarkably insightful, describing a range of phenomena from the so called valley of β stability, to the tight binding of the iron-group isotopes, as well as nuclear fission. Within this picture, the semi-empirical mass formula can be derived, parameterising the five key contributions to the nuclear binding energy, in terms of the proton and neutron numbers, as shown in equation 1.1.

$$E_b = a_V A - a_S A^{2/3} - a_C \frac{Z(Z-1)}{A^{1/3}} - a_A \frac{(A-2Z)^2}{A} \pm \delta(A,Z) \tag{1.1}$$

The first term of the semi-empirical mass formula represents the attractive nuclear forces that the nucleons experience when interacting within the bulk of the nucleus, with the second term correcting for the surface effects; reducing the overall binding energy as the nucleons on the surface have fewer neighbouring nucleons to interact with. Accordingly, the first and second terms are proportional to the nuclear volume and surface area, respectively. The third term accounts for the Coulomb repulsion between the protons, thus subtracts from the total binding energy. An additional reduction is introduced in the penultimate term, for nuclei with unequal numbers of protons and neutrons, arising from the Pauli exclusion principle. The final term accounts for the pairing effect, where nucleons of even numbers tend to pair granting additional binding energy, so that nuclei with even numbers of nucleons are more bound than odd nuclei. The coefficients of the semi-empirical mass formula and magnitude of the pairing effect are empirically determined by fits to the experimental binding energies.

The success of the liquid drop model as a tool for understanding nuclear structure lies with its ability to describe the systematics of the nuclear binding energies across a wide

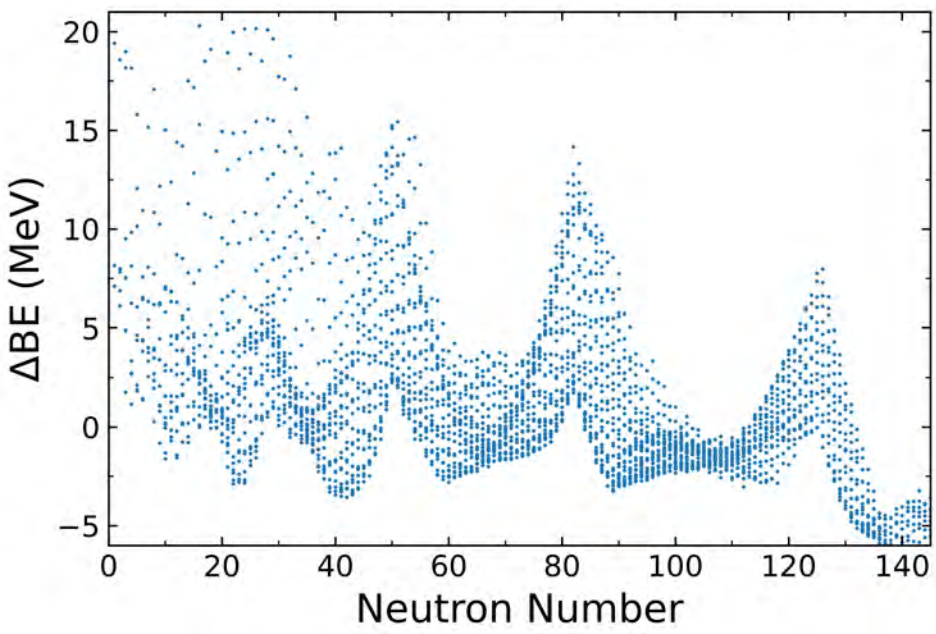

Figure 1.1: Difference in the experimental binding energies obtained from [4], to those calculated using the semi-empirical mass formula in equation 1.1, using the coefficient values of a_V = 15.8 MeV, a_S = 18.3 MeV, a_C = 0.714 MeV, a_A = 23.2 MeV and $\delta = \pm 12/A^{1/2}$. The systematic underestimation of the binding energies at the magic numbers provides strong evidence for the nuclear shell structure.

range of nuclei. Indeed, for the majority of nuclei it is able to reproduce the experimental binding energies strikingly well, to an accuracy of under 1% for the heavier nuclei. However, as is demonstrated in figure 1.1, that by using such a simplified picture, some of the nuclear structure details are overlooked. At select neutron numbers, namely 2, 8, 20, 28, 50, 82 and 128, it can be seen that the experimental binding energies rise sharply beyond what can be accounted for by the liquid drop model. These numbers are often referred to as the magic numbers, which also occur with the protons, and are reflected not only in the nuclear binding energies, but also the energies of the first excited states and the separation energies [5]. To understand the origin and nature of these magic numbers, it is useful to take an independent-particle approach.

1.1.1 The Nuclear Shell Model

In the nuclear shell model, which is loosely analogous to the atomic shell model, the nucleons are described as independent point-like particles, that are free to move within a shared mean-field potential. As the nuclear potential is generated by the nucleons themselves, it follows the rough shape of the nuclear density profile; having a rounded off square

potential shape. A broadly used parametrisation of the nuclear mean-field potential is given by the Wood-Saxon potential in equation 1.2 [6].

$$V(r) = -\frac{V_0}{1+\exp\frac{r-R}{a}} \tag{1.2}$$

Where V_0 is the potential depth, R is the nuclear radius given by $R = 1.25\,A^{1/3}$ fm, and a is the diffuseness parameter. After solving the Schrödinger equation with the Wood-Saxon potential, the set of energy levels displayed on the left side of figure 1.2 emerge. As in atomic physics, the orbitals are labelled using the spectroscopic notation and have a degeneracy of $2(2l+1)$, where l is the orbital angular momentum. The large gaps between the energy levels that appear after the nucleon occupanicies of 2, 8 and 20, match the first three experimental magic numbers, but the calculations fail to replicate the higher magic numbers. The inclusion of the spin-orbit interactions splits the levels into either an aligned or an anti-aligned configuration, with a total angular momentum of $J = l \pm 1/2$, where the level with an aligned angular momentum experiences a reduction in energy [7, 8]. The exception to this is for the s-orbital, where only $J = 1/2$ total angular momentum is permitted. The magnitude of the energy level spitting increases with the l, so that the subshell spacing are correctly reproduced, and the degeneracy becomes $2J+1$, leading to the emergence of the experimental magic numbers from the calculations, see the right side of figure 1.2. As protons and neutrons are not identical particles, they are treated separately and are therefore in different shells. Consequently, the magic numbers appear for both nucleons, leading to the possibility of a doubly-magic nucleus.

In addition to explaining the origin of the magic numbers, the nuclear shell model provides a simple framework for accurately predicting the groundstate spins and parities, and to a lesser extent the first few excited states, of a range of nuclei. By sequentially filling the orbitals and noting that the nucleons in the same level form pairs of opposite angular momenta, the nuclear properties are assumed to be attributed to the motion of the last unpaired nucleon. The nuclear angular momentum is therefore determined by the orbital in which the unpaired nucleon resides, and the parity is given by $\pi = (-1)^l$. This explains the origin of the groundstate properties of nuclei with even numbers of protons and neutrons being 0^+, as the angular momenta couple to zero. In the case where the nucleus has both an odd number of protons and neutrons, the nuclear angular momentum will be one of the possibilities from the sum of the angular momenta of the unpaired nucleons and the parity will be the product of the two.

This type of extreme independent-particle approach is a very course approximation, which tends to work best for nuclei near closed shells and for the lower excited states, as it assumes

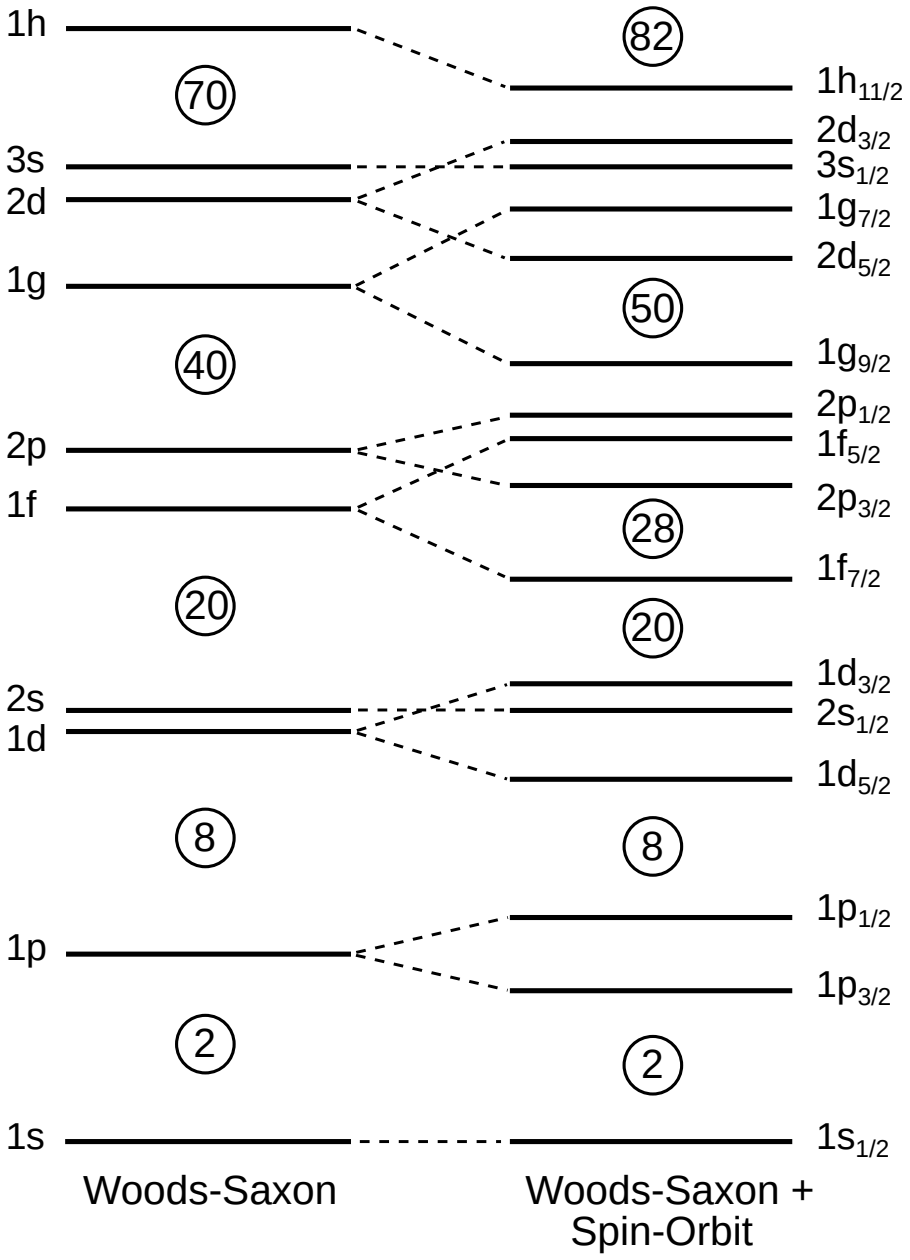

Figure 1.2: Single-particle states shown for a Woods-Saxon potential on the left and with the inclusion of the spin-orbit interactions on the right. The splitting of the orbitals with the spin-orbit interactions is shown to correctly reproduce the large gaps that correspond to the experimentally determined magic numbers.

there are no interactions between the valence nucleons. However, for open-shell nuclei with several valence nucleons, it is known that the contributions from the residual interactions become significant. To account for these effects in the description of the nuclear properties, it is necessary to take a more detailed approach to the shell-model formalism.

1.1.2 Shell-Model Formalism

For the theoretical description of the nuclear system, the fundamental problem that needs to be solved is the A-body Schrödinger equation, which is given by

$$\hat{H}\psi = \left[\sum_{i}^{A} \hat{T}_i + \hat{V}_A\right]\psi = E\psi\,, \tag{1.3}$$

where $\hat{T}$ is the kinetic energy operator and $\hat{V}_A$ is the total nuclear potential. However, as the form of the total nuclear A-body potential remains, as yet unsolved, it is useful to exploit the short range of the nuclear force, so that the potential is restricted to only the two-body interactions. The nuclear Hamiltonian can then be expressed as

$$\hat{H} = \sum_{i}^{A} \hat{T}_i + \sum_{i<j}^{A} \hat{V}_{ij}\,, \tag{1.4}$$

where $\hat{V}_{ij}$ is the two-body interaction between the nucleons i and j. In general, many-body problems such as this are difficult to calculate directly, as solving the Schrödinger equation with the Hamiltonian above quickly exceeds the computational limits of the current hardware, particularly as the A increases for the larger nuclei. The shell-model approach to making this problem tractable is to introduce a central potential $\hat{U}_i(\mathbf{r}_i)$, that only depends on the co-ordinates of the nucleon i and represents the mean potential it experiences from the other nucleons. The Hamiltonian can then be split into the behaviour of the independent nucleons in the mean-field potential $\hat{H}_0$ and the residual interactions $\hat{H}_{\text{res}}$ between them [9].

$$\hat{H} = \underbrace{\sum_{i}^{A}\left[\hat{T}_i + \hat{U}_i(\mathbf{r}_i)\right]}_{\hat{H}_0} + \underbrace{\sum_{i<j}^{A}\hat{V}_{ij} - \sum_{i}^{A}\hat{U}_i(\mathbf{r}_i)}_{\hat{H}_{\text{res}}} \tag{1.5}$$

By applying an appropriate potential, for instance the Woods-Saxon with the spin-orbit interactions, the contributions of the residual interactions component $\hat{H}_{\text{res}}$ can be min-

imised, so that the behaviour of the nucleus is described purely by the motion of the independent particles in the mean-field potential. This is the simple shell-model approximation that was discussed above, that could replicate the magic numbers and predict the ground state properties of a range of nuclei. However, as was stated in the previous section, for nuclei not near a closed shell this simplification breaks down, as it becomes necessary to consider the residual interactions. Assuming the nucleus to be comprised of an inert core of $A-N$ nucleons, with N nucleons orbiting in the valence shells, the Hamiltonian can be decomposed into each of the contributions, such that $\hat{H} = \hat{H}_{\text{Core}} + \hat{H}_{\text{Val}}$. After applying the aforementioned approximation that the two-body forces in the core can be replaced with the mean-field potential, the Hamiltonians for each component can be expressed by the equations below [10].

$$\hat{H}_{\text{Core}} = \sum_{i=N+1}^{A} \left[\hat{T}_i + \hat{U}_i \left(\mathbf{r}_i \right) \right] \tag{1.6}$$

$$\hat{H}_{\text{Val}} = \sum_{i=1}^{N} \left[\hat{T}_i + \hat{U}_i \left(\mathbf{r}_i \right) \right] + \sum_{i<j=1}^{N} \hat{V}_{ij} \tag{1.7}$$

Where $\hat{H}_{\text{Core}}$ refers to the nucleons in the inert core and $\hat{H}_{\text{Val}}$ denotes the contributions of the valence nucleons. Here, the residual interactions are shown to be restricted to only the nucleons occupying the valence shells, considerably reducing the dimensionality of the calculations. The residual interactions between the valence nucleons are mediated by the effective two-nucleon (NN) interactions. These interactions, referred to as the two-body matrix elements (TBME), can be empirically obtained by modifying the free nucleon-nucleon interactions, via fitting to various experimental data sets [11]. Such phenomenological approaches have been used successfully to provide theoretical descriptions for a broad range of nuclei, see the USD-type interactions in the section below. An alternative and more fundamental approach to obtaining the effective nucleon interactions, deriving them from chiral effective field theory (EFT), is discussed in section 1.1.4.

1.1.3 USD-Type Interactions

The universal *sd* (USD) interactions are a phenomenological approach, where the valence space is restricted to the *sd*-shell (third principle quantum number), with all lower lying shells taken to be the core. The USD Hamiltonian is defined by 63 TBME and three single-particle energies (SPE), that have been fitted to various experimental binding energies and excitation energies, for *sd*-shell nuclei between A = 16-40 [12]. This approach

enables the description of the spectroscopic properties and energies of a broad range of nuclei with *sd*-shell configurations, with respect to a unified Hamiltonian applied to the *sd*-model space. The USD Hamiltonians are therefore able to provide realistic theoretical descriptions of the *sd*-shell nuclei, for use within nuclear structure and astrophysics research.

The original USD Hamiltonian has since been revised, using improved and extended sets of energy data. The first refinements of note were the USDA and USDB interactions, where updated data sets were particularly abundant around the neutron-rich *sd*-shell nuclei [13, 14]. Consequently, these interactions are able to provide a greater level of precision for the descriptions of neutron-rich nuclei in this mass region. An additional USD-type interaction, the USDC, has been recently developed, that directly incorporates the Coulomb interactions [15]. This Hamiltonian is therefore expected to be particularly effective at predicting the properties of the *sd*-shell nuclei in the vicinity of the proton drip line.

1.1.4 Interactions from Chiral Effective Field Theory

The inter-nucleon interactions are a fundamental consequence of the strong force that confines quarks into hadronic matter, based upon their colour charge, which is described by quantum chromodynamics (QCD). In the low-energy domain relevant to nuclear structure, the strong coupling of QCD which governs the interaction strength, is too large to allow for a peturbative expansion. As a result, the direct derivation of the interactions between nucleons, as a residual interaction stemming from the strong force, is highly non-trivial [16, 17]. However, the development chiral effective field theory (EFT) provides a means to navigate this issue, by using an appropriate separation of scales to approximate the nuclear forces in terms of the nucleons and pions [18].

Chiral EFT is consistent with all of the underlying symmetries of low-energy QCD and relies upon the separation of scales, based upon the large gap between pion mass of 140 MeV/c^2 and the masses of the vector mesons at around 800 MeV/c^2. An effective Lagrangian can then be constructed, consisting of the relevant interactions between the nucleons and pions, and organised as a systematic expansion in $\left(Q/\Lambda_\chi\right)^\nu$. Here, Q is the typical momenta of the nucleons and Λ_χ is the chiral breakdown scale, which is generally set to be between 700-1000 MeV, and is associated with the physics not explicitly resolved in the calculations. The hierarchy of the nuclear interactions that emerge in terms of power expansion in ν, from chiral perturbation theory, is displayed below in figure 1.3.

The interactions shown in figure 1.3 are defined in terms of the one- or many-pion ex-

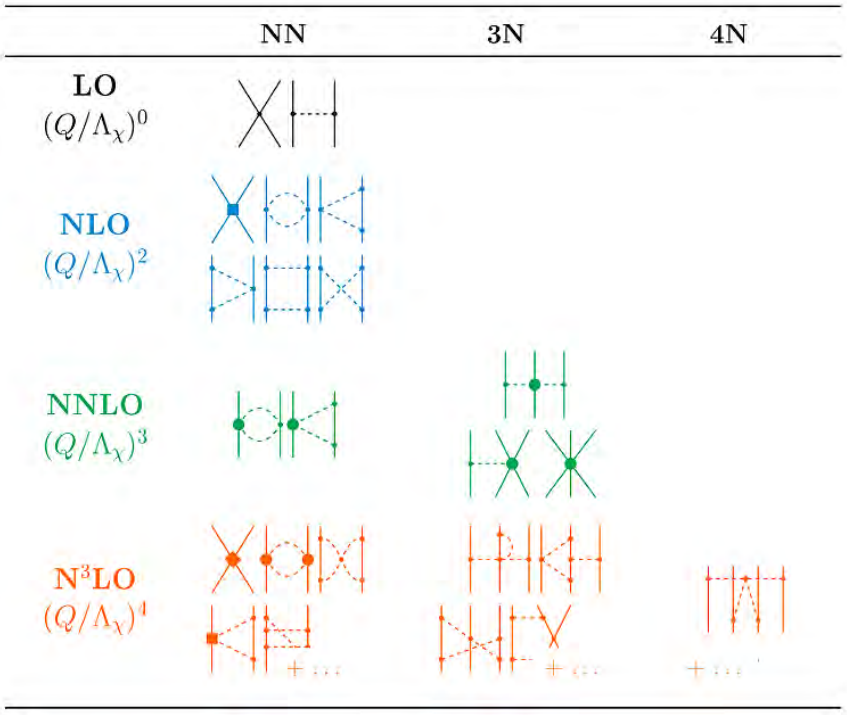

Figure 1.3: Illustration of the hierarchy of the nuclear forces that emerge from chiral EFT, taken from [19]. The solid lines represent the nucleons, with the dashed lines denoting pion exchange interactions and the solid circles, diamonds and boxes representing vertices that are proportional to the low-energy constants of chiral EFT.

changes between the nucleons, denoted by the dashed lines, and the nucleon-contact interactions that are indicated by the vertices. These contact terms encapsulate the short-range behaviour of the nucleon interactions, which is not explicitly resolved in the (Q/Λ_χ) expansion, due to the separation of scales. Therefore, the different vertices displayed on figure 1.3 correspond to the low-energy constants of chiral EFT, which are determined by fitting to experimental scattering data.

Using chiral perturbation theory to order the nuclear forces into the hierarchy in terms of the power ν, provides a means to estimate the relative contributions of each interaction [20]. Starting from the leading order (LO, $\nu = 0$), the only contributions to the NN interactions are from the one-pion exchange and nucleon-contact terms. The terms in the following order of $\nu = 1$ all vanish due to parity and time-reversal invariance. The next-to-leading order (NLO, $\nu = 2$) contains higher-order contact terms, in addition to several two-pion exchange interactions. In this order most of the details required to phenomenologically describe the NN forces have been included, with the primary shortfall being an insufficient intermediate-range attraction [20]. This problem is solved in next-to-next-to-leading order (NNLO, $\nu = 3$), where the first set of non-vanishing three-nucleon (3N) forces emerge. Con-

tinuing to progress further through the powers of ν, the higher many-body forces begin to appear, with the four-nucleon forces (4N) appearing in the following order, at $\nu = 4$, and so on. As the 4N interactions are a higher-order effect, they evidently contribute less than the 3N forces, which themselves are considerably weaker than the NN interactions from the $\nu = 0$ order. Thus, this framework presents a clear explanation for the empirically known hierarchy of nuclear forces, where $V_{NN} > V_{3N} > V_{4N} > ...$ [19]. These interactions that have been derived from chiral EFT are commonly used as the standard inputs for a broad range of many-body calculations, such as the ab initio methods, which are outlined in the following section.

1.1.5 Ab Initio Approaches

As the name suggests, the ab initio approaches aim to describe the properties of atomic nuclei, starting from the fundamental interactions between the nucleons [21]. These methods differ from the aforementioned phenomenological shell-model calculations with the effective interactions, in that the goal is to minimise the amount of fitting to experimental data, so as to avoid losing physical insight into the underlying nucleon interactions. There are a number of such many-body methods that have been devised in recent years, to solve the A-body Schrödinger equation, whilst treating all nucleons as active degrees of freedom. The nuclear interaction term again can be split into the individual contributions to the nuclear force, giving the Hamiltonian below.

$$\hat{H} = \sum_{i}^{A} \hat{T}_i + \sum_{i<j}^{A} \hat{V}_{ij}^{NN} + \sum_{i<j<k}^{A} \hat{V}_{ijk}^{3N} + ... \tag{1.8}$$

Where V^{NN} and V^{3N} are the two- and three-nucleon forces respectively. The interactions for the ab initio calculations generally consist of the realistic NN and 3N contributions, however in principle they can be expanded to include the higher orders. The NN interactions are still the dominant contribution, as per the assumption in the shell model of the short range of the nuclear force, but the inclusion of the 3N interactions can have notable impacts on the results. These effects are particularly pronounced in exotic nuclei, where the proton and neutron numbers differ significantly, see section 1.2. As was discussed previously, the chiral interactions are commonly used as the standard inputs for such calculations.

In addition to including the interactions from chiral EFT, most modern many-body ab initio approaches apply the similarity renormalisation group (SRG) technique, in order to

expedite the convergence of the calculations. The process aims to decouple the low- and high-momentum physics of the interactions, simplifying the many-body calculations, without altering the described physics. This increases the applicability of the methods to beyond just the lightest and least complex systems. The basic principle of the SRG technique is to apply a continuous unitary transform to the many-body Hamiltonian [21]

$$\hat{H}(s) = \hat{U}(s)\hat{H}(0)\hat{U}^{\dagger}(s)\,, \tag{1.9}$$

where $\hat{H}(s=0)$ is the starting Hamiltonian, s is the flow parameter that parameterises the unitary transformation $\hat{U}$, and $\hat{H}(s)$ is the SRG evolved Hamiltonian. Taking the derivative of equation 1.9 yields the operator flow equation

$$\frac{d}{ds}\hat{H}(s) = \left[\hat{\eta}(s), \hat{H}(s)\right]. \tag{1.10}$$

Here, the anti-Hermitian generator $\hat{\eta}(s)$ is related to $\hat{U}(s)$ by

$$\hat{\eta}(s) = \frac{d\hat{U}(s)}{ds}\hat{U}^{\dagger}(s) = -\hat{\eta}^{\dagger}(s)\,. \tag{1.11}$$

The Hamiltonian can then be transformed by integrating the flow equation for $s \to \infty$. The generator $\hat{\eta}$ is chosen in order to achieve the desired transformation of the Hamiltonian. For the choice of $\hat{\eta}$ there are many approaches, however one commonly used for nuclear structure and reaction calculations is the commutator of the kinetic energy with the Hamiltonian, which can be expressed as

$$\hat{\eta}(s) = \left(\frac{2\mu}{\hbar^2}\right)^2 \left[\hat{T}_{\text{int}}, \hat{H}(s)\right], \tag{1.12}$$

where μ is the reduced nucleon mass and $\hat{T}_{\text{int}}$ is the intrinsic kinetic energy operator. Using this generator diagonalises the Hamiltonian in momentum space, thus decoupling the low- and high-momentum physics in the operators and eigenstates. This process is regularly performed on the chiral NN+3N interactions, in order to improve the convergence properties of the many-body calculations.

The application of the SRG technique with the interactions from chiral EFT, has facilitated the development of a broad range of ab initio many-body approaches, such as the in-medium similarity renormalisation group (IMSRG) [22], self-consistent Green's function

(SCGF) [23], coupled cluster [24] and no-core shell model (NCSM) [25] methods. An exhaustive review of these techniques, amongst several other not mentioned, can be found here [19]. These computationally efficient techniques, with controlled truncations, are able to extend the range of nuclei that can be described the ab initio many-body calculations up to and beyond the tin region.

1.2 Light Neutron-Rich Nuclei

Experimental observables from neutron-rich nuclei offer some of the most stringent tests to the current theoretical models of the nuclear system. Indeed, recent developments in rare-isotope beam facilities and experimental techniques have paved the way for new measurements that have challenged the conventional descriptions of the atomic nucleus. A prime example of this is the disappearance of the traditional magic numbers, which were once thought to be immutable, and emergence of the new magic numbers when approaching exotic nuclei with extreme neutron-proton ratios. The first indication of a vanishing magic number was for the N = 20 shell closure in the neutron-rich sodium and magnesium nuclei [26, 27], which was able to explain the anomalous measurements in their binding energies [28], nuclear spectra [29] and mean square radii[30]. Further disappearances were observed for the N = 28 shell, in the measurements of the neutron-rich silicon and sulphur isotopes, below the doubly-magic ^{48}Ca nucleus [31, 32, 33]. Various new magic numbers have also been observed in the neutron-rich region of the nuclear chart, with the emergence of the apparent magic characteristics of ^{22}O (N = 14) [34] and ^{24}O (N = 16) [35], as well as in the ^{52}Ca (N = 32) [36] and ^{54}Ca (N = 34) [37] isotopes. A comprehensive review of the shell evolution effects and the emergence of the non-standard magic numbers in this region, can be found here [9, 38].

Neutron-rich nuclei in the vicinity of the drip line, the point after which additional neutrons will not be bound to the nucleus, exhibit a vast array of exotic phenomena. One such instance is that a select few weakly bound isotopes have a halo structure, with a well defined core and a 'halo' of lightly bound nucleons. The most well known of such nuclei are the ^{6}He, ^{11}Li and ^{11}Be isotopes, which are characterised by their larger than expected radii and comparatively low separation energies [40, 41]. Additionally, extremely neutron-rich nuclei often undergo new and exotic decay modes, such as the weakly unbound ^{26}O nucleus, which was discovered to decay directly to ^{24}O through the two-neutron emission [42], the dynamics of which are sensitive to the neutron-neutron interactions [43, 44]. These exotic effects therefore constitute key observables that can be used to test the nuclear models, benchmark their development and refine their predictive capabilities.

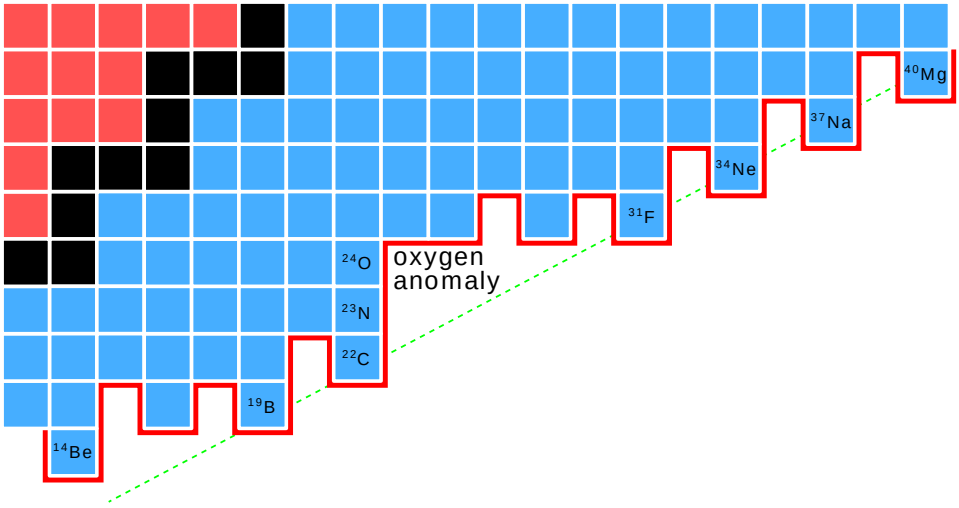

Figure 1.4: Illustration of the neutron-rich region of the chart of isotopes, highlighting the oxygen anomaly in the neutron drip line, adapted from [39].

1.2.1 The Oxygen Isotopic Chain

The oxygen isotopic chain at the interface of the medium-light mass regions, have proven to be excellent laboratories for the study of the nucleon interactions in neutron-rich nuclei [45]. With a closed shell of protons at Z = 8, the full range of bound isotopes are accessible to experiment, from the proton drip line at ^{13}O to the neutron drip line at ^{24}O, and beyond to the unbound ^{28}O. Across this range, these isotopes offer a number of challenges to the theoretical nuclear models, such as the weak Gamow-Teller β decay of ^{14}O [46], to the aforementioned closed-shell characteristics of ^{22}O (N = 14) and ^{24}O (N = 16), and the two-neutron decay of the unbound ^{26}O.

The discovery of the abrupt termination of the neutron drip line at ^{24}O [47], which is anomalously close to the line of stability, see figure 1.4, presented further challenges to nuclear theory. At the time, phenomenological shell-model calculations involving only the NN interactions generally placed the drip line at ^{28}O. It was only with the inclusion of the 3N forces from chiral EFT into the calculations, which added a repulsive component to the interactions between the valence neutrons, that the correct position of the neutron drip line at ^{24}O could be reproduced. Valence space calculations including the 3N forces were first to correctly place the neutron drip line at ^{24}O [48], later followed by ab initio calculations, treating all nucleons as explicit degrees of freedom [49, 50, 51]. This effect has also been replicated using the effective USDB interaction [45], but only after phenomenological adjustments to data in the mass region, that account for the neglected 3N forces.

The oxygen isotopes have since become a crucial benchmark for the developments of the many-body methods that include the chiral NN+3N forces. The structure of these iso-

topes have been systematically studied via a variety of approaches (NSCM [49], IM-SRG [52], coupled cluster [53] and valence space calculations [54]), with the calculated excitation spectra generally in agreement with experiment, and almost on par with those given by the phenomenological approaches. Therefore, the next logical step is the measurement of observables that are sensitive to the details of the nuclear structure, beyond that of the excitation energies. The electromagnetic transition rates for instance, constitute such an observable, with the recent report on the transition rates of ^{21}O [55] demonstrating the sensitivity to the chiral interactions, as well as the effective charges in the phenomenological shell-model approaches.

Following on from the ^{21}O measurement, the natural progression would be to extend the study to the heavier oxygen isotopes. The transition strengths in ^{22}O have been measured once before in a Coulomb excitation experiment, which inferred the lifetime of the 3199 keV 2^+ state to be 690 $\pm$ 280 fs [56]. One of the objectives of the work presented within this thesis was to obtain an improved measurement of this lifetime, using the model independent Doppler shift attenuation method, to examine the sensitivity to the chiral interactions. The experimental details, development of the novel ^{10}Be target required to populate the ^{22}O, analysis and results of this measurement are presented in chapter 4. The second key objective in this thesis was to analyse the nuclear structure of the odd neutron-rich ^{23}F isotope following a one-neutron removal reaction, which is detailed in chapter 3. The structure of ^{23}F can be roughly described as a ^{22}O (Z = 8, N = 14) core with a single valence proton. Thus, it can be used to test the proton-neutron interactions derived from chiral EFT, in addition to the interpretation of the single-particle degrees of freedom on top of a closed-shell core.

Chapter 2

Background

In this chapter the basic physics that underpins the experiments and analysis techniques that are mentioned throughout the thesis are discussed. Section 2.1 below gives a brief summary of the basic principles of γ decay, outlining the selection rules and the transition rates, primarily following the discussions in [5, 10]. This is followed by a review of the mechanisms by which both heavy ions and γ rays interact with matter in section 2.2, with particular emphasis on the processes relevant to the in-beam γ-ray spectroscopy experiments that are presented in this thesis. In section 2.3, the key characteristic features of γ-ray spectra are outlined, with a discussion on the Doppler correction process. Finally in section 2.4, there is a review of the various techniques to both directly and indirectly measure the lifetimes of nuclear excited states, with an in-depth overview of the Doppler shift attenuation method (DSAM).

2.1 Gamma Decay

Gamma decay is a mode of nuclear radioactivity that often follows a prior decay or reaction that results in the population of a nucleus in an excited state. Through the spontaneous emission of a γ-ray photon, the nucleus transitions from its initial state to one of a lower energy, with the energy difference carried by the γ ray. Neglecting the small nuclear recoil effects (generally smaller than the experimental uncertainties in the energy measurements), the γ-ray energy is given by

$$E_\gamma = \Delta E = E_i - E_f \,. \tag{2.1}$$

Reflecting the typical energy differences between nuclear excited states, γ rays are generally measured to have energies between 0.1 to 10 MeV. By studying the γ-ray emission through the γ-ray spectroscopy techniques mentioned throughout this thesis, a broad range of important nuclear structure observables can be accessed and compared to predictions from theory. Indeed, in addition to the energy difference between the states, the outgoing γ rays also carry some quanta of angular momentum l, to maintain conservation of angular momentum and parity when a nucleus transitions from a state of J_i^π to J_f^π. The l of the γ ray can be determined by measuring the angular distributions of the outgoing γ rays, see section 3.2.6. The angular momentum and parity of the emitted γ-ray photon are restricted by the gamma-decay selection rules, such that

$$|J_i - J_f| \leq l \leq J_i + J_f \tag{2.2}$$

$$\pi_\gamma = \pi_i \pi_f = \begin{cases} (-1)^l & \text{electric multipole} \\ (-1)^{l+1} & \text{magnetic multipole} \end{cases} \tag{2.3}$$

Where π_i and π_f are the parities of the initial and final states respectively. The angular momentum selection rules often permit several values of l units of angular momenta to be transferred when decaying from J_i to J_f. The different γ rays are therefore referred to by their multipolarities (2^l-pole), such that transitions with $l = 1$ are labelled dipole (2^1) transitions, $l = 2$ are quadrupole (2^2) and $l = 3$ are octupole (2^3). In such a circumstance where several multipolarities are allowed, the transitions with the lowest allowed value of l tend to dominate, with the higher multipole transitions being a much slower process, see the transitions probabilities section below.

The exception to the above angular momentum selection rule occurs when $J_i = J_f$, which would give a monopole ($l = 0$) transition to be the lowest allowed multipolarity. However, as there are no ($l = 0$) transitions in which a single photon is emitted, the lowest possible multipole γ ray for transitions where the initial and final angular momenta are the same, is a dipole ($l = 1$). In the unique situation where the angular momentum of the initial and final state are both zero ($J_i = J_f = 0$), $l = 0$ is the only solution to the angular momentum selection rule. Consequently, in such cases the decay via γ-ray emission is forbidden, instead decaying via the internal conversion process, where the excitation energy is carried away by an ejected orbital electron.

The class of the emitted radiation, whether it is electric or magnetic type, can be determined from the relative parities of the initial and final states. As the parity selection rule

in equation 2.3 indicates, if there is no change in parity ($\Delta\pi$ = no) then the radiation field must have an even parity. This only occurs in electric transitions where the l is even and in magnetic transitions where the l is odd. Inversely, in the case where the transition results in a change in parity between the initial and final states ($\Delta\pi$ = yes), the radiation field has an odd parity, which limits the multipolarities of the electric and magnetic transitions to odd and even values respectively. Therefore the parity selection rule can also be expressed as

$$\begin{aligned} \Delta\pi = \text{no:} \quad & \text{odd magnetic, even electric} \\ \Delta\pi = \text{yes:} \quad & \text{even magnetic, odd electric} \end{aligned} \tag{2.4}$$

The class of the electromagnetic transition and the mulitpolarity can be abbreviated using the notation (σl), where σ is either E or M, representing an electric or magnetic transition. Taking an example of a gamma decay from an initial state of $J_i^\pi = 7/2^+$ to $J_f^\pi = 5/2^+$, using the selection rules above, it is clear that the l can take values of between 1 to 6, and since there is no change in parity, the allowed transitions are M1, E2, M3, E4, M5 and E6. The transition is therefore likely to be M1 dominated, with a small amount of E2 mixing.

2.1.1 Transition Probabilities and Lifetimes of Nuclear States

The rate of radioactive decay is mediated by the decay constant λ, which denotes the probability per unit time of a decay event, and is related to the average lifetime of a radionuclide or excited state by $\tau = 1/\lambda$. For electromagnetic transitions, the decay constant can be calculated directly from the nuclear wave functions before and after the decay, ψ_i and ψ_f respectively, using Fermi's golden rule

$$\lambda = \frac{2\pi}{\hbar} \langle \psi_f | \hat{O} | \psi_i \rangle |^2 \rho(E_f) \,. \tag{2.5}$$

Where $\hat{O}$ is the operator that mediates the transition from ψ_i to ψ_f and $\rho(E_f)$ is the density of final states. The dependence of the decay rate on the density of final states can be heuristically understood by considering that the decay probability will be higher if there is a larger density of states in proximity to E_f, that can be accessed via the transition. Noting that the decay rate is proportional to the square of the transition matrix element, an additional parameter is often defined for the electromagnetic transition of a state J_i^π to J_f^π, given by

$$B(\sigma l; J_i^\pi \rightarrow J_f^\pi) = \frac{1}{2J_i+1} |\langle J_f^\pi || \hat{m}(\sigma l) || J_i^\pi \rangle|^2 . \tag{2.6}$$

The $B(\sigma l)$ parameter is known as the reduced transition probability, which contains the nuclear structure dependency of the transition, where $\hat{m}(\sigma l)$ is the radiation transition operator. The character of the transition, whether it is electric or magnetic, is again denoted by σ and l is the multipole order. Assuming the transition has a single radiation character of (σl), Fermi's golden rule can be adapted for electromagnetic transitions, and including the reduced transition probability, the probability of photon emission per unit time can be written as

$$\lambda(\sigma l) = \frac{2(l+1)}{\hbar\epsilon_0 l\,[(2l+1)!!]^2} \left(\frac{E_\gamma}{\hbar l}\right)^{2l+1} B(\sigma l; J_i^\pi \rightarrow J_f^\pi) . \tag{2.7}$$

As is evident from equation 2.7, the rate of an electromagnetic transition is dependent upon a number of different factors. The energy of the emitted γ ray (E_γ in MeV), affects the rate of transition, where the larger the γ-ray energy, the faster the transition will occur. Additionally, there is a strong dependence on the multipolarity, as low l transitions decay much faster than the higher l transitions of the same energy. Finally, there is the structural component to the transition that is contained within the $B(\sigma l)$ parameter, which was shown in equation 2.6 to be directly linked to the structure of the initial and final states. This highlights the power of the lifetime measurement as an experimental tool for understanding nuclear structure. As through this observable, there is a direct, model-independent way of accessing the detailed nuclear structure of the involved states.

The expression for the γ-decay rate in equation 2.7, can be rewritten into the reduced forms displayed in table 2.1 below, for the four lowest multipolarities of both the electric and magnetic transitions [57].

l	$\lambda(El)\ \left[e^2\, fm^{2l}\right]$	$\lambda(Ml)\ \left[\mu_N^2\, fm^{2l-2}\right]$
1	$1.59\times10^{15}\ E_\gamma^3\ B(E1)$	$1.76\times10^{13}\ E_\gamma^3\ B(M1)$
2	$1.22\times10^{9}\ E_\gamma^5\ B(E2)$	$1.35\times10^{7}\ E_\gamma^5\ B(M2)$
3	$5.67\times10^{2}\ E_\gamma^7\ B(E3)$	$6.28\times10^{0}\ E_\gamma^7\ B(M3)$
4	$1.69\times10^{-4}\ E_\gamma^9\ B(E4)$	$1.87\times10^{-6}\ E_\gamma^9\ B(M4)$

Table 2.1: Reduced forms of the γ-decay rate formulae for the four lowest multipolarities of both electric and magnetic transitions, where E_γ is in MeV.

Through the comparison of the formulae in table 2.1, the magnitude of the l dependence on the transition rate becomes apparent, where the decay probability falls off sharply for all but the lowest allowed multipolarities. The table also shows that the electric transitions have an additional two orders of magnitude in strength over the magnetic transitions of the same multipolarity. This therefore supports the example discussed in the selection rules section above, wherein it was concluded that a transition from $J_i^\pi = 7/2^+$ to $J_f^\pi = 5/2^+$ would be M1 dominated, with small amount of E2 mixing. However, in the opposite case where an E1 transition were to dominate, there would be a significantly lower, almost a negligible contribution of M2, due to this difference in strength.

In the regular occurrence where there are several permitted transitions for a γ decay, the total decay constant is simply the sum of the individual decay constants for the contributing modes of decay. It is from this total decay constant that the lifetime of an excited state can be determined via $\tau = 1/\lambda_{\text{total}}$. Therefore, to theoretically compute the average lifetime of an excited state, the individual decay constants for each of the transitions must be calculated using the formulae in table 2.1, and then summed.

2.2 Radiation Interaction with Matter

The mechanisms by which the different types of radiation interact with matter are necessary to understand the basic operations of their detectors. Since both experiments presented in this thesis involve in-beam γ-ray spectroscopy, the sections below outline the key processes relevant to the interactions of both heavy ions and γ rays, primarily following the discussions in [58]. In these sections, references will made to how the interactions are exploited in order to separate and identify the ions via their atomic numbers and masses, and for the detection and measurement of the γ rays.

2.2.1 Interactions of Heavy Ions

When heavy charged particles (Z>1) pass through matter, they experience a loss of kinetic energy via the interactions with the material. The total energy loss of the traversing particle is therefore the sum of the energy lost from each individual interaction over the entire trajectory. The kinetic energy reduction of the particle per distance travelled, in a specific absorbing material, is referred to as the linear stopping power and given by

$$S = -\left[\left(\frac{dE}{dx}\right)_e + \left(\frac{dE}{dx}\right)_n\right]. \tag{2.8}$$

The stopping power of an ion passing through a material has two key components (neglecting radiative effects at extremely high energies), the electric and nuclear stopping powers, denoted by the subscripts e and n in the equation above. The nuclear stopping power, which refers to the discreet elastic collisions with the material nuclei, often resulting in the significant deflection of the ions, is the primary energy loss mechanism for particles with kinetic energies of less than a few keV. However, as the ion-beam energies in the experiments discussed throughout this thesis are notably greater than this region, the principle contribution of interest is that of the electric stopping power. Thus, the remainder of this discussion on heavy-ion interactions will be on this component.

In contrast with the nuclear stopping power mentioned above, the electric stopping power processes give rise to a continuous energy loss of the ion, with no significant changes in direction, caused by inelastic interactions with the orbital electrons in the material. As a charged particle traverses an absorbing medium, the Coulomb interactions result in many of the bound electrons being excited to a higher energy state in the atom, or fully ionised, depending on their proximity to the ion. An equal amount of energy gained by the excited or ionised electrons, is lost by the traversing ion. Whilst each individual interaction results in a small loss of energy loss, the multiple simultaneous interactions sum up to be a significant net energy loss. It is for this reason why the ions generally take a straight path through matter, as they are not significantly deflected by any particular interaction, and also because the interactions occur from all directions simultaneously. The electric stopping power of high-energy charged particles passing through matter is well described by the relativistic Bethe-Bloch formula,

$$-\left(\frac{dE}{dx}\right)_e = \frac{Z^2 e^4 n_e}{4\pi\epsilon_0^2 m_e v^2}\left[\ln\left(\frac{2m_e v^2}{I(1-\beta^2)}\right) - \beta^2\right]. \tag{2.9}$$

Where Z and v are the atomic number and velocity of the traversing ion, where $\beta = v/c$, and e and m_e are the electron charge and rest mass respectively. The n_e parameter represents the electron density in the absorbing material, ϵ_0 the vacuum permittivity and the I quantity specifies the mean excitation and ionisation potential of the material. The Z^2 dependence highlighted by equation 2.9 enables the separation and identification of the ions, via their atomic numbers, in recoil detectors such as ionisation chambers. The generation of the electron-ion charge carriers in this process, and their flow in an applied electric field, produces the signals.

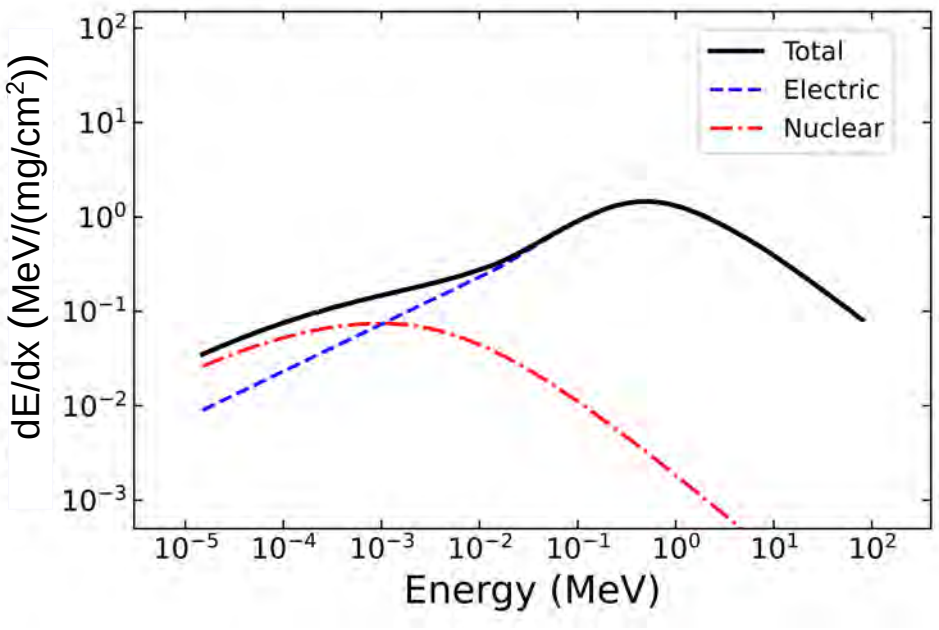

Figure 2.1: The stopping powers of a helium ion travelling through silicon is plotted against the ion energy, demonstrating the typical energies over which the electric and nuclear components dominate. The data in this plot was calculated using the SRIM stopping power tables [59], where the units of MeV/(mg/cm^2) were used to remove the material density dependence.

The energy dependence of the stopping power of an ion passing through matter can be observed from the plot in figure 2.1. The stopping power curve demonstrates that as an ion traverses an absorbing material, the stopping power it experiences increases as it slows down, with a rough $1/v^2$ dependence, until a maximum is reached towards the end of its range. This is often referred to as the Bragg peak. This inverse proportionality to the velocity of the particle can be understood with a simplified picture of an ion spending more time in the vicinity of the orbital electrons, thus transferring a greater amount of energy. At the lower ion energies the electron pickup from the absorbing material becomes significant, causing the electric stopping power to rapidly fall off, as the ion charge has effectively been reduced. Towards the end of its trajectory, the ion has accumulated sufficient electrons to be a neutral atom, and thus has no energy loss contribution from the electric stopping power.

2.2.2 Interactions of γ rays

Unlike heavy ions, γ rays do not continuously interact with the material they are passing through, instead undergoing abrupt interactions in which some or all of the photon

energy is transferred to the material, resulting in the scattering or full absorption of the γ ray. Neglecting coherent scattering, which does not contribute any significant deposition of energy, there are three primary mechanisms by which γ rays interact with matter. These are the photoelectric absorption, Compton scattering and pair production, which are illustrated in figure 2.2. The energy dependence of each interaction to the attenuation of a γ ray passing through germanium is demonstrated in figure 2.3, highlighting the energies over which the cross section for each mechanism dominates.

In the photoelectric absorption interaction, as is demonstrated in figure 2.2, an incident γ-ray photon is fully absorbed by an atom in the absorbing material, transferring all of its energy and ejecting a photoelectron from a bound atomic shell. The most probable emissions, for a γ ray of sufficient energy, are from the tightest bound shell or K-shell of the atom. The photoelectron is emitted with a kinetic energy given by

$$E_{e^-} = h\nu - E_b\,, \tag{2.10}$$

where E_b is the energy required to remove the photoelectron from its original atomic shell and ν is the frequency of the absorbed γ ray. An additional consequence of the photoelectric absorption is the creation of vacancies in the bound shells of the absorber atoms. These vacancies are promptly occupied via the capture of free electrons in the material, or through the rearrangement of the bound electrons, resulting in the emissions of characteristic X-rays or Auger electrons.

As figure 2.3 demonstrates, photoelectric absorption constitutes the primary mechanism by which low-energy γ rays, of up to a few hundred keV, interact with matter. The probability of this interaction scales approximately proportional to $Z^n/E_\gamma^{3.5}$, where n is generally between 4 and 5. It is for this reason why materials with greater atomic numbers are favoured for γ-ray detectors and shielding materials. The sharp discontinuity in the probability of photoelectric absorption, in the low energy region of figure 2.3, is the K-absorption edge, which corresponds to the binding energy of an electron in the K-shell of the absorber atom. For an incident γ ray with an energy slightly over the binding energy, the emission of a K-shell electron is energetically possible. However, for γ rays where the energy is below this absorption edge, this process is no longer possible, thus the probability of interaction falls sharply. There are similar absorption edges located at the binding energies of the L- and M-shells for the lower energy γ rays.

Compton scattering is the most probable interaction mechanism for intermediate-energy γ rays, of between a few hundred keV to roughly 10 MeV, which are typically the energies

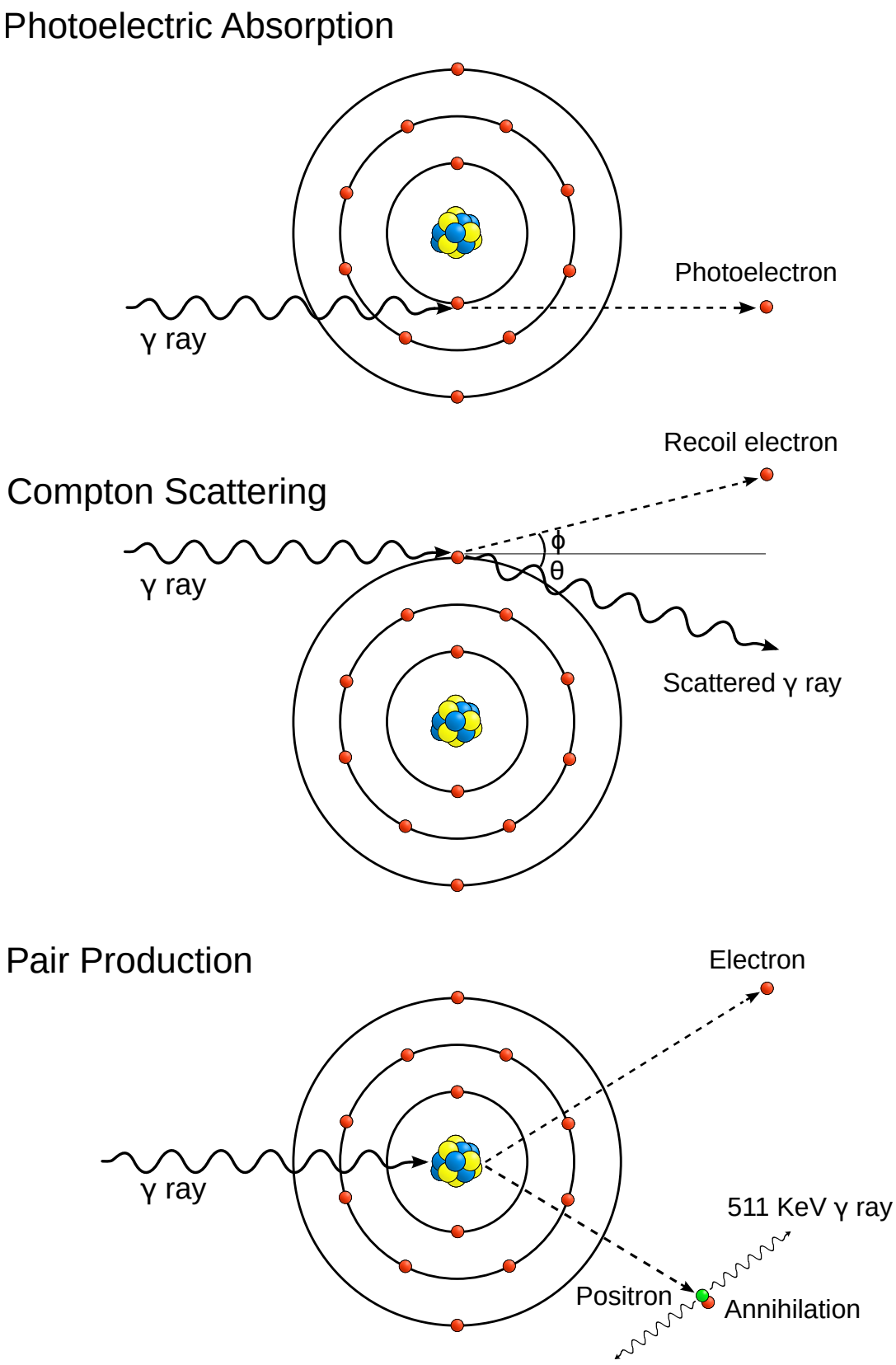

Figure 2.2: Schematic illustration of the three main mechanisms by which γ rays interact and deposit energy into matter.

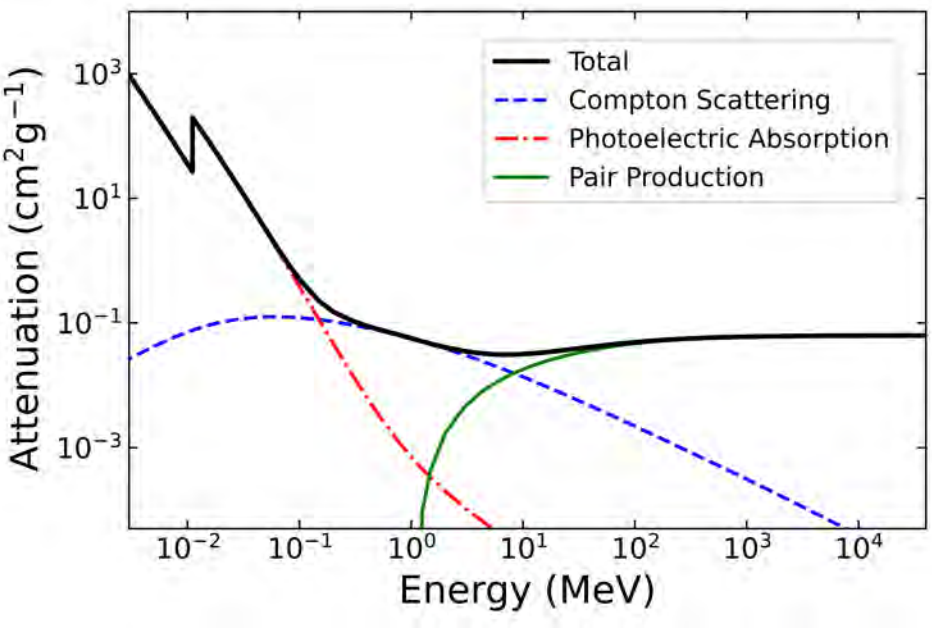

Figure 2.3: The contributions of each interaction process to the attenuation of γ rays in germanium, is plotted across a range of γ-ray energies. The energy regions over which each interaction mechanism dominates is clearly visible, as is the K-edge discontinuity in the low-energy part of the photoelectric absorption cross section. The γ-ray attenuation data presented in this plot was gathered from the NIST XCOM database [60].

expected from the γ decay of most radionuclides. In Compton scattering, the incident γ ray interacts with an electron in the absorbing medium and is scattered to an angle θ with respect to the incoming direction, as is shown figure 2.2. A fraction of the initial γ-ray energy is transferred to the recoil electron, which was assumed to be free (or very weakly bound) and at rest before the scattering event. The expression relating the energy of the scattered γ ray E'_γ to the angle through which it was deflected θ, is given by

$$E'_\gamma = \frac{E_\gamma}{1 + \frac{E_\gamma}{m_e c^2}\left(1 - \cos\theta\right)}. \tag{2.11}$$

Where m_e is the electron rest mass and E_γ is the initial γ-ray energy. The expression above indicates that for the forward scattering angles, a relatively small fraction of the initial γ-ray energy is transferred to the recoil electron. Inversely, for the larger scattering angles where $\theta \approx \pi$, a much larger proportion of the γ-ray energy is deposited in the material.

As the likelihood of an incident γ ray Compton scattering in a medium is dependent upon the number of electrons available to be scattered from, the cross section scales linearly with the number density and the atomic number of the material. The differential scattering cross

sections given by the Klein-Nishina formula below in equation 2.12, describe the angular distributions of the Compton scattered γ rays [61].

$$\frac{d\sigma}{d\Omega} = \frac{r_e^2}{2}\left(1+\cos^2\theta\right)\left(\frac{1}{1+\frac{E_\gamma}{m_e c^2}\left(1-\cos\theta\right)}\right)^2\left(1+\frac{\left(\frac{E_\gamma}{m_e c^2}\right)^2\left(1-\cos\theta\right)^2}{\left(1+\cos^2\theta\right)\left(1+\frac{E_\gamma}{m_e c^2}\left(1-\cos\theta\right)\right)}\right) \tag{2.12}$$

Where r_e is the classical electron radius. The angular distributions, given by the Klein-Nishina formula are illustrated in figure 2.4, for a range of incident γ-ray energies. The distributions demonstrate the preference of high-energy γ rays to be scattered to the forward angles.

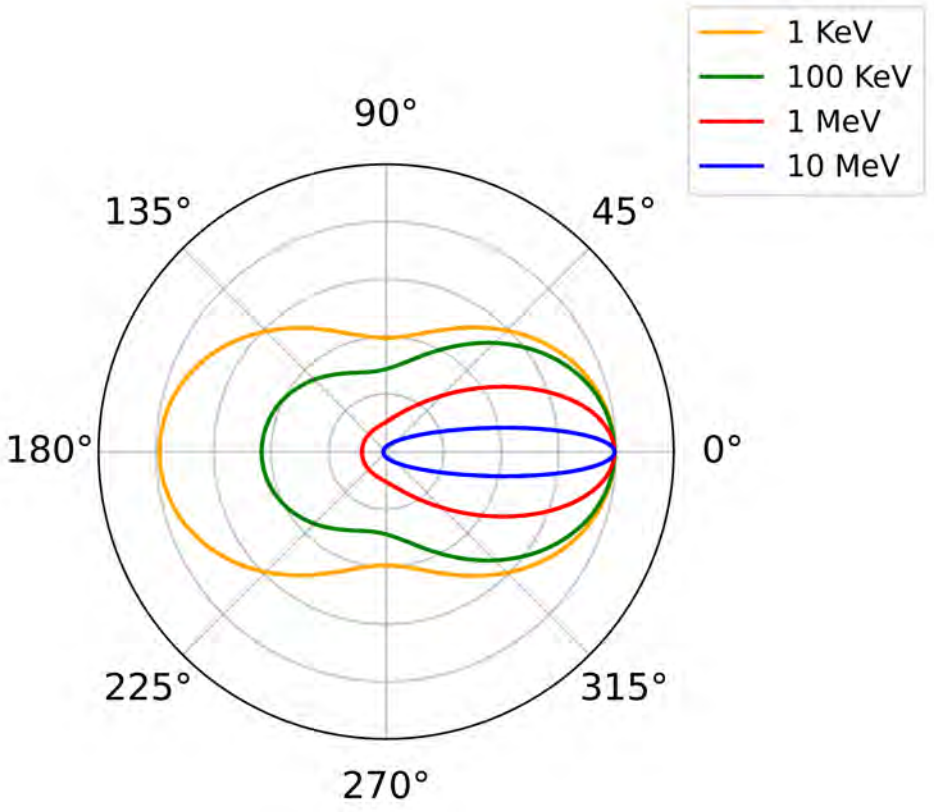

Figure 2.4: Plot of the probability of a γ ray to be deflected to a specific angle following a Compton scattering event, using the Klein-Nishina formula for a range of γ-ray energies. The tendency of higher energy γ rays to scatter towards the forward angles is demonstrated.

The final mechanism by which γ rays interact with matter is pair production, displayed in the bottom panel of figure 2.2. This process involves an incident γ ray interacting in the Coulomb field of a nucleus, and being replaced with an electron-positron pair. For this interaction to be energetically possible, the incoming γ-ray photon must have at least twice

the energy of the electron rest-mass energy (1.022 MeV), with the interaction cross section increasing sharply as the photon energy increases beyond this threshold. Consequently, for high-energy incident γ-ray photons (>5 MeV), pair production becomes the predominant interaction mechanism between γ rays and matter. The pair production cross section is also proportional to the square of the atomic number of the absorbing material, as the interaction must take place within a nuclear Coulomb field.

After the pair production event, any energy in excess of 1.022 MeV that was carried by the photon, is split between the kinetic energies of the outgoing electron and positron. At the end of its track, the positron will annihilate with an electron in the absorbing material, emitting the two characteristic 511 keV γ rays.

2.3 γ-ray Spectroscopy

When an incident γ ray interacts within the sensitive volume of a detector, via the mechanisms described above, some or all of the original photon energy is transferred to the electrons in the material, which are then detected and processed as a signal. A detailed discussion on the principle operation of semi-conductor detectors after interacting with an incident γ ray can be found in section 3.1.4. Although the detector response to an incident γ ray is dependent on the type of detector, the geometry and the material, there are characteristic features that appear on most γ-ray spectra. The annotated drawing in figure 2.5 illustrates a typical γ-ray spectrum resulting from the detection of high-energy γ rays, with the characteristic elements highlighted.

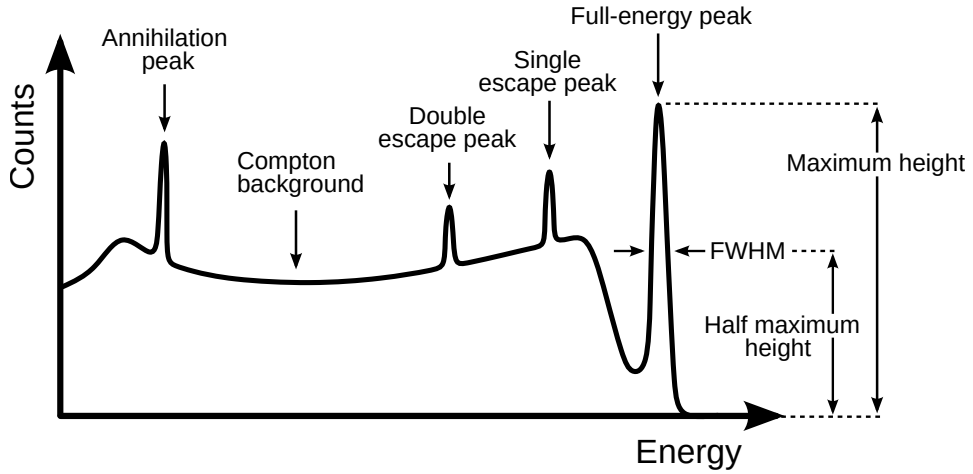

Figure 2.5: Annotated sketch of a typical γ-ray spectrum of a medium-high energy γ ray.

The features that are present on all γ-ray spectra are the full-energy peak and the Compton background. The full-energy peak represents the scenario in which the total energy of

the incident γ ray is deposited into the detector, independent of its track through the material. A γ ray that Compton scattered several times in the detector material before undergoing photoelectric absorption, would have the same response as a γ ray that underwent photoelectric absorption as the first interaction, provided all of the scattered γ rays and recoil electrons were captured. This is due to the events of a single γ-ray track effectively occurring in coincidence, with respect to the detector response times. Therefore, the signals from the individual electrons combine, and assuming the detector responds linearly to electron energy, the produced signal is proportional to the total deposited energy, which if no secondary radiation escapes, is the energy of the incident γ ray.

In situations where the Compton scattered γ rays escape from the sensitive volume of the detector, only a fraction of the incident γ-ray energy will be deposited. As was discussed in the above section, the energy transferred to the recoil electrons is dependent on the scattering angle of the γ ray, with the maximum energy deposition being when the γ ray is backscattered. As all scattering angles will occur in the detector, a continuum of energies will be deposited into the material, forming the characteristic shape illustrated in figure 2.5. The Compton edge can be observed to be where the continuum terminates at the higher energies, corresponding to the largest amount of energy that can be deposited via a single Compton event. In the rarer cases where the γ ray undergoes multiple Compton scattering events before escaping the detector, more energy is able to be deposited into the material than can be transferred by a single Compton event, partially filling the gap between the Compton edge and the full-energy peak.

For higher energy γ rays where the pair production interaction becomes significant, additional features appear upon the γ-ray spectrum, on account of the two 511 keV γ rays emitted at the end of the positron tracks. Assuming a total deposition of the electron and position kinetic energies, the escape without interaction of one or both of the annihilation γ rays, results in the appearance of additional peaks on the γ-ray spectrum, that correspond to the subtraction of the total energy deposition, by the escaped γ rays. These structures are referred to as the single escape and double escape peaks, and are located 511 keV and 1.022 MeV below the full-energy peak, respectively. In reality, there exists a wide range of other possibilities in which one or both of the 511 keV γ rays undergo a partial energy deposition via Compton scattering, before escaping the detector. In such circumstances, these events form part of the continuum between the double escape and full-energy peaks. Additionally, the detection of the secondary annihilation γ rays, resulting from the pair production interactions in a non-sensitive medium, produces the characteristic 511 keV peak in the γ-ray spectrum.

2.3.1 Relativistic Doppler Shift

A key characteristic of both of the experiments presented in this thesis, is that they are in-beam γ-ray spectroscopy measurements, in which the γ rays of interest are emitted in-flight, by the excited ions. The high ion velocity at the instance of emission, means that the relativistic Doppler shift of the γ rays becomes a significant effect. Consequently, the detected γ-ray energies in the laboratory frame have a dependence upon the angle at which they were detected, relative to ion-beam direction. The expression relating the detected lab-frame energy of a γ ray with a transition energy E_0, detected at an angle θ and emitted by a source travelling with a velocity $\beta = v/c$, is given by

$$E_{\text{Lab}} = E_0 \frac{\sqrt{1-\beta^2}}{1-\beta\cos\theta_\gamma}. \tag{2.13}$$

The image at the top of figure 2.6 demonstrates the ratio of the detected γ-ray energy to the centre-of-mass energy, across a range of detection angles and beam energies. The plot shows that for γ rays emitted by high-velocity ions, the detected energies can be smeared over extremely large energies on the γ-ray spectrum, losing any peak definition and forming smooth background structure, as is evident from the uncorrected spectrum in figure 3.15. Clearly then, to recover the γ-ray peak structures in experiments with such beam energies, the energy-angle dependence of the γ rays has to be removed via a Doppler correction.

The Doppler correction process removes the correlation between the detected γ-ray energy and the angle it was detected at, by inverting the relationship in equation 2.13. However, there is often a noticeable reduction in the energy resolution of the γ-ray spectrum post Doppler correction. Indeed, for the higher energy beams, it is the uncertainties in the Doppler correction itself that often dominate the energy resolution of the Doppler corrected spectrum. The impact of each of the uncertainties in the Doppler correction, to the energy resolution of the spectrum, can be derived from equation 2.13 [62]. These contributions can then be summed up via the propagation of uncertainties, to obtain the expression for the energy resolution of a peak post Doppler correction [63], shown below in equation 2.14.

$$\left(\frac{\Delta E_{\gamma 0}}{E_{\gamma 0}}\right)^2 = \left(\frac{\beta\sin\theta_\gamma}{1-\beta\cos\theta_\gamma}\right)^2 (\Delta\theta_\gamma)^2 + \left(\frac{\beta-\cos\theta_\gamma}{(1-\beta^2)(1-\beta\cos\theta_\gamma)}\right)^2 (\Delta\beta)^2 + \left(\frac{\Delta E_{\text{intr}}}{E_\gamma}\right)^2 \tag{2.14}$$

Where the energy resolution here is represented as a fraction of the transition energy $\Delta E_{\gamma 0}/E_{\gamma 0}$. The total energy resolution is the sum of the contributions from the uncertainties in the

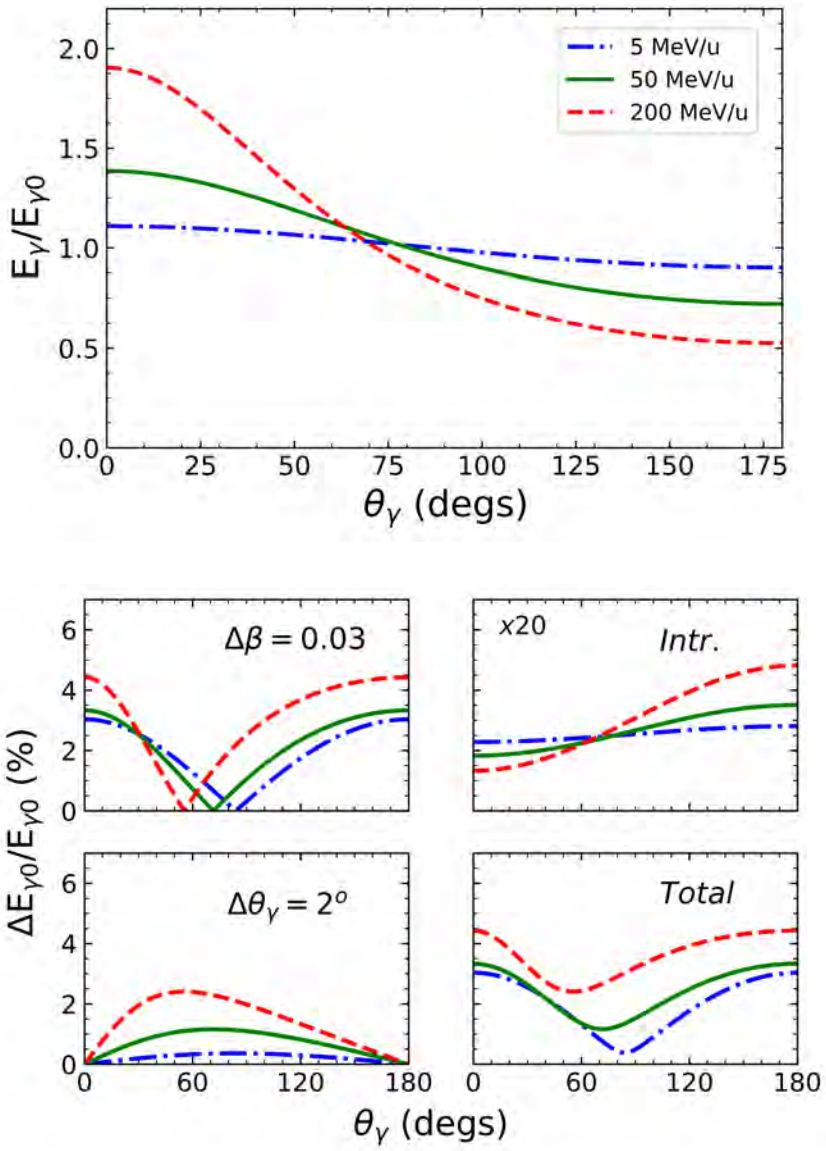

Figure 2.6: The plot on the top illustrates the ratio of the γ-ray energy in the laboratory frame to the rest frame, across a range of detection angles. The bottom four plots demonstrate the contributions to the energy resolution loss of a peak post Doppler correction. The top left panel shows the contribution due to an uncertainty in the Doppler correction β, the bottom left from an uncertainty in the detection angle, the top right is the intrinsic resolution and the bottom right panel shows the sum of the individual components. The contribution from the intrinsic resolution is multiplied by 20 in this plot, to demonstrate the lesser affect it generally has on the Doppler corrected resolution. All of the data that is presented in these plots was calculated for an A = 20 ion with a kinetic energy of 5 MeV/u, 50 MeV/u and 200 MeV/u.

detection angles $\Delta\theta_\gamma$ and emission velocities $\Delta\beta$, in addition to the intrinsic energy resolution of the detector ΔE_{intr}. The contributions of each of the components is illustrated in the bottom four plots of figure 2.6, across a range of detection angles, for an example set of uncertainties and beam energies.

The importance of a good Doppler correction is highlighted by equation 2.14, as to maintain a high-resolution Doppler corrected γ-ray spectrum, the detection angles and emission velocities must be accurately determined. There are however situations in which these uncertainties can be deliberately induced into a measurement, exploiting the relationships in equation 2.14 to produce lifetime-sensitive lineshapes on the γ-ray spectrum. Indeed, the induction and subsequent measurements of these lineshapes constitutes the fundamental principles of several Doppler Shift lifetime techniques, which are discussed in further detail in the section below.

2.4 Lifetime Measurements

Once populated via a reaction or decay, a nuclear excited state will exist for an average lifetime τ before decaying. This lifetime is related to the total decay width of the initial state by

$$\Gamma_{\text{total}}\tau = \hbar, \tag{2.15}$$

where the total width Γ_{total}, is the sum of the partial widths of all possible transitions. The measurement of the lifetime of an excited state, either directly or by inferring from the decay width, is a critical tool in experimental nuclear physics, providing key nuclear structure insights [64]. As was discussed in section 2.1.1, the excited state lifetimes are linked to the reduced transition strengths $B(\sigma l)$, which represent a model-independent way to access information on the nuclear wavefunctions and matrix elements. These measurements can therefore be compared to the predictions from theory and used to assess the accuracy of nuclear models.

A variety of experimental techniques have been developed in order to measure the excited state lifetimes across a broad range of sensitivities. The techniques displayed in figure 2.7, can be divided into either directs methods, which directly measure the lifetimes of the excited states, or indirect methods, in which the lifetimes are extracted from the decay widths. The objective of the experiment presented in chapter 4 of this thesis, was to directly measure the lifetime of the first 2^+ state in ^{22}O, which was inferred to be 690 ± 280

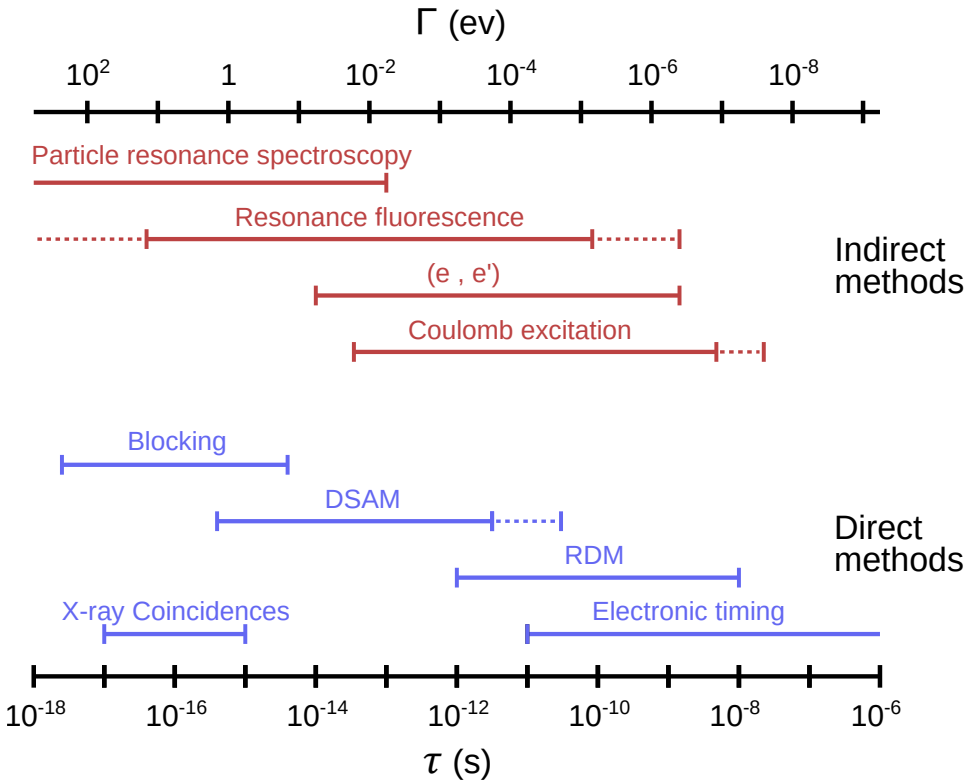

Figure 2.7: Illustration of the effective ranges for an assortment of lifetime measurement techniques. The direct methods measure the lifetime τ of the state of interest directly, whilst the indirect methods infer the lifetime from the width Γ. This plot was taken and adjusted from [64].

fs from a previous Coulomb excitation measurement [56]. Therefore, to cover the expected lifetime range of this state, the Doppler shift attenuation method (DSAM) was selected for the measurement.

2.4.1 Doppler Shift Attenuation Method

The Doppler shift attenuation method (DSAM) is a technique that enables the direct measurement of the nuclear level lifetimes in the femtosecond to picosecond range. The premise of this technique involves the population of an excited state via a nuclear reaction, followed by the subsequent observation of the γ decay in-flight, as it passes through a known material [65]. By measuring the Doppler shift of the γ-ray energy in the laboratory frame, given by equation 2.13, the velocity of the recoiling nucleus at the instance of γ-ray emission can be determined. The distributions of recoil γ-emission velocities results in the emergence of a lifetime-sensitive lineshape on the γ-ray spectrum. If the time frame of the slowing and energy loss processes of the recoils passing through the stopping medium is known, see section 2.2.1, the lifetime of the state can be extracted from this lineshape.

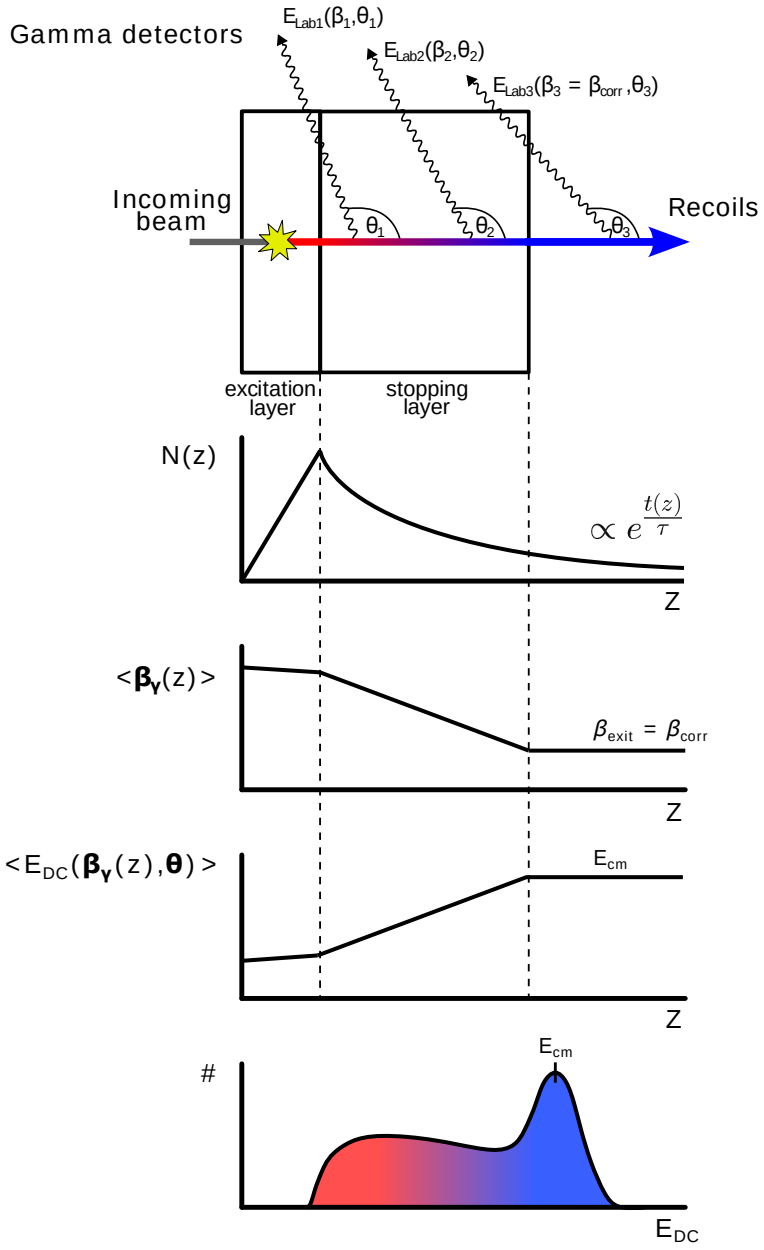

Figure 2.8: Diagrammatic sketch demonstrating the principles of the Doppler shift attenuation method (DSAM), where the ions leave the back of the target and the γ-ray detectors are placed towards the backward ($> 90°$) angles. The average emission velocities $\langle\beta_\gamma(z)\rangle$ of the excited recoils are visually represented by the colours, where the red denotes a higher velocity and the blue is slower. A sketch of a typical peak and lineshape on a Doppler corrected γ-ray spectrum, resulting from the distribution of emission velocities, is shown in the bottom image, with the exit velocity taken for the Doppler correction.

There are several variations and modifications to the DSAM technique that can be configured to the requirements of the measurement. The diagram in figure 2.8 illustrates setup of the DSAM measurement of the first 2^+ state in ^{22}O, see chapter 4, where the recoils leave the back of the target and the γ-ray detectors are placed towards the backward ($> 90°$) angles. Typically in such DSAM measurements, the targets are comprised of two distinct sections; the excitation layer wherein the reactions to populate the state of interest takes place, and the stopping layer, which degrades the velocities of the ions that pass through it. The average velocities of the excited recoils are visually represented in figure 2.8 by the coloured arrow, where red is fast and blue is slow.

The plots beneath the sketch of the target in figure 2.8 break down the formation of the expected lineshape on the Doppler corrected γ-ray spectrum. After the excited recoils are populated by the reactions in the excitation layer, they pass through the remainder of the target, all the while emitting γ rays according to the exponential decay law. The recoils passing through the target gradually lose energy so that the average velocity at the instance of γ-ray emission $\langle\beta_\gamma(z)\rangle$, reduces until the recoils leave the back of the target, as is illustrated by the central plot. Taking the recoil exit velocity for the Doppler correction β_{corr}, causes the decays that occur outside of the target to be reconstructed back to the centre-of-mass energy E_{cm}. Alternatively, the decays that occur inside the target, at higher velocities ($\beta_1 > \beta_2 > \beta_3 = \beta_{\text{corr}}$ in the diagram), will have a lower Doppler corrected energy due to the backward ($> 90°$) detection angles. For setups with forward detection angles the reverse is true, where the higher velocities in the target causes an increase in the Doppler corrected γ-ray energies, and the line in the second-to-last plot is reflected in the y-axis, about the E_{cm} energy. This distribution of recoil γ-emission velocities creates a lineshape on the γ-ray spectrum, an example of which is sketched on the bottom plot of figure 2.8, demonstrating the slow and fast components by the blue and red shaded regions. The lifetime sensitivity is clear by considering that for different nuclear state lifetimes τ, the decay curves will change, resulting in different recoil γ-emission velocity distributions, altering the lineshape of the Doppler corrected γ-ray peak. Thus, the sensitive range of lifetimes for this technique is constrained by the recoil stopping/transit time through the target.

Chapter 3

Nuclear Structure of ^{23}F Following a One-Neutron Removal Reaction

The neutron-rich ^{23}F isotope is located one proton above the weakly doubly-magic ^{22}O (Z = 8, N = 14) and decays via β^- decay to ^{23}N, with a half-life of 2.23 ± 0.14 s [66]. The structure of a single valence proton outside the ^{22}O core makes ^{23}F an excellent candidate for studying the single-particle properties, as the assumption of the single-particle degrees of freedom on top of a closed-shell core can be tested, see figure 3.1. The measurement of the excitation spectra of the fluorine isotopes provides a unique opportunity to study the effect of the proton-neutron interaction on the orbital energy gaps for odd-A isotopes. Previous measurements of the energy of the first excited state of ^{23}F, a low-lying single-particle proton $1/2^+$ state, shows it to be significantly higher than those of the neighbouring odd-A ^{17,19,21}F isotopes [67], indicative of the strong N = 14 shell closure also present in ^{22}O. Take for example the ^{17}F isotope, which has a similar structure to the ^{23}F, in that a single proton is located outside of the doubly-magic ^{16}O core. Any differences in the energies of the low-lying proton states between these isotopes can then be ascribed to the full or empty occupancy of the $\nu 1d_{5/2}$ orbital. This can be seen in the independent-particle picture as the neutron occupancy widening the energy gap between the $\pi 1d_{5/2} - \pi 2s_{1/2}$ orbitals. Another interesting measurement along this theme is the energy of the $3/2^+$ proton state, as it could determine the energy gap between the $\pi 1d_{5/2} - \pi 1d_{3/2}$ orbitals. This would effectively probe the spin-orbit splitting of the d-orbital, in which the tensor interaction is suspected to have a contribution [9].

The production of the ^{23}F via the one-neutron knockout reactions on incoming ^{24}F fragments, will populate a range of states with spins from $1/2^+$ to $11/2^+$, via the removal of a neutron from the $\nu 1d_{5/2}$ orbital. The knockout of the neutron in the $\nu 1s_{1/2}$ orbital will di-

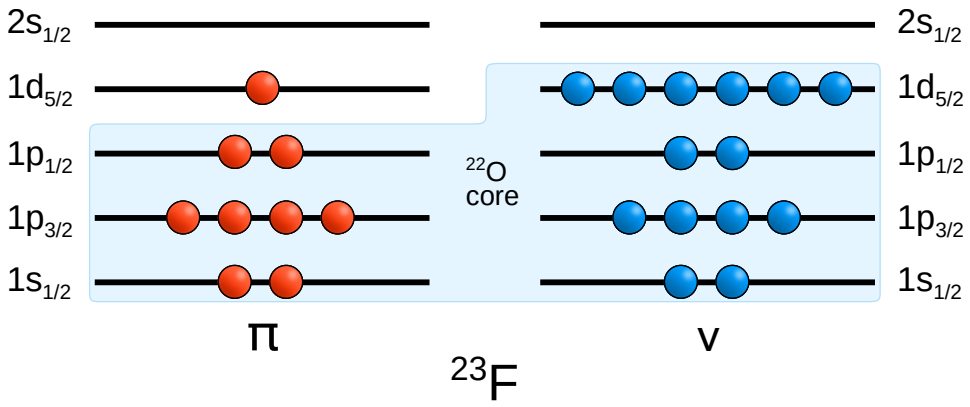

Figure 3.1: Sketch of the ^{23}F shell structure, illustrating the interpretation of a single valence proton on top of a ^{22}O core.

rectly populate the ground state of the ^{23}F fragments and the removal of a neutron from the lower shells is unlikely, as they are more deeply bound. The excitation spectrum of ^{23}F has previously been measured; most notably following the β decay of ^{23}O [67] and various particle-transfer reactions [68, 69]. However, no electromagnetic transition rates have so far been recorded. The measurement outlined in this chapter, with access to the high-resolution γ-ray detector array, GRETINA, and significantly greater statistics, stands to markedly improve the quality of the excitation spectrum data and enable a more precise probing of the nuclear structure of this system.

In the following sections the different aspects of the measurement are discussed. Starting with section 3.1, the experimental setup is outlined, providing a brief review of the key components, how they operate and why they were necessary for the measurement. Section 3.2 overviews the methods and techniques that were applied in the data analysis, stating and reviewing any approximations that were made. This is followed by a presentation of the results in section 3.3 and the discussion in section 3.4, where the results are compared to those of previous experimental works and the phenomenological shell-model calculations.

3.1 Experimental Setup

The experiment was carried out at the National Superconducting Cyclotron Laboratory (NSCL) at Michigan state university, in March/April 2016. A ^{48}Ca primary beam was accelerated by the two coupled cyclotrons, K500 and K1200, into the A1900 fragment separator and then onto a ^{9}Be production target. Various reactions in the primary target resulted in the production of a wide assortment of fragments. The A1900 was used to separate these incoming fragments and select the ^{24}F isotopes, with energies of around 95 AMeV. The ac-

cepted ^{24}F beam had a purity of 95% with a momentum spread of approximately 2%. The selected ^{24}F fragments were then impinged upon a 2 mm thick (370 mg/cm^2) ^{9}Be secondary target, wherein the one-neutron removal reactions took place to populate the ^{23}F. The γ rays emitted in-flight by the excited ^{23}F fragments were detected by the tracking γ-ray detector array GRETINA, which was mounted surrounding the target chamber. GRETINA was coupled to the S800 spectrograph, so that the outgoing fragments and unreacted beam could be separated and identified, and the γ-ray transitions in ^{23}F could be studied.

The experiment was originally set up and optimised for the measurement of electromagnetic transition rates in ^{21}O, via the recoil distance method, and thus ran with two settings. The first was with a single ^{9}Be target for the simple identification of the ^{21}O fragments and the transitions of interest. The second configuration was with the inclusion of a ^{181}Ta degrader to induce lifetime-sensitive lineshapes in the peaks of interest, that could be measured [70, 55]. In addition to the ^{21}O, it was discovered that there were several other channels that were strongly populated in the experiment. One of which, the ^{23}F, is the subject of the analysis in this chapter. Only the runs in the first setting were analysed here however, as the addition of the ^{181}Ta degrader blocked the acceptance of the ^{23}F fragments into the S800. The following subsections detail the key components of the experiment, with a focus on their operations and necessity to the measurement.

3.1.1 A1900 Fragment Separator

The A1900 Fragment separator is a large-acceptance spectrometer, comprising of several dipoles and detector systems, see figure 3.2. Together with the K500 and K1200 coupled cyclotrons, the A1900 constitutes one of the key components at NSCL, for the production of rare-isotope beams [71]. Following the fragmentation reactions of the ^{48}Ca primary beam within the ^{9}Be production target, there were a wide assortment of fragments entering the A1900. The first dispersive half of the A1900 filters these fragments to a single magnetic rigidity $B\rho$, see equation 3.1.

$$B\rho\frac{c}{\gamma\beta} = \frac{m}{q} \tag{3.1}$$

Where a fragment of mass m with a velocity v and charge q is bent by a radius ρ in the magnetic field B (the β, γ and c parameters take their usual relativistic definitions). As the fragments with this energy range are fully ionised, the fragment charge is identical to Ze. The momentum distribution, $\Delta p/p$, of the secondary beam may be selected here, through the adjustment of the beam slits at the dispersive focal planes. Full separation of the frag-

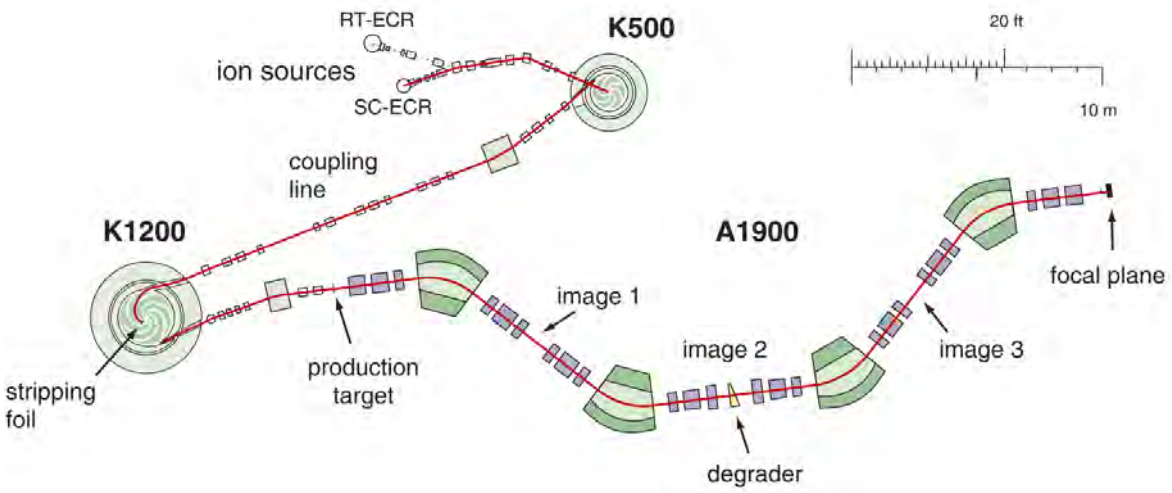

Figure 3.2: Schematic drawing of the A1900 fragment separator and the coupled cyclotrons at NSCL [72].

ments according to their atomic number and mass cannot be achieved solely through the use of the bending magnets. As can be seen from equation 3.1, the fragments are selected based upon the ratio of the momentum to charge. To disentangle these quantities, the fragments are passed through a degrader at the image 2 position. The energy loss of the fragments passing through the degrader is proportional to the square of the charge, specified by the Bethe formula in equation 2.9, so that fragments with different atomic numbers will emerge with different momenta. A wedge shaped degrader is used to maximise the momentum spread of the fragments, as fragments with a greater momentum will pass through more material and therefore experience a greater energy loss. Consequently, a better fragment separation is achieved.

In the second half of the A1900 Fragment Separator, the remaining optical elements enable a complete isotopic separation of the outgoing fragments. In order to allow the identification of individual isotopes on an event-by-event basis, time of flight (TOF) measurements of the secondary beam are measured by the extended focal plane scintillator (X_{FP}), at the focal plane of the A1900. A full overview of the particle identification (PID) of the incoming secondary beam is discussed in section 3.2.1.

3.1.2 S800 Spectrograph

The S800 is a high-resolution, large-acceptance spectrometer at NSCL, that enables the event-by-event tracking and identification of the outgoing fragments from the secondary target [73]. As can been seen from schematic in figure 3.3, the S800 has two main sections:

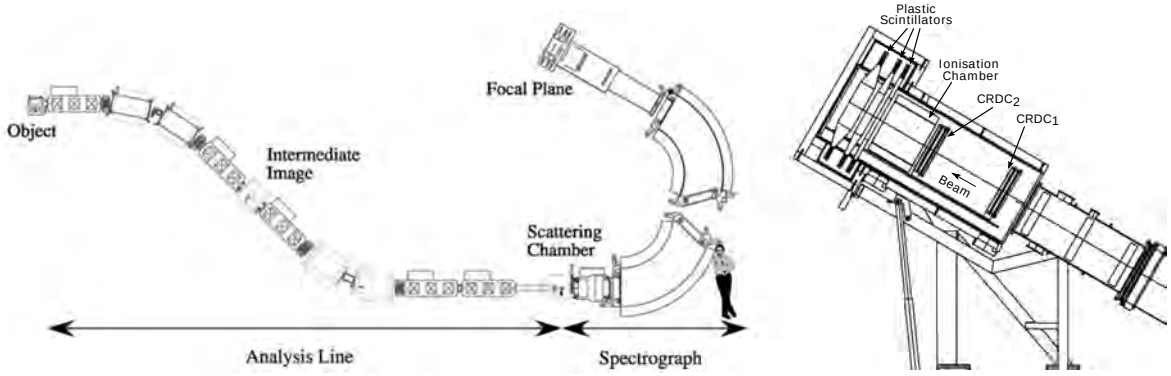

Figure 3.3: Schematic drawings of the S800 (left) [73] and of the detectors at the focal plane (right) [74].

the analysis line and the spectrograph itself. At the focal plane of the spectrograph, there is an array of detectors that are used to identify and track the fragments.

The analysis line is the section that spans from the object station to the target chamber. It has two commonly used modes of operation: the focused mode and the dispersion matching mode. In the focused mode, only the analysis line is achromatic, so that the beam is focused on the target and that the image at the focal plane is chromatic. This means that the momentum distribution of the fragments at the focal plane is set by the momentum width of the incoming beam, modified by the induced momentum change whilst transiting the target. This mode provides the highest momentum acceptance of approximately ± 2%. In the dispersion matching mode, which was used in this experiment, both the analysis line and the spectrograph are tuned to be achromatic. In this mode, the beam at the secondary target is momentum dispersed, resulting in a limited momentum acceptance of less than ±0.5%. However, this mode does provide the greatest energy resolution of the S800.

The spectrograph is located directly after the target chamber, with an angular coverage of approximately 20 msr and a momentum acceptance of about 5%. The spectrograph itself is comprised of the superconducting bending magnets and the detectors at the focal plane position. As opposed to tracking the fragment trajectories through the spectrograph, the S800 relies upon ray reconstruction to correct, event-by-event, for any aberrations introduced by the fringe fields of the magnets [75]. This method requires the inversion of the transfer matrix from the target to the focal plane, calculated by the ion optics code COSY Infinity. These inverse maps link the positions and angles of the fragments, measured by the position sensitive detectors at the focal plane, to their energies, angles and non-dispersive positions at the target. However, the dispersive positions of the fragments at the target position are not able to be deduced. After passing through the spectrograph, the fragments enter the focal plane detectors, which are outlined below.

Focal Plane Detectors

At the focal plane of the S800 is a group of detectors that are used for the tracking and particle identification of the outgoing fragments [74]. The detectors start with pair of position sensitive cathode-readout drift chambers (CRDC), to measure the positions and angles of the outgoing fragments. The first CRDC is located at the position of focal plane of the spectrograph, with the second 1 m downstream. With a position measurement from each of the CRDCs, the fragment trajectory at the target position is able to be deduced, using the inverse mapping described above. The CRDCs are essentially thin gas chambers, with an active depth of 1.5 cm and area of 30 cm × 59 cm. An anode wire spans the boundary of the gas chamber and runs through the 224 cathode pads, as shown in the schematic drawing in figure 3.4. These cathode pads are fundamental to the position sensitivity of the CRDCS. When a charged fragment passes through a CRDC, the gas (80% CF_4 and 20% C_4H_{10} at 40 Torr) contained within becomes ionised, and the electrons are drawn towards to anode wire. As the electrons drift towards the anode wire, they induce a positive charge into the cathode pads. The signals in the cathode pads are then readout to determine the positions of the fragments. The x positions are determined by the pads with the largest signal readout, whereas the y positions are determined by the electron drift time.

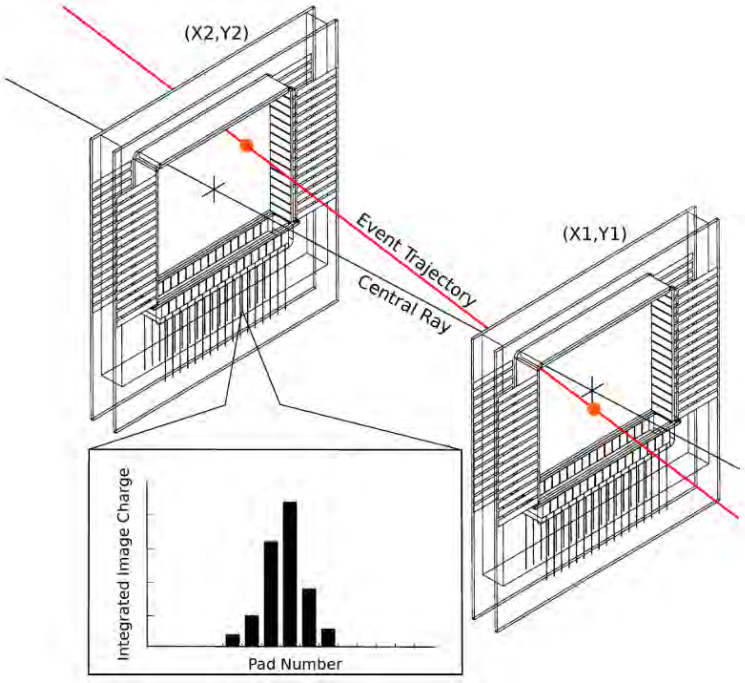

Figure 3.4: Schematic drawing of the pair of CRDCs located at the focal plane of the S800. Measurements of the x and y position from both CRDCs are used to calculate the trajectory of the fragment. The inset demonstrates the determination of the x position to be the pad with the largest signal [75].

After the fragments pass through the CRDC2, they immediately enter the ionisation chamber (IC). The IC has a depth of 41 cm and is segmented by 16 anodes that run perpendicular to the flight path of the fragments. As the outgoing fragments pass through the chamber they ionise the gas, producing electrons and ions. The charge carriers are then collected at the anode and cathode respectively. The number of ionisation events is proportional to the energy lost by the fragment passing through the gas, which is specified by the Bethe formula in equation 2.9, to be proportional to the square of the charge, Z, of the fragment. Therefore, the energy loss of a fragment passing through the IC, enables the determination of it's atomic number.

After the IC, a plastic timing scintillator E1 was installed, which provided the main trigger for the data acquisition (DAQ) system in this experiment. The trigger conditions were set to record the γ-ray data in coincidence with a fragment event at the E1 scintillator, and the S800 singles events with a downscale factor of 5. Timing measurements from the E1 in conjunction with the measurements from the object station scintillator (OBJ), enabled the measurement of the time of flights (TOF) of the fragments.

3.1.3 GRETINA

The Gamma-Ray Energy Tracking in-beam Nuclear Array (GRETINA) is a state-of-the-art γ-ray tracking detector array, that was used to study the γ rays emitted in-flight, by the excited ^{23}F fragments [76]. By making use of sophisticated tracking algorithms, which will be expanded upon further in this section, GRETINA is able to produce high-resolution γ-ray spectra, with excellent peak-to-total ratios [77]. Additionally, these algorithms also allow GRETINA to track the three-dimensional positions of the γ-ray interactions within the germanium, to a position resolution of approximately 2 mm. This enables a good reconstruction of the detection angles, which is crucial to achieve a good Doppler corrected spectrum, see section 2.3.1.

Each module of GRETINA consists of four highly-segmented, high-purity germanium (HPGe) crystals [78]. The crystals begin in a cylindrical form at the base, that tapers towards the front, to one of two irregular hexagonal shapes; type A or type B, see schematic in figure 3.5. The coaxial design of the crystals enables them to be arranged in a close-packed formation, so that the hexagonal shapes tessellate to form a closed surface of HPGe surrounding the target chamber, as the photograph in figure 3.6 demonstrates. Each GRETINA crystal is electrically segmented 36 times, with five transverse and six longitudinal segmentation lines, illustrated by the schematic in figure 3.5. Therefore, for every crystal there are 37 contact signals, one from each segment, and from the central contact, which are individually

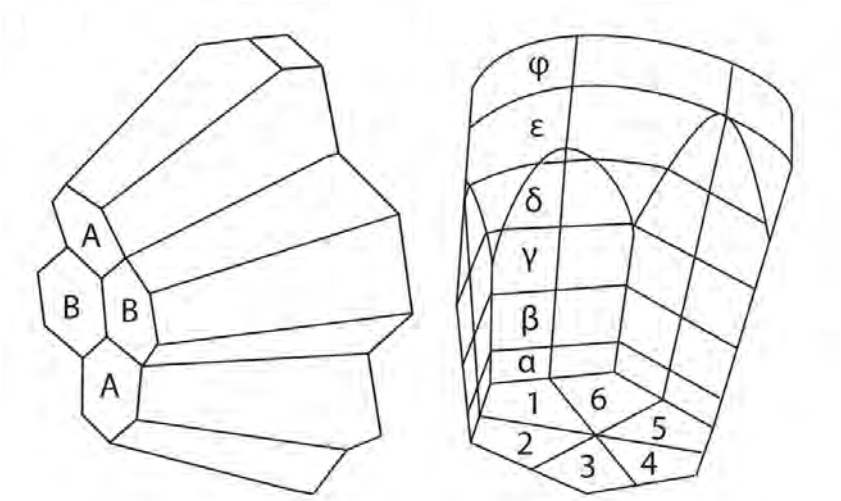

Figure 3.5: Sketch of a GRETINA module (left) with the four crystals arranged into two irregular hexagonal shape and a drawing of a single GRETINA crystal (right) demonstrating the electrical segmentation [78].

Figure 3.6: Photograph of an open hemisphere of GRETINA with 6 modules visible. The slots in the frame into which the modules are mounted can be seen, as well as the tight configuration of the crystals. This hemisphere may be closed with the one out of view of the picture so that the crystals surround the target chamber.

read out. These signal readouts from the segments are crucial to the tracking functionality of GRETINA, which will be discussed in the following few sections below.

For the experiment being discussed in this analysis, nine GRETINA detector modules were available, resulting in a solid angle coverage of approximately 1.2π sr. As the primary objective of this experiment was to measure the lifetimes of the excited states in ^{21}O, the target was shifted 13 cm upstream from the nominal position. This had the effect of

shifting the detection angles further forwards, thus increasing the sensitivity of the Recoil Doppler Method (RDM) setup, see section 2.4. With respect to the new target position, four of the modules were covering detection angles of approximately 40 degrees and the other five were placed at approximately 60 degrees. Additionally, for this experiment, lead plates were attached to the faces of the GRETINA modules, which acted as shields to mitigate the high rates of low-energy γ rays produced during the experiment.

3.1.4 Germanium Detectors

The fundamental operation of GRETINA is that of a highly-segmented, high-purity Germanium (HPGe) detector. Germanium is a semi-conductor detector material that is heavily favoured for high-resolution γ-ray spectroscopy [58]. Germanium detectors significantly outperform scintillators in terms of γ-ray energy resolution and are preferred over silicon detectors due to the photoelectric absorption cross section being approximately 60 times greater in germanium ($Z_{\mathrm{Ge}}^5/Z_{\mathrm{Si}}^5 = 32^5/14^5 \approx 60$), see section 2.2.2, as well as the higher achievable material purity. This section will briefly outline the key characteristics of germanium detectors and their response to an incident γ-ray interaction within the detection medium.

When a reverse-bias voltage (negative voltage to the p-region and positive voltage to the n-region) is applied to a p-n junction in a semiconductor detector, the depletion region in the detector is increased. The depletion region is a layer in which there are no free charge carriers, and constitutes the sensitive area for the detection of radiation. For γ-ray spectroscopy, it is necessary to maintain a large depletion region for effective charge collection and detection efficiency of the γ rays. The width of the depletion region d, for a specified reverse-bias voltage V, is given by

$$d = \left(\frac{2\epsilon V}{eN}\right)^{1/2}, \tag{3.2}$$

where ϵ is the dielectric constant, e is the electron charge and N is the net impurity concentration. Clearly, to increase the depletion region for a set voltage, the net impurity concentration, N, must be reduced as much as possible. Therefore, high-purity germanium (HPGe) is often used. The HPGe crystals used in GRETINA have less than 1.8×10^{10} cm^{-3} net impurity concentration.

When an incident γ-ray photon interacts within the depleted region of a reverse-biased HPGe detector, free charge carriers (electrons and holes) are produced, which drift in the

electric field, towards their respective electrodes. This flow of the charge carriers constitutes a small current, which is passed through a charge-sensitive preamplifier to get the signal. This signal is dependent on the number of charge carriers, which itself is proportional to the energy deposited by the γ ray in the interaction. As the electron allowed-energy band gap in germanium, see figure 3.7, is smaller than that of silicon, more charge carriers are produced for the same energy deposition. Consequently, a γ-ray energy spectrum taken by a germanium detector will have a greater energy resolution, than one taken by a silicon detector. However, because of the small band gap in germanium, the detectors must be cooled to temperature of approximately 77 K, to limit the leakage current caused by the thermal generation of the charge carriers. Without cooling, the energy resolution of the detector would be severely hampered by the noise induced by the leakage current [58].

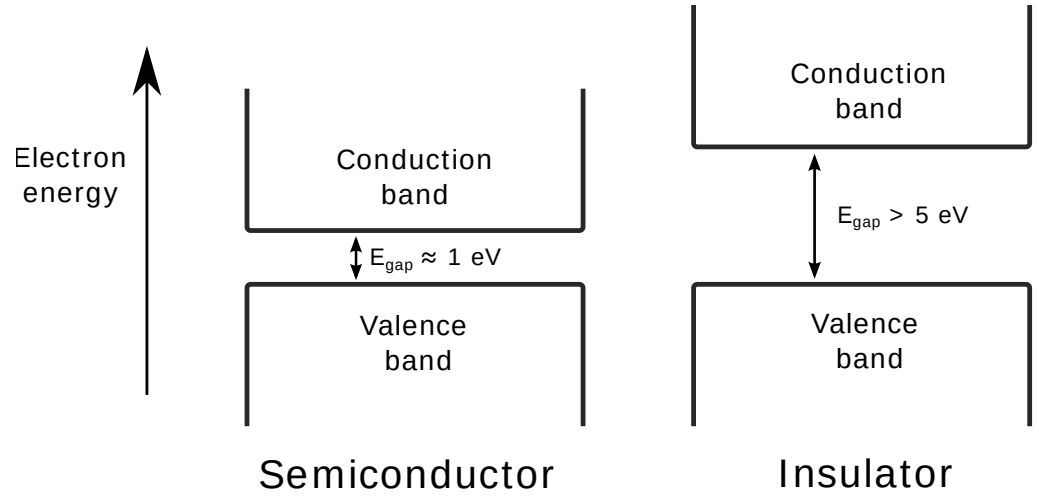

Figure 3.7: A simple sketch of the electron allowed-energy band structure, highlighting the difference in the band gap for a semiconductor material and an insulator. The electrons must be excited from the valence band to the conduction band, across the band gap, to freely move about the crystal. The smaller the band gap, the more charge carriers are produced from the same energy deposition.

The detector crystals in GRETINA are comprised of an n-type HPGe material, in a coaxial (cylindrical) geometry, see figure 3.8. The coaxial configuration enables a much larger active detection volume, and allows the crystals to be closely packed to one another. In such a configuration, the outer surface of the crystal is the p^+ contact, whilst an inner cylindrical surface is the n^+ contact. When the reverse-bias voltage is applied, the central contact becomes the anode, to which the electrons are drawn, and the outer contact becomes the cathode, which collects the holes.

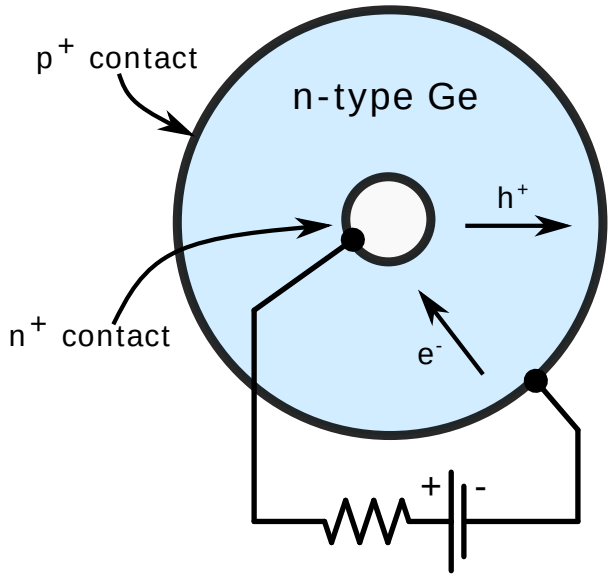

Figure 3.8: A simplified sketch of an n-type HPGe coaxial detector, highlighting the n+ and p+ contacts and the drift directions of the charge carriers.

3.1.5 GRETINA Tracking

The ability of GRETINA to effectively determine the interaction positions of the γ rays within the detector material, and thus effectively track them, sets it apart from other γ-ray detector arrays (except for AGATA [79]). This ability to track enables a good add-back of γ-ray interactions across crystals and the identification and rejection of the partially absorbed γ rays that Compton scatter out of the detector material. This leads to GRETINA having a high detection efficiency and an excellent peak-to-total ratio. Furthermore, the high position resolution with which the point of the first interaction of the γ ray within the detector volume can be determined (i.e. the interaction with the highest energy deposition), enables the accurate reconstruction of the detection angle of the γ ray, with respect to the fragment trajectory. The importance that this quantity has on the resolution of the peak, post Doppler correction, is described in detail in section 2.3.1.

When a γ ray interacts within the HPGe crystals of GRETINA, the electron-hole pairs are created and separated by the bias voltage. The electrons drift towards the central contact, whilst the holes drift towards the outer surface. The anode at the central contact will generally collect the full charge from the electrons, however the outer contacts often share the charge into the neighbouring segments. The time dependency and shape of the signals, read out from each segment, are sensitive to the position of the γ-ray interaction within the detector volume [80]. Therefore, by looking at all of the signal waveforms, it is possible to determine the position of the interaction, even to within a segment. However, γ rays usually interact several times within the crystals, with each interaction creating its own set of

signals. The readout pulse then becomes a superposition of the generated signals from the individual interaction points. A method called signal decomposition is then applied to this pulse, in order to determine the position of each interaction point [78]. In brief, this process entails the comparison of the measured signals to a library of simulated single-interaction-point pulses. The end result is the real-time recovery of the number of γ-ray interactions, and their three-dimensional positions within the detector crystals.

The tracking algorithms are then applied in order to associate the interaction points to individual γ rays and reconstruct their trajectories and energies. The details of the tracking algorithms can be found in [81]. In brief, the interaction points are grouped into clusters that are likely to have originated from a single γ ray. The energy-angle relationship in the Compton scattering formula, see section 2.2.2, is exploited to link these interactions points. Each potential sequence of interactions is assigned a figure of merit (FoM) value, to describe the likelihood of the γ ray following that sequence. The FoM value is determined by the deviation of the measured energy deposited and scattering angle of the γ ray, from the expected values given by the Compton scattering formula. By minimising the FoM, this algorithm determines the most probable interaction sequence for the given interaction points, thus tracking the path of the γ ray through the detector. The type of algorithm, described above, is known as a forward tracking algorithm [82]. There are alternative methods, such as the backward tracking algorithms, which track the γ rays starting from the end of the interaction sequences [83]. Either way, the end result of the tracking algorithms, is the extraction of the energies of the γ rays and their trajectories through the detector crystals. This enables a good add-back of the γ-ray interactions across the crystals and the removal of γ rays which Compton scatter out of the crystals. Thereby, improving the detection efficiencies and peak-to-total ratios of the entire detector array.

3.2 Data Analysis

This section outlines the methods and techniques that were employed for the analysis of the data. Specifics on the particle identification of the incoming and outgoing fragments, as well as the energy and efficiency calibrations of GRETINA are covered. The Doppler correction and subsequent analysis of the γ-ray spectrum of the ^{23}F fragments is then discussed, followed by an outline of the γ-γ coincidence analysis and the γ-ray angular distributions. Each technique that was made use of during the analysis is reviewed, alongside any approximation that were made. The data was initially unpacked using the GrROOT package [84], with the rest of the analysis performed using ROOT [85]. Prior to the work presented in this

section, the data was calibrated and the CRDCs were gain matched and drift adjusted by Sebastian Heil [70]. The results of the analysis are presented in section 3.3, followed by the discussion in section 3.4.

3.2.1 Particle Identification

The scintillation detectors at the focal plane of the A1900 (X_{FP}), and the object (OBJ) and focal plane stations (E1) of the S800, were used for the event-by-event particle identification (PID) of the incoming and outgoing fragments. For the incoming PID, the time of flight (TOF) from the X_{FP} scintillator to the E1 was plotted against the TOF from the OBJ scintillator to the E1, see figure 3.9. The diagonal lines in the PID plot denote the incoming fragments with the same velocities. The ^{24}F fragments are easily identifiable in this plot due to the high purity ($\approx$ 95%) of the secondary beam.

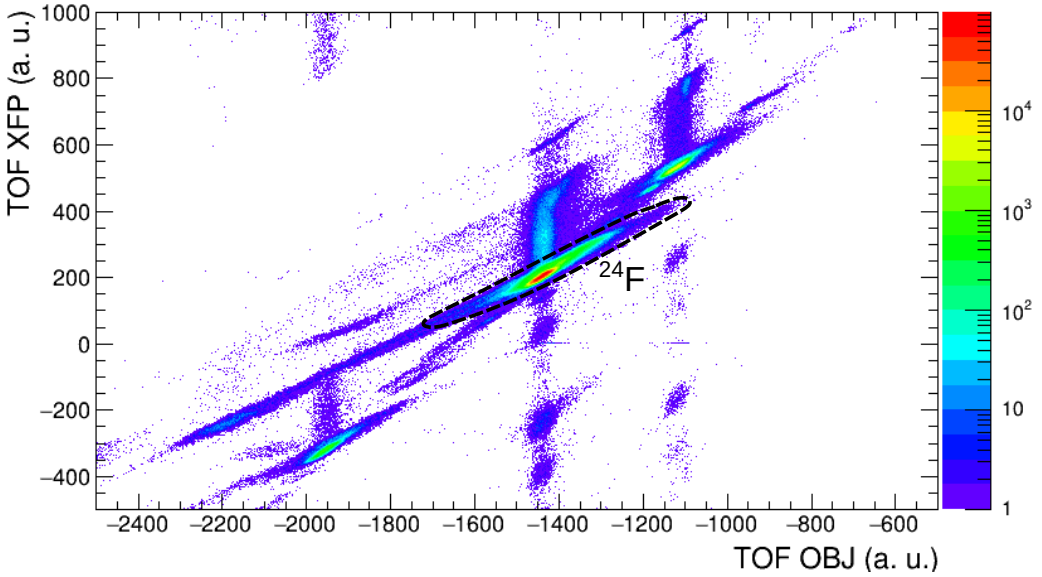

Figure 3.9: Incoming particle identification plot. The TOF of the fragments from the X_{FP} scintillator to the E1 is plotted against the TOF from the OBJ scintillator to the E1. The incoming ^{24}F fragments are labelled and the cut is indicated by the dotted black line.

The outgoing fragments were also identified using the TOF from the OBJ scintillator to the E1 station. However, a correction had to be applied to this TOF to account for the trajectories of the outgoing fragments. The momentum change induced by the reactions in the target resulted in the outgoing fragments taking different flight paths through the S800, therefore having different TOFs. The plots on the left side of figure 3.10 demonstrate a correlation between the TOFs of the fragments transiting the S800 and their dispersive positions

(X_{FP}) and angles (A_{FP}) at the focal plane. With this correlation, the left plot of figure 3.11 shows that it was impossible to clearly identify the outgoing fragments, simply by plotting energy loss through the ionisation chamber (ΔE_{IC}) against the TOF. Therefore, the fragment TOFs were corrected according to the function

$$\mathrm{TOF}_{\mathrm{corr}} = \mathrm{TOF} + a_X \times \mathrm{X}_{\mathrm{FP}} + a_A \times \mathrm{A}_{\mathrm{FP}}\,. \tag{3.3}$$

Where the factors $a_X = 0.157$ mm^{-1} and $a_A = 1.61$ mrad^{-1} were set to remove the TOF correlations [70]. The plots on the right of figure 3.10 show that the corrected TOFs are now independent of the position and angle of the fragment at the focal plane. Consequently, the outgoing PID, constructed by plotting the ΔE_{IC} against the corrected TOF, now shows distinct and separate structures for each outgoing fragment, according to their charge and mass. This enabled the simple identification and selection of the ^{23}F, see the right plot of figure 3.11.

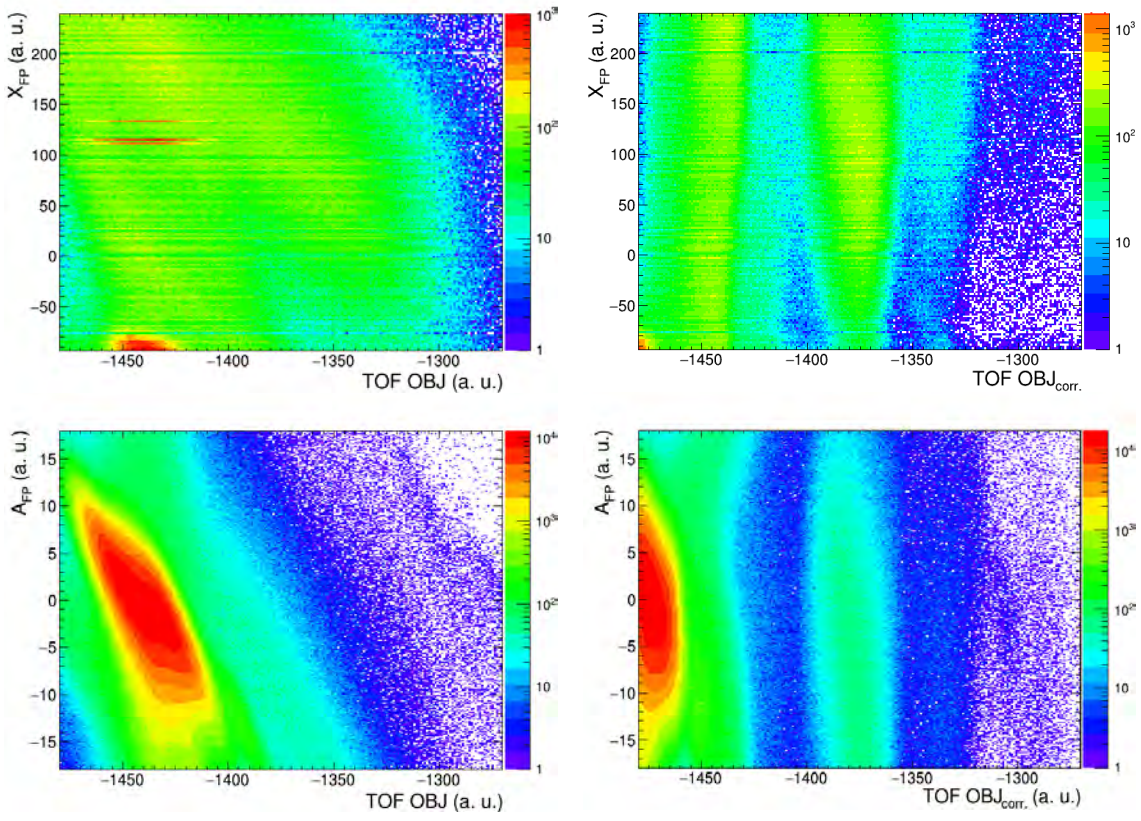

Figure 3.10: The dispersive positions X_{FP} and angles of the fragments A_{FP} at focal plane of the S800 are plotted against the time of flight from OBJ to the E1 scintillator. The images on the left highlight the correlation with the position and angle when the TOF corrections are not applied. The plots on the right show that when the corrections are applied, the correlations are removed.

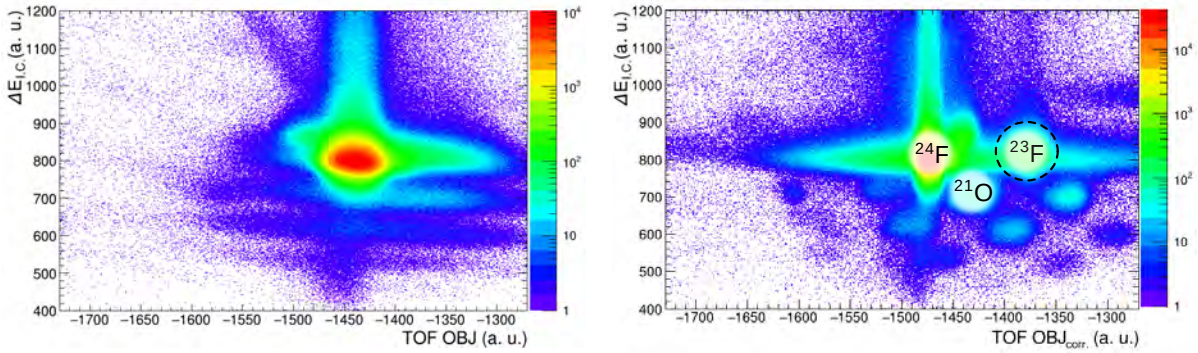

Figure 3.11: The outgoing particle identification plots. The energy loss of the fragments passing through the ionisation chamber is plotted against the uncorrected (left), and corrected (right) TOF from OBJ to E1. The plot on left clearly demonstrates that without first correcting the TOF of the fragments, to account for their trajectories, it is impossible to discern any clear structures in the PID plot. The plot on the right shows that with the TOF corrections applied, the individual isotopes can then be identified and selected. The strongest channels are labelled in the PID and the cut used to gate on the outgoing ^{23}F fragments is indicated by the dotted black line.

3.2.2 GRETINA Energy Calibration and Efficiency

Measurements of the ^{56}Co and ^{152}Eu sources, at the target position, were carried out for the energy and efficiency calibration of GRETINA, the spectra from which can be seen in figure 3.12. The calibration was determined to have a precision of generally better than 0.1% across the measured energy range, with good agreement between the measured and expected γ-ray energies of the sources [86], as demonstrated in figure 3.13. However, due to the limited energy range of the two sources, any γ rays that were detected in the experiment with energies greater than 3.5 MeV, will have had some systematic uncertainty introduced into their measurement from the calibration.

For the accurate determination of the relative intensities, branching ratios and angular distributions, it was essential that the γ-ray detection efficiencies were properly calculated and corrected for. In this analysis, the absolute detection efficiencies were unable to be accessed, as in the course of the experiment, the scalars were not accurately recorded. However, the relative detection efficiencies could still be ascertained. Furthermore, as the GEANT4 simulations used extensively throughout this analysis, see section 3.2.7, could not replicate the tracking functionality of GRETINA, the relative efficiencies here are obtained using the single-crystal analysis. In order to plot the relative efficiency curve for GRETINA,

the ^{56}Co and ^{152}Eu calibration sources were used. By measuring the intensities of the transitions on the spectra shown in figure 3.12, and adjusting for the known relative intensities of the γ rays [86], the relative detection efficiencies were calculated. The detection efficiencies of the γ rays from the ^{56}Co source were calculated relative to the 846.7 keV transition and the ^{152}Eu γ rays relative to the 876.4 keV transition.

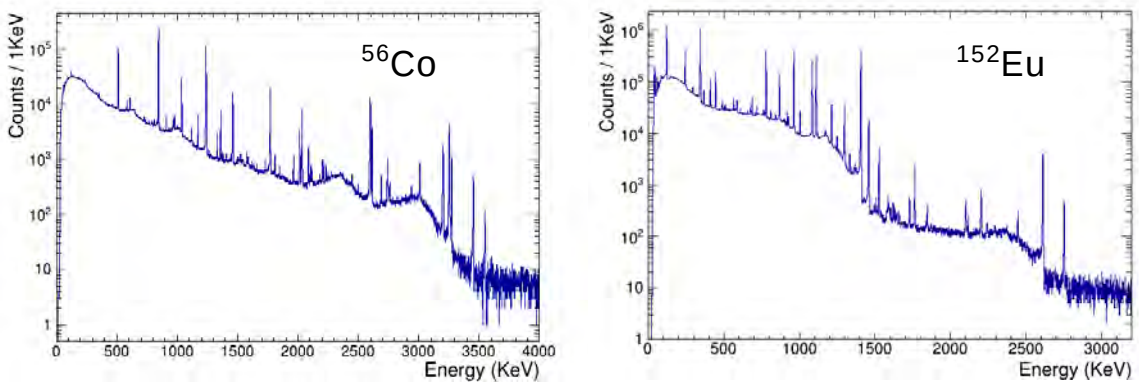

Figure 3.12: ^{56}Co (left) and ^{152}Eu (right) source measurements for the GRETINA energy and efficiency calibrations.

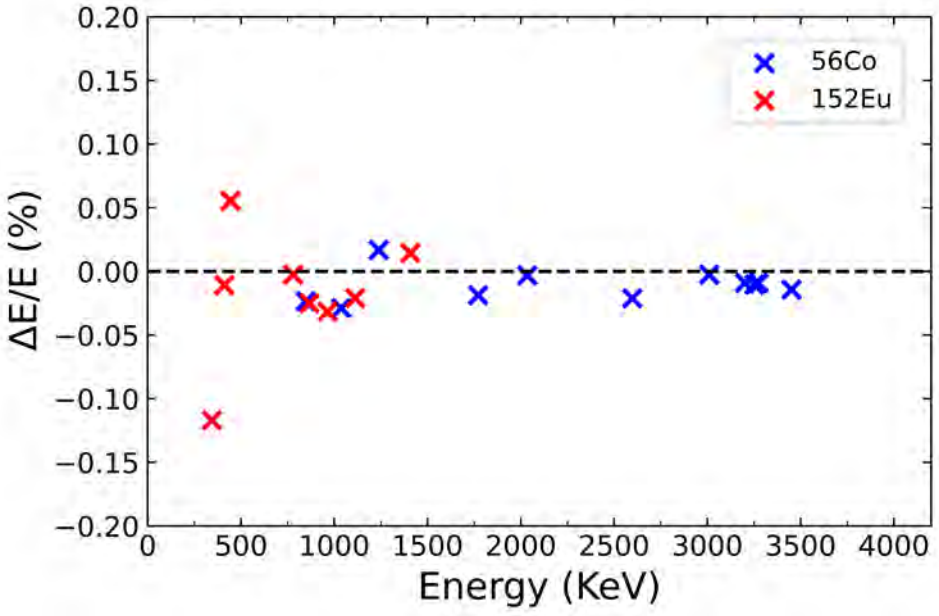

Figure 3.13: The relative difference of the measured energies from the expected γ-ray energies of the ^{56}Co and ^{152}Eu sources, for each transition. The plot shown constitutes a measure of the quality of the energy calibration of GRETINA. In general, most of the measurements across the energy range are within 0.1% of the expected values.

In this way the sources were effectively normalised to each other, as the two transitions have a similar energy, so a single continuous efficiency curve could be plotted, see figure 3.14. The relative efficiency curve given by equation 3.4, was fit to the data to enable the determination of the relative detection efficiency for any γ-ray energy.

$$\ln\epsilon = \sum_{i=1}^{N} a_i \left(\ln\frac{E}{E_0}\right)^{i-1} \tag{3.4}$$

Where E_0 is a fixed reference energy and the values of a_i are the fitted parameters. Using the 846.7 keV transition as the reference energy, it was found that the 5th order of the equation minimised to be the best fit, where the coefficients are a_1 = 0.0135, a_2 = -0.4584, a_3 = -0.0639, a_4 = -0.04 and a_5 = -0.0223.

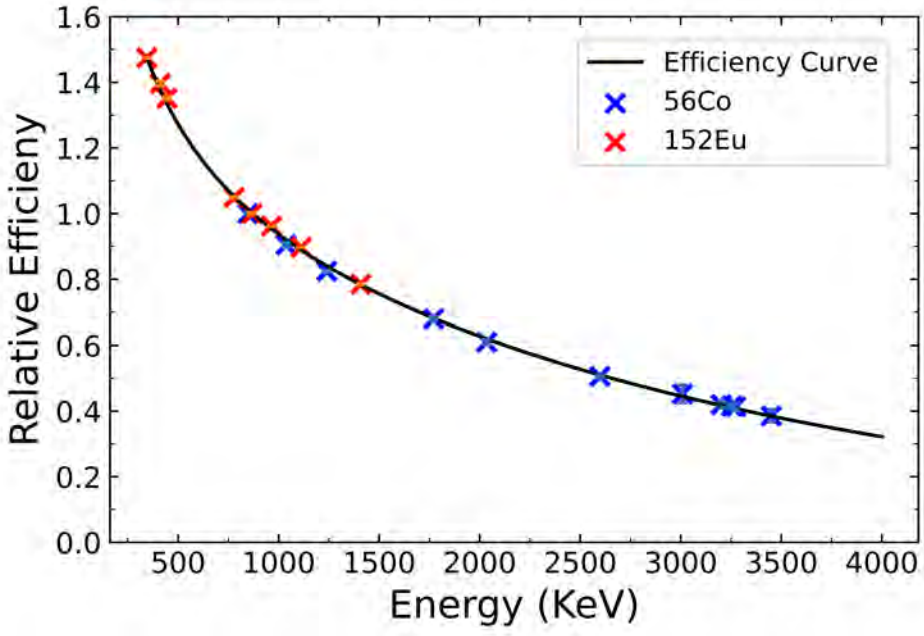

Figure 3.14: The relative detection efficiencies from the single-crystal analysis, plotted over the γ-ray energies for the ^{56}Co and ^{152}Eu sources. The efficiency curve given by equation 3.4 has been fitted to the data.

3.2.3 Doppler Correction

The γ rays emitted in-flight, by the de-excitation of the ^{23}F nuclei, were detected by the GRETINA array surrounding the target chamber. The high velocities of the excited ^{23}F fragments at the instance of emission, resulted in the significant Doppler shift of the emitted γ rays. Consequently, the detected γ-ray energies in the laboratory frame, emitted by the ^{23}F, were greater at the smaller detection angles relative to the beam-axis direction. This effect

is described by the relativistic Doppler shift expression in equation 2.13.

The measured lab-frame γ-ray energy spectrum is displayed in figure 3.15. The peak structures that can be seen on the spectrum predominantly originate from neutron-induced reactions on aluminium and germanium. The corresponding structures on the inset are straight, indicating that the detected energies are independent of the angle at which they were detected, and thus are not Doppler shifted. The aluminium and germanium, from which the majority of these peaks originate, are ubiquitous within the experimental setup. Aluminium constitutes the primary structural material from which the beam tubes, detector frames, casings and chambers are constructed, whilst germanium is the detector material of the GRETINA modules. The peaks originating from the neutron inelastic scattering from germanium can be identified on the γ-ray spectrum, as they have a distinctive triangular shape. This is due to the energy of the nuclear recoil being measured in addition to the γ-ray energy [87].

The inset of figure 3.15 demonstrates that the γ rays from ^{23}F have a clear correlation between their measured energies and the angle at which they were detected, due to the relativistic Doppler shift. Thus, on the lab-frame γ-ray spectrum, these peaks are smeared out into the smooth background. In order to recover the peak structures of the γ-ray transitions of ^{23}F, from which their energies and intensities could be measured, the detected γ-ray energies were Doppler corrected, see section 2.3.1.

The Doppler correction of the γ-ray energies was carried out on an event-by-event basis. As the exact location along the z-axis of the ^{23}F fragments at the instance of decay could not be known, the centre of the 2 mm ^{9}Be target was taken to be the z-coordinate of the decay position. The beam direction was defined as the vector from this point, to the position of the fragments at the entrance of the S800. Similarly, the γ-ray directions were defined to be the vector from the decay position, at the centre of the target, to the position of the first interactions of the γ rays with GRETINA. This was defined to be the position of the interaction with the largest energy deposition for the spectra using the tracking functionality of GRETINA, or to be the crystal with the largest energy deposition, for the single-crystal spectra. Either way, from these two vectors, the detection angles could be reconstructed. The other variable necessary for the Doppler correction, the average emission velocity $\langle\beta\rangle$ = 0.4175, was set to be the velocity required for the γ-ray energies to be equal to the expected rest-frame energies, and to be independent of the angle at which they were measured. Several of the most intense transitions across the spectrum were used for this purpose, to remove the possibility of introducing a systematic uncertainty to the spectrum, due to the reference transitions having a lifetime effect. The resulting Doppler corrected γ-ray spectrum is displayed in figure 3.16.

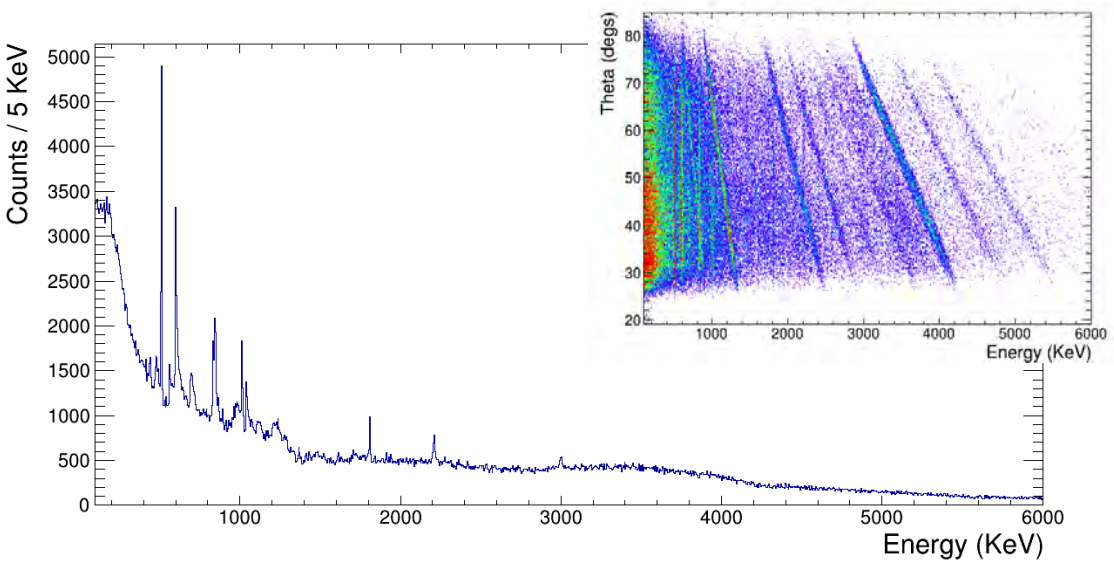

Figure 3.15: The lab-frame γ-ray spectrum. The inset shows a plot of the detection angle against the detected γ-ray energy. For the ^{23}F transitions, there is a clear correlation between the detected γ-ray energies and the detection angles. Consequently, the ^{23}F peaks are smeared out into smooth curves across the spectrum. The sharps peaks that are clearly visible on the spectrum, originate from the neutron-induced reactions on aluminium and germanium.

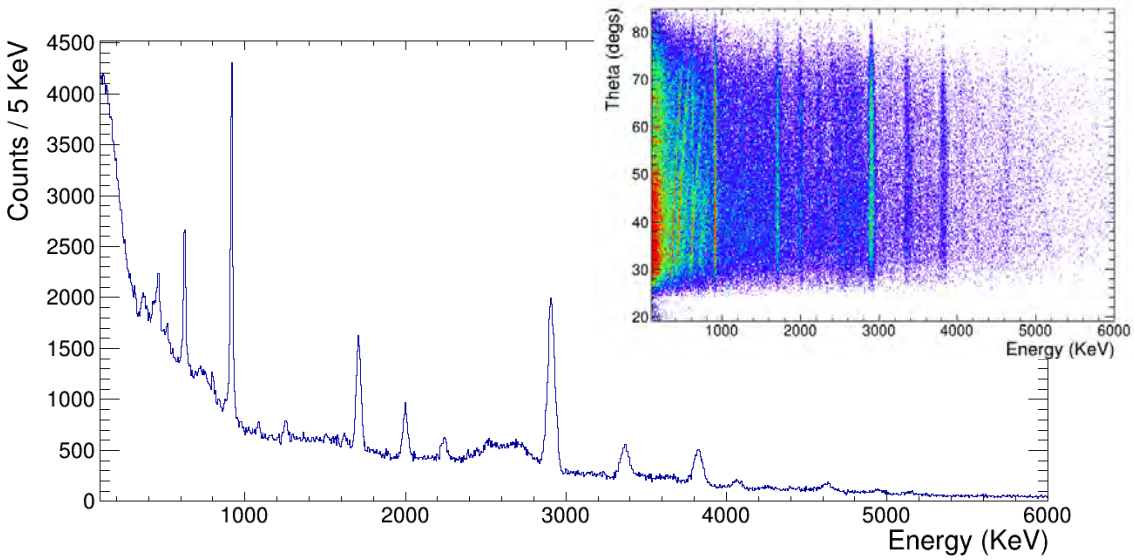

Figure 3.16: The Doppler corrected γ-ray spectrum, using the full tracking capabilities of GRETINA. The inset now shows that the correlation between the detection angle and the γ-ray energy has been removed. Therefore, the Doppler reconstructed peaks are now visible on the spectrum.

The Doppler reconstructed γ-ray spectrum for ^{23}F, displayed in figure 3.16, demonstrates the removal of the correlation between the γ-ray energies and their detection angles, and the recovery of the peak structures for the ^{23}F transitions. Inversely, the peaks from the neutron inelastic scattering reactions on aluminium and germanium are now smeared across the angles, and form broad background structures in the low-mid energy regions of the γ-ray spectrum.

The apparent reduction in the energy resolution of the γ-ray spectrum post Doppler correction, that can be observed when comparing the spectra, was explained in section 2.3.1 to be a consequence of the uncertainties in the Doppler correction parameters. In the experiment, the uncertainties in the detection angles were minimised through the use of GRETINA. The ability of GRETINA to effectively determine the positions of the first interactions of the γ rays, to a resolution of 2-3 mm, significantly reduced the contribution of this uncertainty to the broadening of the peaks. In addition, the approximation of the decay position being in the centre of the target, is generally valid for transition with lifetimes that are much shorter than the transit time of the excited fragments through the target. If there were any transitions with lifetimes on the order of, or greater than the fragment transit time ($\tau > 15$ ps), then this approximation would induce a significant uncertainty in the detection angle, and a lifetime-sensitive lineshape would appear in the spectrum. Finally, the uncertainty in the Doppler correction velocity arises on account of the emission velocities being a distribution. This distribution was a convolution of initial momentum distribution of the fragments, with the energy loss effects through the target. The contribution of this uncertainty was minimised by selecting as close as possible to the mean emission velocity of the distribution.

3.2.4 γ-ray Spectrum Analysis

The Doppler corrected γ-ray spectrum was systematically analysed through the fitting of Gaussian curves to the peaks, with an approximated linear background, of the form shown in equation 3.5. From these fits, the γ-ray transitions in ^{23}F were identified, and the centroid energies and Full Width Half Maxima (FWHM $\approx 2.35\sigma$) of the peaks were measured. Additionally, from the fitting of symmetric Gaussians to the data, it can be can be inferred that there were no strong lifetime effects present in the measured transitions.

$$f(x, a, \mu, \sigma, b, c) = ae^{-\frac{(x-\mu)^2}{2\sigma^2}} + bx + c \tag{3.5}$$

Where a is the height of the Gaussian, μ and σ are the centroid energy and standard devia-

tion respectively. The free parameters b and c, describe the linear background upon which the Gaussian sits.

The fits were carried out using the Minuit fitting package, built into the ROOT data-analysis framework [85]. The least squared technique was used to minimise the fit and extract the observables. The basic principle of this technique is to minimise the following χ^2 function, with respect to the free parameters.

$$\chi^2 = \sum_{i=1}^{n} \frac{(y_i - f(x, \mathbf{a}))^2}{\sigma_i^2} \tag{3.6}$$

Where y_i are the measurements and σ_i are their uncertainties, f is a function of x and an array of free parameters to be fitted $\mathbf{a} = (a_1 + a_2 + a_3 + a_4 + ...)$. The optimum parameters are defined as the values which return the χ^2 at a minimum. The curvature of the function in the vicinity of the minimum, provides information regarding the uncertainties in the parameter values.

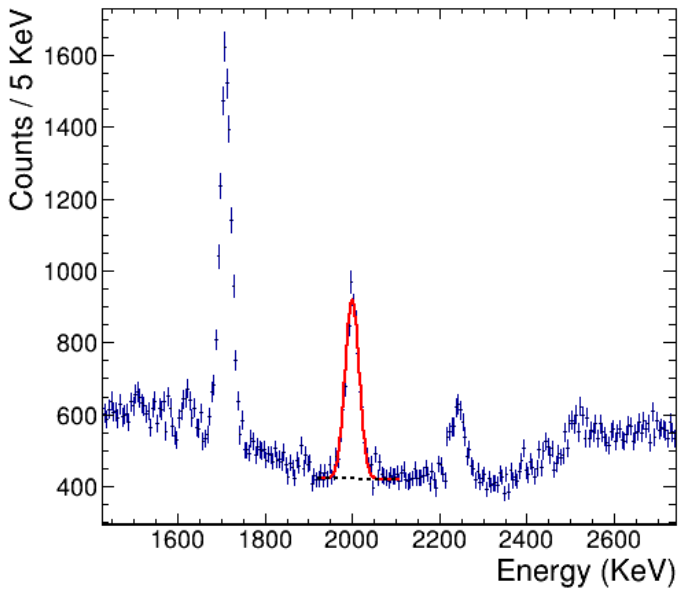

Figure 3.17: Plot of an example fitting of the 1999 keV transition in ^{23}F. The peak is fit using a Gaussian on top of an assumed linear background. The background subtraction of the peak can be carried out by the subtraction of the integral of the linear component from the integral of the total function.

In principle, the intensities of the γ-ray transitions could be measured from these fits, by performing a background subtraction on the peaks. As demonstrated by figure 3.17, this would entail the subtraction of the integral of the linear background component, from the integral of the entire function. However, the peaks on the Doppler corrected γ-ray spectrum

often had complex background functions. This was due in part to their broadness, causing them to merge with the other structures on the spectrum; such as the neutron inelastic scattering peaks and the Compton structures and escape peaks of other nearby transitions. This made the linear background approximation significantly less valid and would constitute the dominant source of uncertainty in the intensity, and thus branching ratio measurements. Therefore, detailed Monte Carlo simulations were carried out, with the γ-ray energy measurements as inputs, to extract not only the relative intensities of the transitions, but also the relative populations and branching ratios of the excited states in ^{23}F, see section 3.2.7.

3.2.5 γ - γ Coincidence Analysis

The excited states of nuclei do not necessarily decay directly to the ground state with the emission of a single γ ray. Many transitions form part of a cascade, a chain of decays in series, emitting two or more γ rays in coincidence. Before being able to deduce the relative populations and branching ratios of the excited states in ^{23}F via the simulations, the cascades first had to be identified. For this purpose, a γ-γ coincidence matrix was constructed, with GRETINA tracking, to determine which γ rays were detected in coincidence, see figure 3.18. In principle, this technique could be expanded to the observation of the γ rays detected in coincidence with several other γ rays, a γ-γ-γ cube for instance. However, in practice this is limited by the fact that the efficiencies are multiplicative. In this case, this means that the limited geometrical coverage of GRETINA results in a reduced γ-γ efficiency. Consequently, only the cascades with the most intense transitions were able to be identified.

In order to observe and measure the cascades, the previously measured transition energies were gated upon. The peaks on the resulting gated spectra were then fitted, and the cascades deduced. Figure 3.19 displays each of the steps involved in the γ-γ coincidence analysis. The first step was to define a "data gate" around the energy of a transition, between the red lines in the top left panel. A background subtraction was then carried out, so that only the transitions in coincidence with the gated transition energy were visible upon the gated spectrum. The background subtraction was performed by defining the background gates as the regions directly adjacent to the data gate, denoted by the black lines. The background gates were then summed, scaled and then subtracted from the data gate, to produce the background-subtracted spectrum shown in the bottom right panel. The analysis of these gated spectra, coupled to the prior analysis of the γ-ray spectrum, enabled the construction of a new level scheme for ^{23}F, which is presented in figure 3.31.

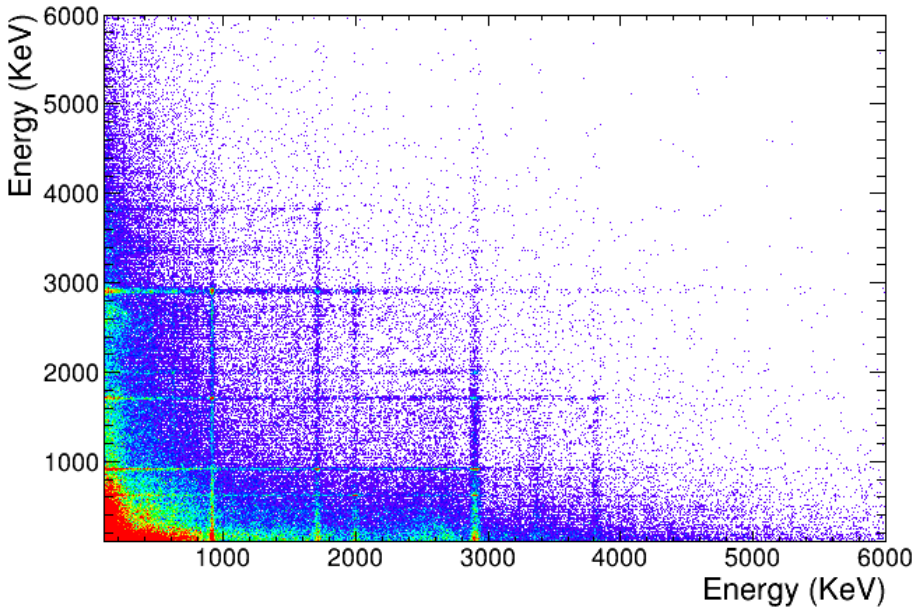

Figure 3.18: γ-γ coincidence matrix for ^{23}F.

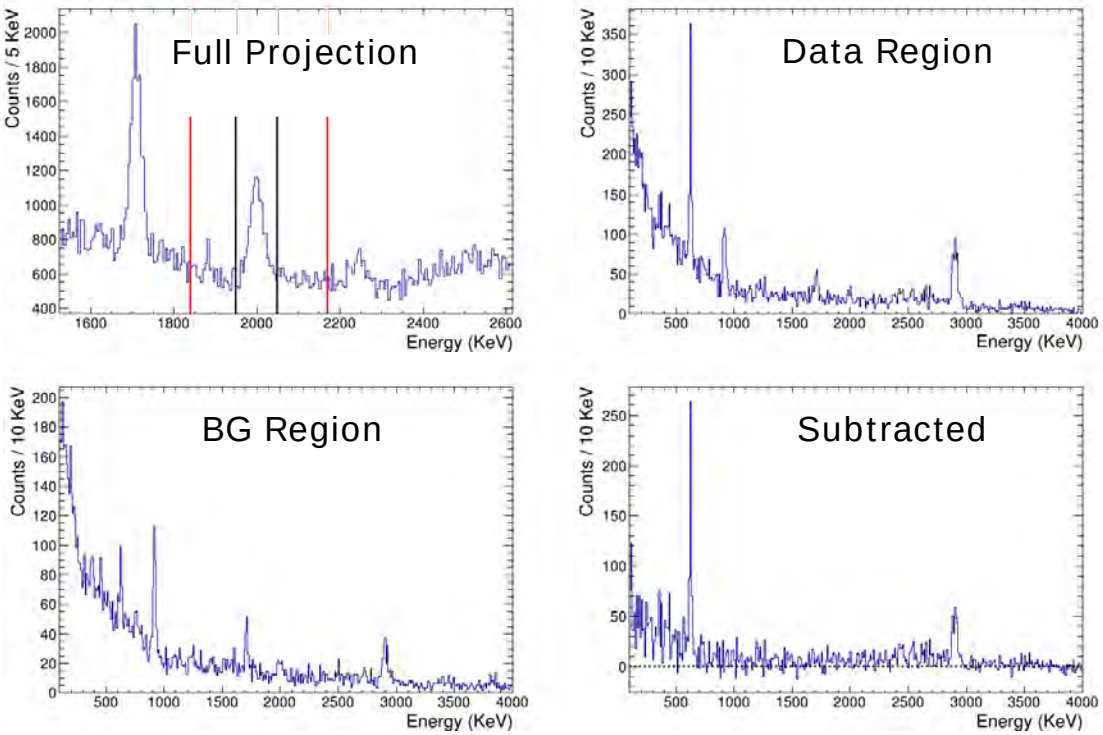

Figure 3.19: Example of γ-γ coincidence analysis. The top left panel is the full projection of the γ-γ matrix, where the black and red lines denote the "data" and "background" regions respectively. The spectra for the γ rays in coincidence with these regions are displayed in the top right and bottom left panels, with subtracted spectrum in the bottom right.

3.2.6 γ-ray Angular Distributions

The measurement of the angular distributions of the γ-ray transitions, emitted from the nuclear excited states, is an important tool in nuclear structure research. Indeed, by studying the γ-ray angular distributions, the multipolarities of the transitions are able to be derived. Thus, enabling the assignment of spins to the excited states. The one-neutron knockout reactions of ^{24}F populated aligned excited states in the ^{23}F fragments, the transitions from which had measurable angular distributions. A nuclear state is said to be oriented if there is a preferential relative population of the m-substates, so that $P(m) \neq P(m')$. In the circumstance where $P(m) = P(-m)$, the state is said to have an alignment [88].

In the following subsection there is a brief summary of the principles and framework required to interpret the angular distribution data, and an outline of the commonly used notation. A complete discussion of the γ-ray angular distributions for intermediate-beam energies can be found in [89, 90].

Angular Distribution Framework

The orientation of a state of interest, with a spin I, is specified by a statistical tensor. A statistical tensor describes a collection of nuclei in a specific state, and is related to the distribution of magnetic substates, with respect to a chosen coordinate frame. In this analysis, the coordinate frame is chosen be with the beam directed along the positive z-axis. The magnetic substate distribution is given by the populations $P(m)$ of the $2I+1$ m-substates, which are normalised so that $\sum_m P(m) = 1$. For an axially symmetric m-substate distribution, the statistical tensor B_k is defined by

$$B_k(I) = \sqrt{(2I+1)} \sum_m (-1)^{I+m} \langle I - m I m | k 0 \rangle P(m) \,, \tag{3.7}$$

where $k = 0, 1, 2, ..., 2I$ if I is an integer spin, or $k = 0, 1, 2, ...2I-1$ if I is a half-integer spin. For an aligned state, where $P(m) = P(-m)$, only the statistical tensors with even values of k are non-zero [90].

In the circumstance where the orientation of an excited state of interest is due to several different population channels (i.e. direct population via neutron knockout, or feeding from a higher energy state), the alignment of the state may vary based upon the relative strengths of each channel. In this case, the overall statistical tensor required, is simply the weighted sum of statistical tensors of each population process.

The γ-ray angular distribution function $W(\theta)$, specifies the intensity of a γ-ray transition, measured at an angle θ with respect to the beam axis. The angular distribution function of a transition is calculated using the statistical tensor of the initial state. If the state has axial symmetry about the quantisation axis (z-axis) then the angular distribution can be expressed as

$$W(\theta) = \sum_{k} B_k(I_i) A_k(\delta_\gamma l l' I_f I_i) P_k(\cos(\theta)) \,. \tag{3.8}$$

This can be written in terms of the m-substate populations $P(m)$ by substituting the formula for the statistical tensor B_k, in equation 3.7.

$$W(\theta) = \sqrt{2I+1} \sum_{k,m} (-1)^{I+m} \langle I - m I m | k 0 \rangle P(m) A_k(\delta_\gamma L L' I_f I_i) P_k(\cos\theta) \tag{3.9}$$

Where I is the initial state spin of the γ-ray transition, l and $l' = l+1$ are the lowest possible multipolarities of the γ ray. The $P_k(\cos\theta)$ terms are the Legendre polynomials, where only the even ordered terms contribute to the angular distributions. The A_k terms are related to the dynamic angular momentum coupling of the initial and final spins of the transition, with a term to account for transitions with mixed multipolarities [89].

The γ-ray angular distribution formula, given by equation 3.9, specifies the intrinsic angular distribution of the transition in the centre-of-mass frame. Therefore, to enable comparison to the experimental data in the lab frame, a series of corrections needed to be applied in order to account for Lorentz boost of the fast moving fragments, in addition to other detection efficiency terms. The following subsection outlines the measurement of the angular distributions of the γ-ray transitions and details each of the corrections that were required.

γ-ray Angular Distribution Data

The nucleon knockout reactions that take place in the secondary target induce a momentum change in the outgoing fragments. The momentum distribution of the outgoing fragments provides some insight into the nucleon that was knocked out, as the angular momentum of the knocked-out nucleon alters the width of the fragment momentum distribution. In the reaction being studied in this analysis, it is highly likely that the excited states in ^{23}F were populated via the removal of a neutron from the $1d_{5/2}$ shell. The removal of the neutron from the $2s_{1/2}$ would instead populate ground state ^{23}F, and the removal of a

neutron from the lower shells is unlikely as they are more deeply bound.

The S800 is able to a extract a measure of the momentum distribution of the outgoing fragments. The D_{TA} displayed in figure 3.20, is the relative difference of the measured magnetic rigidity ($B\rho$) from the central rigidity. The distribution is not symmetric about the zero, as the S800 was not centred for the ^{23}F fragments, but rather for ^{21}O. The structure to the right of the distribution is the unreacted ^{24}F beam, that can be seen to be leaking into the PID gate in the inset. The comparison of the widths of these two structures, reveals the effect of the reaction on the momentum distribution of the fragments. Before proceeding with the γ-ray angular distribution analysis, a cut was applied from the centre of the fragment momentum distribution to the high-energy region, denoted by the dotted black lines. This was to ensure the removal of any asymmetries in the low-energy region of the momentum distribution, which have been associated with higher-order dissipative effects in the nucleon knockout reactions at NSCL, as discussed in a number of reports [91, 92, 93, 94, 95].

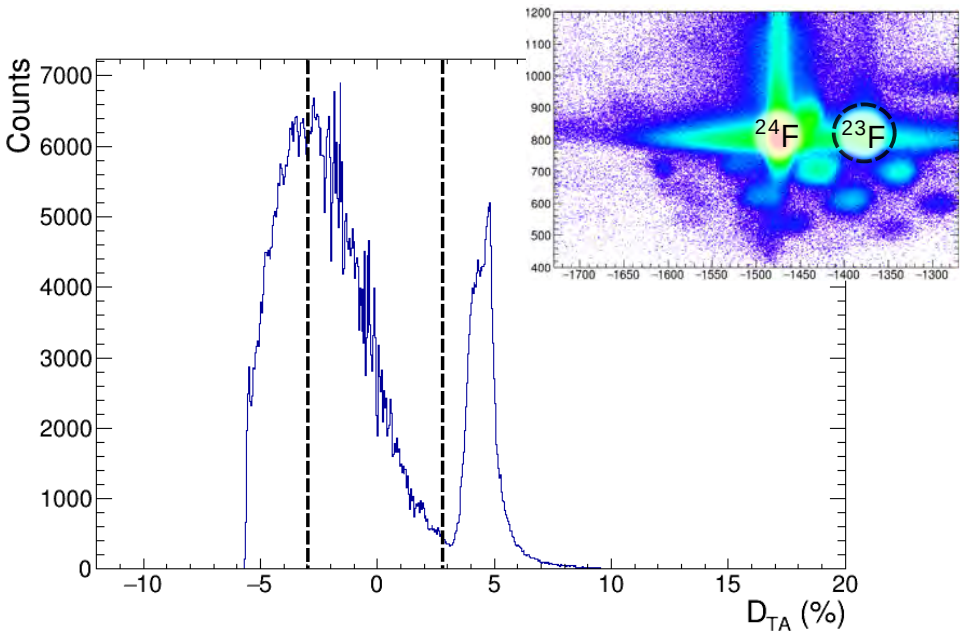

Figure 3.20: Plot of the D_{TA} from the S800, gated on the ^{23}F. The inset shows the ^{24}F leaking into the ^{23}F gate in the outgoing fragment PID. The momentum distribution cut is denoted by the black dotted lines.

The distributions of γ-ray emission angles were obtained by dividing the total angular detection range into intervals of 10 degrees in the laboratory frame, see figure 3.21. This interval was selected to allow enough statistics for the spectra to be fit with high level of confidence, whilst also maintaining enough data points for the shape of the distribution to be visible. The intensity of a transition across each angular interval constitutes the angular distribution of that transition. However, in order to effectively compare these intensities

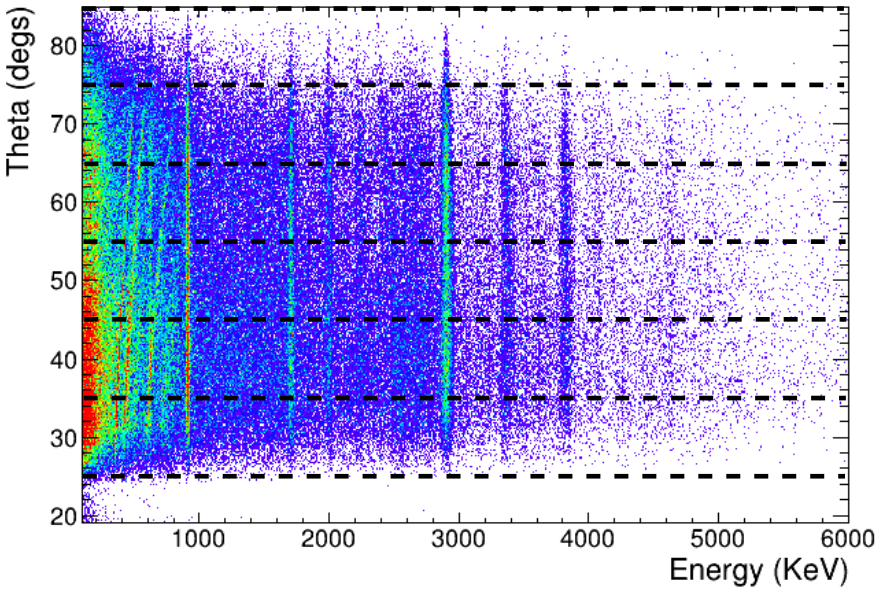

Figure 3.21: Illustration of the division of the full angular detection range into the regions used for the γ-ray angular distributions analysis.

and extract the angular distributions, it was of paramount importance that the detection efficiencies at each angle were dealt with correctly. There were a number of factors which affected the efficiency of the γ-ray detection, at the different angles. This resulted in the deviation of the detected γ-ray angular distributions W_{Det}, from the intrinsic angular distributions of a transition W_{Intr}, such that

$$W_{\mathrm{Det}}(\theta) = W_{\mathrm{Intr}}(\theta_{\mathrm{c.m}}) \cdot \varepsilon_{\mathrm{Det}}(\theta) \cdot \varepsilon_{\mathrm{Geo}}(\theta) \cdot \frac{1-\beta^2}{(\beta\cos(\theta)-1)^2}\,. \tag{3.10}$$

To recover the intrinsic angular distributions, from which the multipolarities of the transitions could be derived, these efficiency terms needed to be accounted for. The first correction term in equation 3.10 is the detection efficiency of the γ ray. The angular dependence of this term originates in the Doppler shift of the γ-ray energies, in the laboratory frame. As has already been discussed in section 2.3.1, γ rays detected at different angles will be observed to have different lab-frame energies, therefore different detection efficiencies. Consequently, for the same transition, γ rays detected at the forward angles, would have a reduced detection efficiency compared to the back angles. The second efficiency factor in equation 3.10, is the geometrical coverage of the detectors. This a measure of how many detectors were present in each of the angular intervals. Clearly, a greater number of detectors in an angular interval would result in a higher detection efficiency. The final correction term is the Lorentz boost, which arises due to the relativistic velocity of the beam

fragments. This term results in the γ-ray angular distributions being skewed towards the forward angles. Each of these terms were accurately accounted for, via the analysis of the detailed Monte Carlo simulations, see section 3.2.9.

3.2.7 GEANT4 Simulations

Detailed Monte Carlo GEANT4 simulations [96] of the experimental setup were carried out, in order extract the relative intensities of the transitions, branching ratios, level populations and γ-ray angular distributions. The simulation and fitting of γ-ray spectra to measured data is a power analysis tool, enabling the complete evaluation of all components on the γ-ray spectrum. This is particularly useful when measuring the intensities of transitions with a complex background function, such as peaks found on the Compton edge of another nearby transition, or overlapping with a neutron-induced background peak. The simulations also provide a means to identify and interpret any subtle abnormalities in the peak structures, arising due to lifetime effects, or multiple peak overlaps, that may have been missed upon first inspection of the γ-ray spectrum.

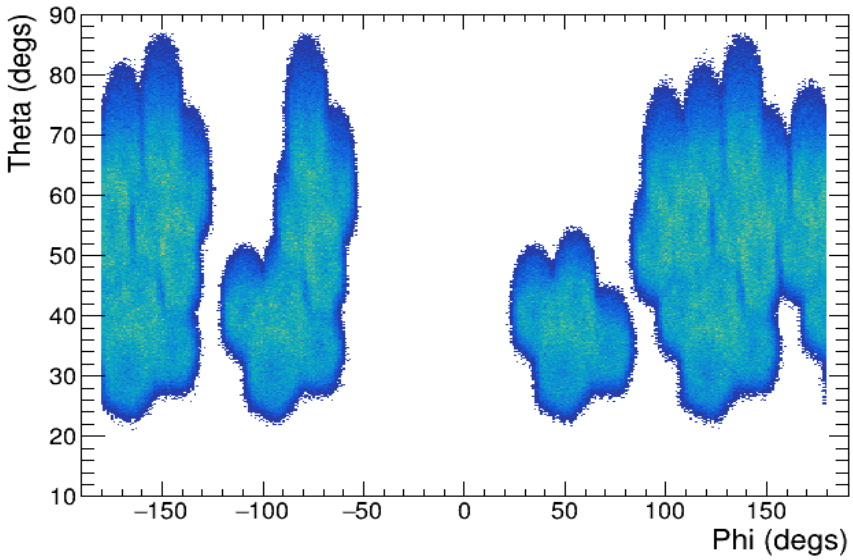

Figure 3.22: The simulated GRETINA geometry in the same configuration as the experiment.

The simulations were carried out using a modified version of the G4Lifetime simulation, in GEANT4, which is a tool originally devised to assist with the analysis of Recoil Distance Lifetime Measurements at NSCL [97]. As such, it has the GRETINA geometry implemented as it was at NSCL during the experiment, see figure 3.22, as well as the beampipe and shielding. The target material, density and position were inputted into the simulations, in addi-

tion to the incoming-beam properties and reaction details. The γ-ray transition energies measured in section 3.2.4 were also implemented.

The simulation runs event-by-event, with each event starting with the generation of the primary beam particle, and ending once all primary and secondary particle tracks have ended. The simulation contains the physics processes governing particle and electromagnetic interactions, and as such accurately describes the passage of particles through matter. They are particularly adept at dealing with the Doppler effect and the corrections of γ rays emitted from a fast beam, travelling through a degrader or backing, and replicating the lineshape on the spectrum due to any lifetime effects. However, the simulations did not include the tracking functionality of GRETINA, and therefore had to be compared to the single-crystal γ-ray spectra, without add-back, reducing the peak-to-totals. The simulated output files were processed in the same way as the data files, so as to allow the comparison and fitting of the spectra.

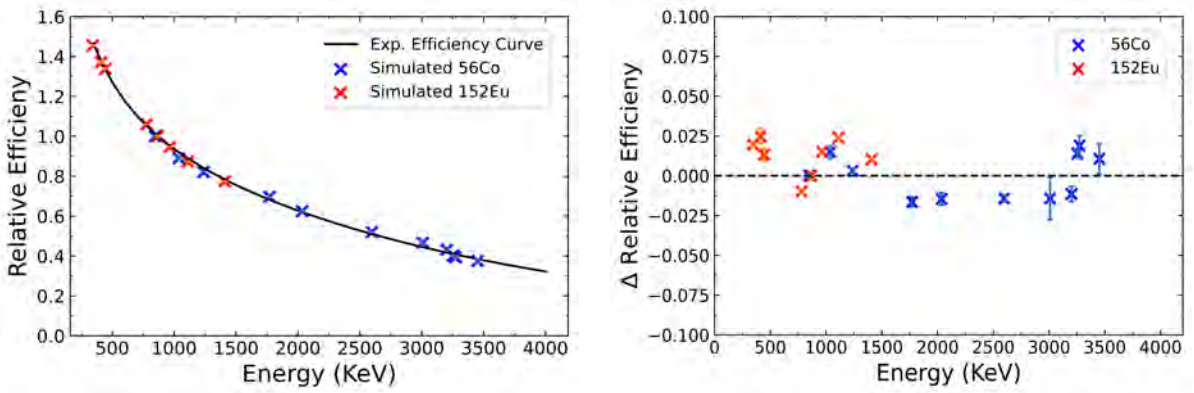

Figure 3.23: The plot on the left shows the simulated γ-ray detection efficiencies from simulated ^{56}Co and ^{152}Eu sources. The data is plotted alongside the experimental single-crystal efficiency curve from figure 3.14, to demonstrate the good replication of the GRETINA efficiencies in the simulation. The plot on the right is the difference in the simulated efficiency from the experimental efficiency.

In order to accurately fit the simulated spectra to the measured data, and extract the transition intensities, branching ratios and level populations, the γ-ray detection efficiency and energy resolution of GRETINA must be properly simulated. To verify that the detection efficiency was correctly implemented, the ^{56}Co and ^{152}Eu source peaks were simulated, with the relative intensities obtained from [86]. The simulated relative efficiency data, again normalised to the 846.7 keV transition, was compared to the experimental single-crystal efficiency curve with good agreement, see figure 3.23.

The detector energy resolution was simulated by assigning the exact γ-ray energy calcu-

lated by the simulation, to be the mean μ of the Gaussian probability distribution, given by equation 3.11. The γ-ray energy value taken by the simulation was then obtained through the random sampling of this Gaussian distribution.

$$f(E) = \frac{1}{\sigma\sqrt{2\pi}} e^{-\frac{1}{2}\left(\frac{E-\mu}{\sigma}\right)^2} \tag{3.11}$$

The standard deviation of the distribution σ, was again determined via the measurement of the calibration source data. The Full Width Half Maxima (FWHM) of the peaks from the ^{56}Co and ^{152}Eu sources were measured and plotted against the transition energies, see figure 3.24. A linear fit was then carried out to this data, in order to determine the FWHM as a function of the γ-ray energy, with the form

$$\text{FWHM}(E) = a_1 \times E[\text{keV}] + a_2\,. \tag{3.12}$$

From the fit in figure 3.24, the coefficients were calculated to be $a_1 = 0.8256 \times 10^{-4}$ and a_2 = 2.025 keV. This function was then applied to the Gaussian distribution for the simulated detector energy resolution, where $\sigma = 0.425 \times \text{FWHM}(E)$. The result of this was a realistic, energy dependent, simulated detector resolution.

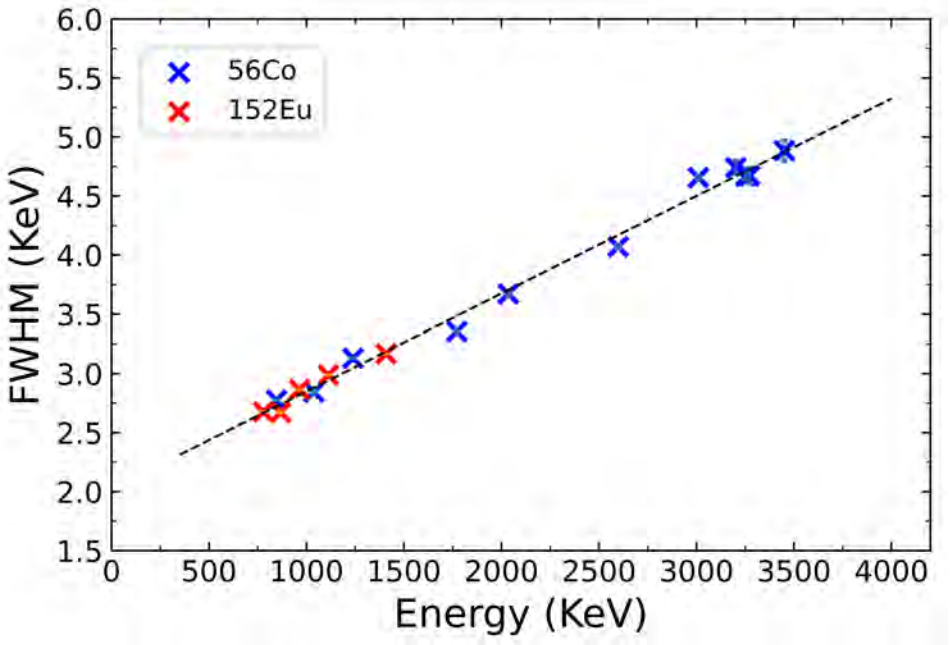

Figure 3.24: The FWHM of the peaks from the ^{56}Co and ^{152}Eu sources, plotted against the γ-ray energy. The linear fit function is given by equation 3.12, and was used to tune the simulated GRETINA energy resolution.

3.2.8 Simulation Spectra Fit

The fitting process was carried out in a similar way to the Gaussians in section 3.2.4, only this time with a greater number of free parameters to be fit. First, the background peaks were simulated, representing the decays originating from the neutron inelastic scattering on aluminium and germanium, figure 3.25. These were then Doppler corrected to form the broad background structures that can be seen on the spectrum.

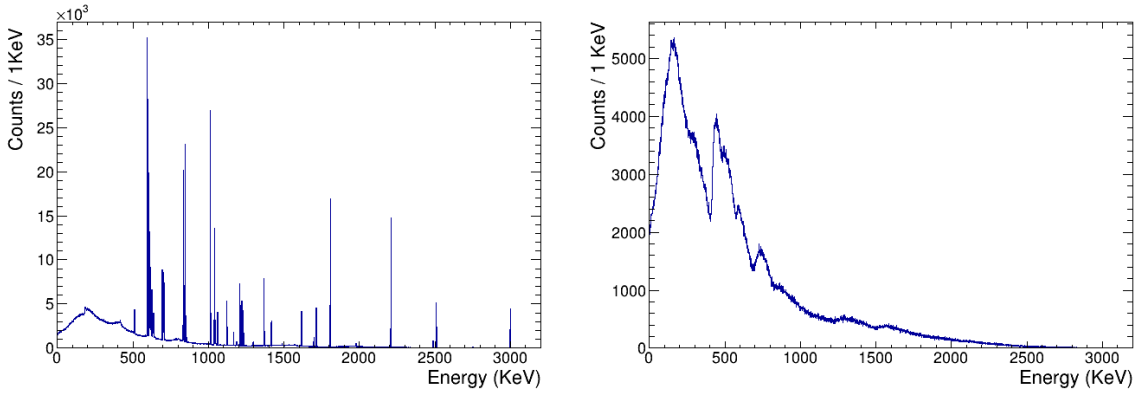

Figure 3.25: The plot on the left shows a γ-ray spectrum of the simulated neutron inelastic scattering peaks of aluminium and germanium. The right plot displays this spectrum after the Doppler correction has taken place, with respect to the same direction and velocity as the ^{23}F fragments.

These background structures were then fitted to the experimental spectrum, along with a double exponential curve, and the individual cascades and transitions, where the fitting parameter was a coefficient representing the intensity of each transition, equation 3.13. A Doppler shifted 511 keV term was also present in the fit. This term was required, as many of the γ rays in the background were not simulated, instead substituted for by the double-exponential curve. This meant far fewer pair production and annihilation events took place, resulting in the smeared out structure around 460 keV, which is the Doppler corrected 511 keV peak, not being fully filled in. Without the introduction of this term, the low-energy region of the spectrum can not correctly be accurately reproduced.

$$f(x,\mathbf{a}) = a_1 e^{-a_2 x} + a_3 e^{-a_4 x} + a_5 h_{BG}(x) + a_6 h_{511}(x) + a_7 h_1(x) + a_8 h_2(x) + ... \tag{3.13}$$

Where $\mathbf{a} = (a_1, a_2, a_3, ...)$ again represents a vector of free fitting parameters, h_{BG} and h_{511} are the Doppler corrected background peaks and 511 keV spectra respectively, and $h_1(x), h_2(x), ...$ are the spectra of the individual cascades and transitions. The free parameters $(a_7, a_8, ...)$

represent the intensities of their corresponding transitions. The functions representing the cascades here are a full spectrum, taking not only the peak intensities into account, but also the intensities of the escape peaks, Compton structures and the 511 keV peak, and their impact on the total spectrum and other nearby peaks. All of these components are combined into the fit, so that there can only be a single solution to correctly replicate the experimental spectrum, see figure 3.26. Therefore, this method provides a uniquely holistic understanding of the spectrum, as all aspects of the spectrum are simulated and accounted for and anything missing from the fit is noticeable by its absence. The fit replicated the shape of the spectrum and provided valuable insight for the determination of the intensities and branching ratios of the transitions, as well as the relative populations of the levels in ^{23}F.

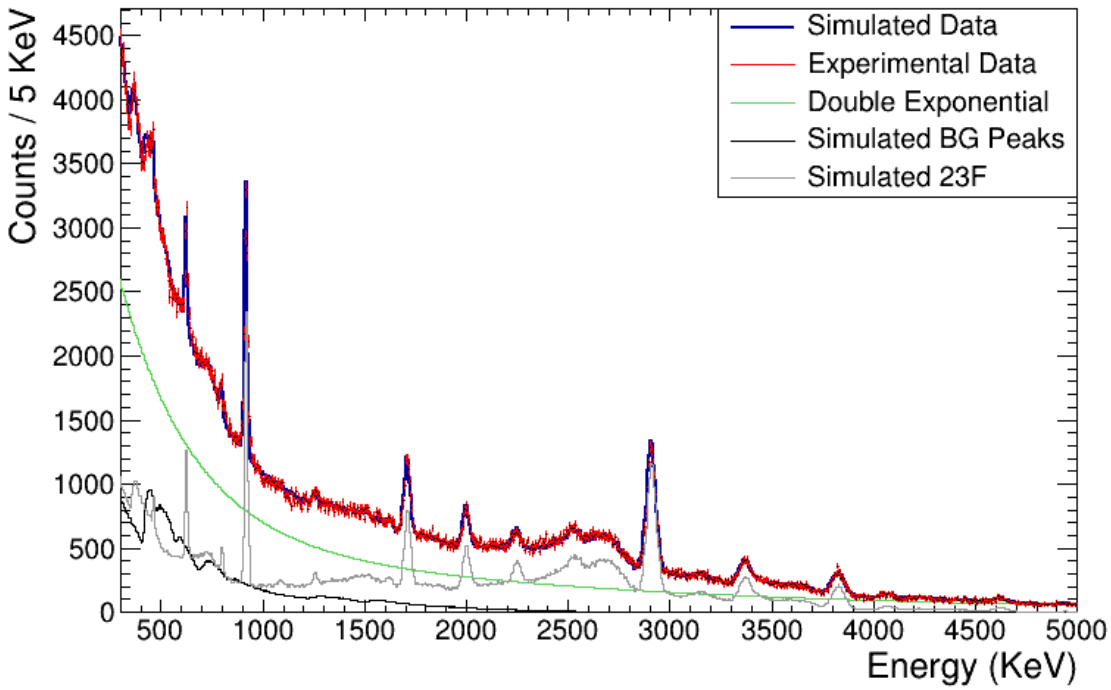

Figure 3.26: Plot of the simulated data fit to the experimental single-crystal γ-ray spectrum. The experimental data is in red and the total simulated fit in blue. The components of the fit, the double exponential curve, the neutron-induced reaction peaks, and the ^{23}F γ rays are denoted by the black, green and grey lines respectively.

3.2.9 Simulation Angular Distribution Analysis

The simulations that were used to fit the full angle spectrum were also cut into the angular slices defined in figure 3.21. These simulated transitions had an intrinsically-isotropic angular distribution, where any differences between the measured intensities of the transition at the different angles, were due to the efficiency terms described by equation 3.10. As the Lorentz boost is included in the simulations, and the GRETINA geometry and detection efficiencies have been correctly implemented, figures 3.22 and 3.23 respectively, the total efficiency factors relevant to the γ-ray angular distributions, were well reproduced by the simulations. Therefore, by fitting the simulated to the experimental spectra, these efficiencies have effectively been corrected for. Thus, the fitting parameters of the simulated transitions once again provided a measure of the intensities of the transitions, enabling the extraction of the γ-ray angular distributions.

The fitting of the γ-ray spectra across the angles, figure 3.27, was carried out using the same procedure as for the full angle spectrum. As before, this process enabled the complete description of the spectra, including the background peaks, Compton structures and the escape peaks. Rather than form the smooth background structures as in the full angle fit, the neutron inelastic scattering peaks, denoted by the black lines on figure 3.27, form block shapes. This is a result of the angular cutting of the Doppler corrected peaks, where the γ-ray energy is correlated with the detection angle. The results of the fitting and the γ-ray angular distributions for each of the transition are displayed and discussed in section 3.3.3.

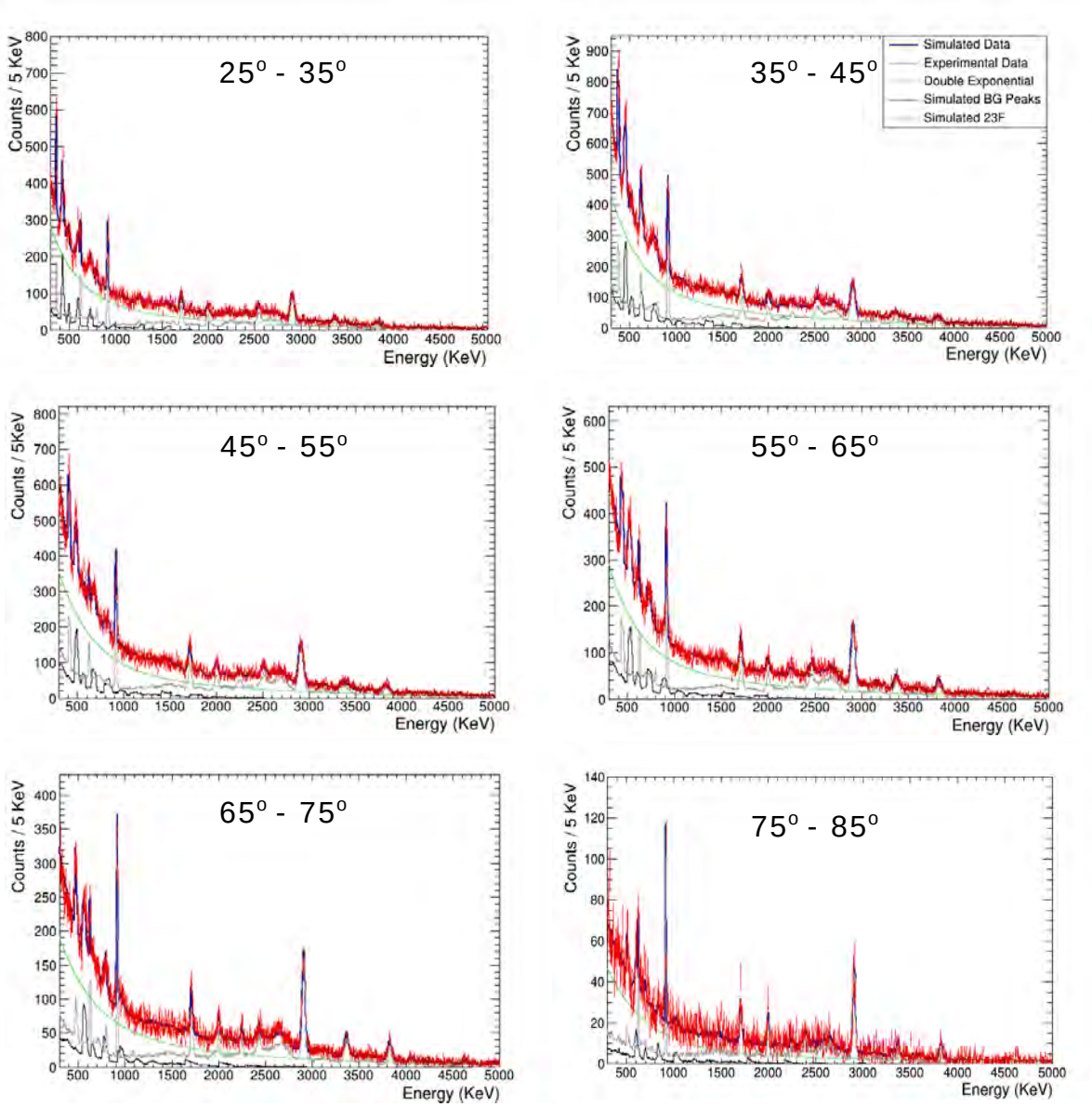

Figure 3.27: The fitting of the simulated data to the experimental single-crystal γ-ray spectra, across each angular interval. The parameters of the fit are the same as for the full angle case, where the components are again denoted by the coloured lines. The intensities of each transition, in each interval, can be extracted from the fit to calculate the γ-ray angular distributions.

3.3 Results

The following sections present the results of the analysis detailed above. Section 3.3.1 covers the results from the analysis of the Doppler corrected γ-ray spectrum, obtained through the fitting of Gaussians and simulations to the data. The results of the γ-γ coincidence analysis are displayed in section 3.3.2, as well as the identification of the cascades and the constriction of a new ^{23}F level scheme. The γ-ray angular distribution results are then presented in section 3.3.3, alongside the spin assignments of the excited states. The results are summarised with the complete level scheme in section 3.3.4.

3.3.1 γ-ray Spectroscopy Results

The combined analysis of the Doppler corrected γ-ray spectrum, through the fitting of both the Gaussians and the simulations, enabled a complete description of the spectrum. The fitting of the Gaussians on a linear background, outlined in section 3.2.4, was used for the identification and energy measurements of the γ-ray transitions, on the tracked spectrum. From this analysis, several new transitions were observed for the first time, in addition to many transitions that have previously only been observed in other reaction channels, i.e proton transfer reactions. The populations of these states and transitions is further elaborated upon in section 3.4.

Through the fitting of the simulations to the experimental single-crystal spectrum, the strengths of the transitions relative to the 2909 keV γ ray, were extracted with an accurate accounting of the background components. Additionally, the lack of any apparent lifetime induced lineshapes on the spectrum, confirmed by the simulation fit, also indicates that there were no measurable lifetime effects for these transitions. Table 3.1 summarises the measured γ-ray energies and their relative intensities. The new transitions are highlighted in bold and those observed for the first time in the neutron removal reactions, by the asterisks. All of the transitions listed in this table have been fitted by Gaussians, with a confidence level of greater than 5σ.

E_γ (keV)	Int. $_{\text{Rel.}}$ (%)	E_γ (keV)	Int. $_{\text{Rel.}}$ (%)
459.2 (11)	1.3 (3)	1999.8 (5)	15.8 (6)
625.4 (2)	7.6 (3)	2241.3 (13)*	10.7 (6)
798.9 (12)	2.4 (3)	2909.0 (7)	100
917.2 (1)	30.3 (5)	3368.4 (9)	22.6 (7)
1084.1 (15)	0.8 (3)	3825.8 (7)	29.3 (7)
1256.0 (18)*	1.9 (4)	4064.8 (27)*	5.4 (6)
1620.7 (21)	2.0 (4)	**4623.7 (24)**	7.1 (5)
1707.2 (30)	19.5 (8)	**4943.7 (38)**	2.2 (4)
1722.9 (38)	4.9 (8)		

Table 3.1: The γ-ray energy and relative intensity measurements obtained from the Doppler corrected γ-ray spectrum. The new transitions are highlighted in bold and those observed for the first time in the neutron removal reactions, by the asterisks. All values displayed in this table are from the present analysis.

3.3.2 γ - γ Coincidence Results

The γ-γ coincidence analysis was carried out to observe which of the γ rays exist in a cascade, so that a new level scheme for ^{23}F could be constructed. In general, when a γ ray that is part of a cascade is detected, the other other γ rays will also be detected in coincidence. Therefore, by gating on the transitions measured above, the γ rays observed in coincidence should appear on the subtracted coincidence spectra. These spectra for the data are presented in figures 3.28 and 3.29, with the coincidences summarised in table 3.2. Only the gatings which have measurable coincidences, to a confidence level of approximately 3σ or greater, are displayed. Due to the low γ-γ efficiency, from the detector coverage, this includes only the comparatively strongest of the γ-ray transitions.

Through the studying of the γ-ray coincidence data, the cascades in ^{23}F were deduced. As can be seen from figures 3.28 and 3.29, or from the coincidence table 3.2, the 2909 keV is coincident with five other γ rays. As such, it constitutes the final transition to the ground state in a number of different cascades. The dominant transition feeding into this state is the 917 keV γ ray, which itself is in coincidence with the 1707 keV transition. The 2909 keV and 917 keV transitions sum up to the 3826 keV state, the decay from which to the ground state is also observed to be in coincidence with the 1707 keV transition. Therefore, from this simple analysis, the 2909 keV, 3826 keV and 5534 keV states were deduced. The 2909 keV is

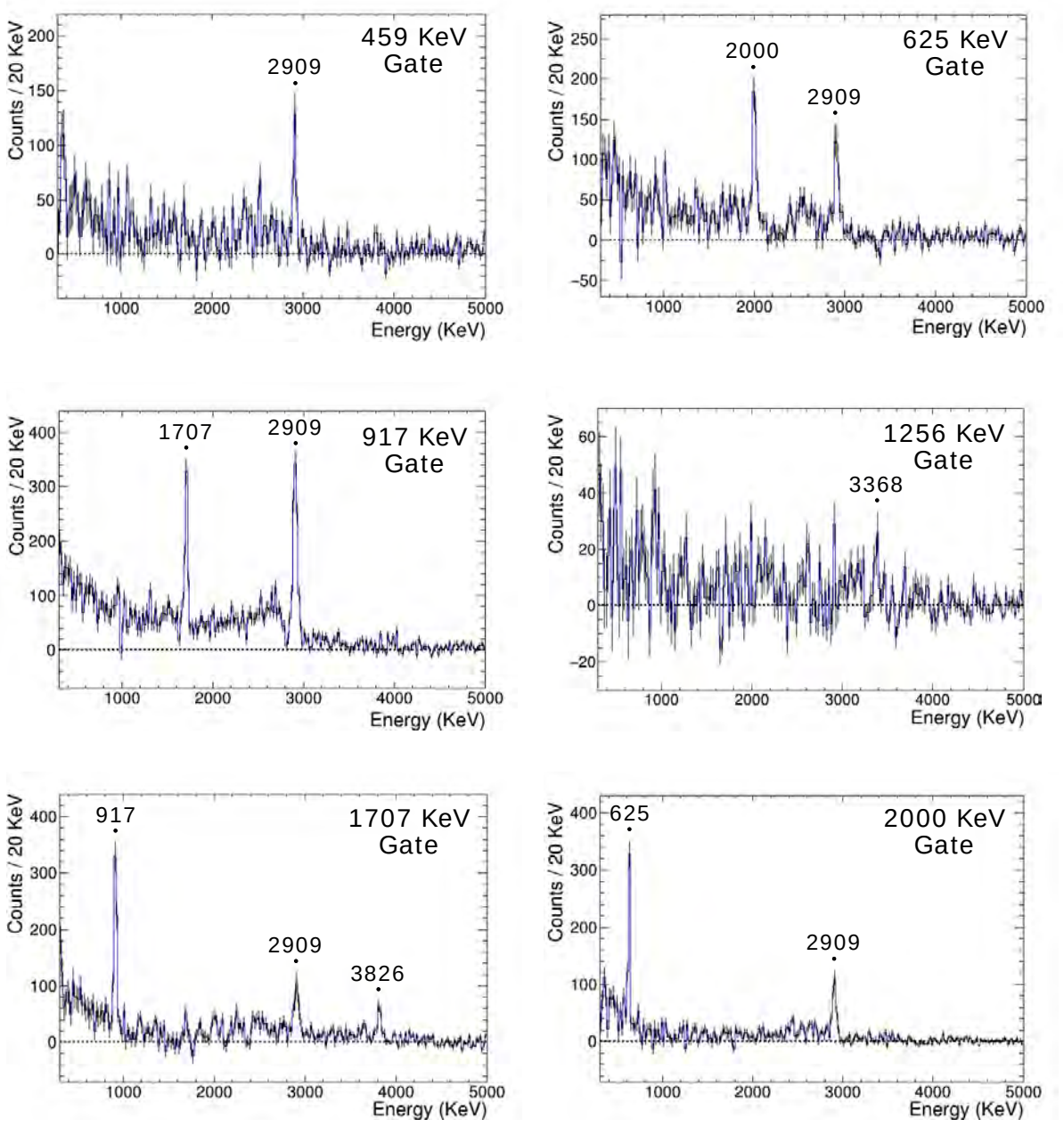

Figure 3.28: The first set of subtracted γ-ray coincidence spectra for the lower energy transitions. The γ rays in coincidence with the specified gatings are labelled on the spectra.

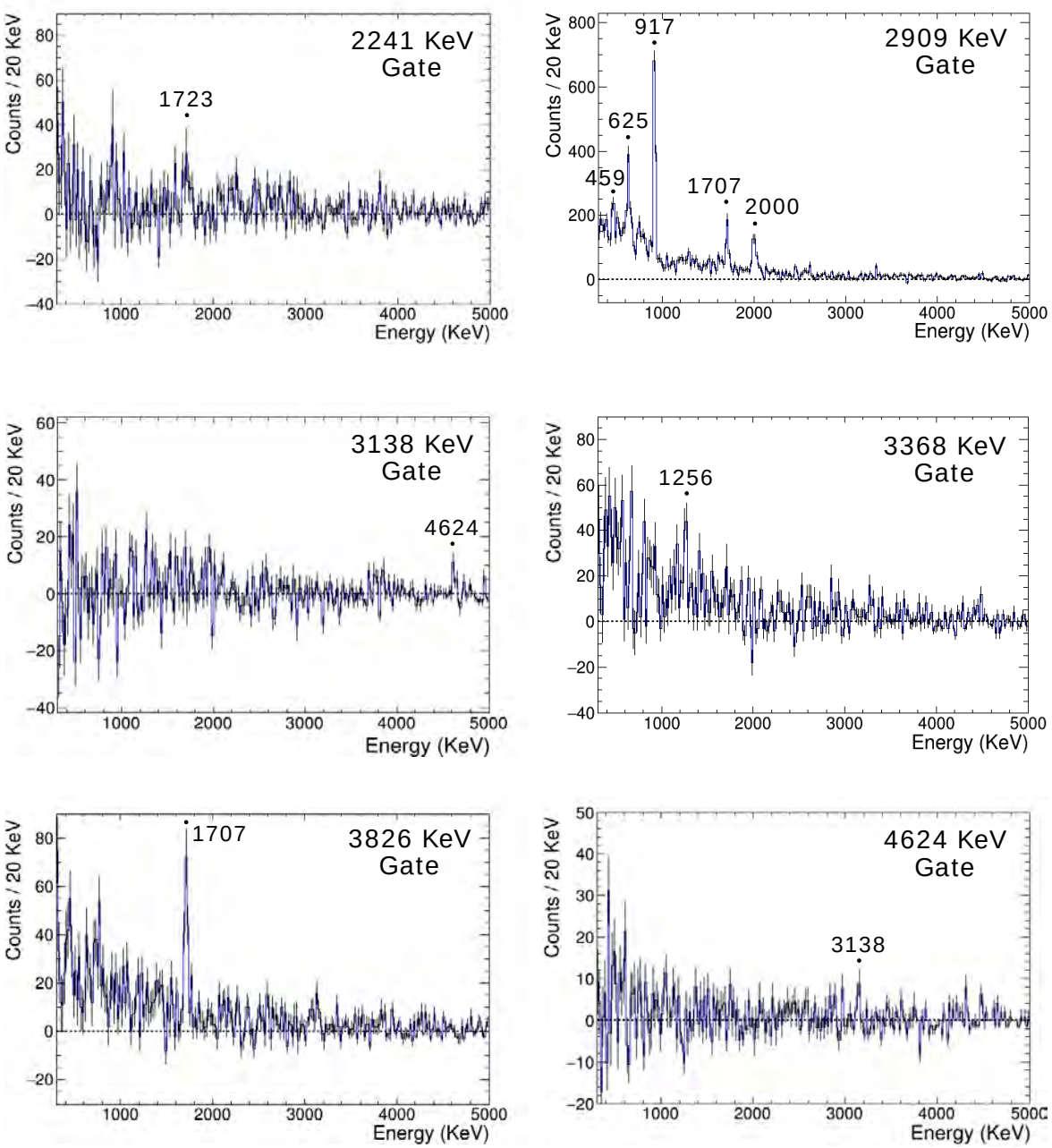

Figure 3.29: The second set of subtracted γ-ray coincidence spectra for the higher energy transitions. The γ rays in coincidence with the specified gatings are labelled on the spectra.

E_γ (keV)	Coinc. E_γ (keV)	E_γ (keV)	Coinc. E_γ (keV)
459	2909	2241*	1723
625	2000	2909	**459**
	2909		625
917	1707		917
	2909		1707
1256*	3368		2000
1707	917	**3138**	**4624**
	2909	3368	1256*
	3826	3826	1707
2000	625	**4624**	**3138**†
	2909		

Table 3.2: A summary of the γ rays observed in coincidence with the gatings displayed in figures 3.28 and 3.29. With the coincidence data, the γ-ray cascades were identified and the new level scheme was constructed. The new transitions are again highlighted in bold, with the asterisks identifying those observed for the first time in the one-neutron removal reactions. The † symbol indicates that the transition was fit with a confidence level of less than 3σ.

also coincident with the 2000 keV transition from the 4909 keV state, which again is fed from the 5534 keV level by the 625 keV γ ray. These four states and the transitions between them, make up the most dominant cascades that were observed in the data.

The newly measured 459 keV γ ray was also observed to be in coincidence with the 2909 keV transition, from the 3368 keV state. The transition from this state to the ground state, was also observed on the γ-ray spectrum. In the 459 keV coincidence spectrum, only the 2909 keV γ ray is present. This is in contrast with the 3368 keV gating, where the 1256 keV transition from the 4624 keV state can be clearly discerned. However, this is due to the fact that the 459 keV transition is significantly weaker than the 3368 keV. Therefore, the 1256 keV γ ray is not expected to be observed in the 459 keV gating.

Gating on the direct decay of the 4624 keV state, a weak transition, unseen on the Doppler corrected γ-ray spectrum, was observed. This transition was measured to have an energy of 3138.1 (41) keV, and was fit with a confidence level of 2.8σ. Despite the low confidence level

of the fit, by gating on the 3138 keV region, the 4624 keV transition was visible and could be fitted to a confidence level of greater than 3σ. The fact that this transition was not observed on the γ-ray spectrum could be indicative of its low intensity. The apparent low intensity of the γ ray, together with its location on the Doppler corrected spectrum, between the strong 2909 keV and 3368 keV transitions, is most likely the reason why this transition was not previously observed. The low intensity also hampers the observation of this transition in the 1256 keV gate. However, there does appear to be a structure, discernible in the 1256 keV region of the 3138 keV gate, but it was not able to be fitted with a sufficient confidence level. With this analysis, the 7762 keV state was tentatively assigned. The result of this analysis, was the inclusion of the 3368 keV, 4624 keV and 7762 keV states to the ^{23}F level scheme, in figure 3.31.

The final gating not yet discussed, is that of the 2241 keV γ ray. In this gating, the 1723 keV transition was fitted with a confidence level of 4σ. In addition, there appears to be a structure around the 900 keV region, however this could not be fitted with sufficient confidence. The potential for additional transitions indirectly populating this state, via feeding, is relevant to the discussion of the populations of the single-particle proton states, see section 3.4.4. The 1723 keV region, does not have a gate displayed in figure 3.28, due to the dominant 1707 keV transition nearby, the coincidences of which are amongst the strongest transitions on the spectrum. Therefore, the 2241 keV state was assigned to be in coincidence with only the 1723 keV γ ray, from the 3964 keV excited state.

The remaining transitions had no discernible γ rays detected in coincidence. Therefore, the 4065 keV transition was assigned to be a direct ground state decay of an excited state not within a cascade. Additionally, due the proximities in their energies, the 4944 keV transition could be the direct ground state transition from the 4909 keV state. However, this could not be confirmed by the γ-γ coincidence analysis, as the 625 keV transition could not be identified in the gating of the 4944 keV region. This was to be expected though, as a consequence of the low intensity of the detected 4944 keV γ ray.

The apparent 35 keV energy gap between the 4944 keV transition and the 4909 keV state, deduced from the 2909 keV - 2000 keV cascade, could not be simply explained by the uncertainties in the measurements. The possibility of a lifetime effect causing this mismatch was investigated through the use of the simulations. It was found that any lifetimes large enough to cause an effect on this magnitude would induce measurable asymmetric lineshapes onto the peaks, which was not observed in the γ-ray spectrum. An alternative possibility was that this energy gap was caused by an uncertainty in the calibration, due to the highest energy calibration point being only 3.2 MeV. However just 300 keV away, the 4624 keV transition was measured to be in strong agreement with the energies of 3368 keV - 1256

keV cascade, to less than 1 keV. Therefore, as these two energies could not be reconciled by either lifetime nor calibration effects, and could not be explained by the uncertainties in the measurements, the 4909 keV and 4944 keV were assigned to be distinct excited states.

The other new transitions that were measured on the spectrum 798.9 (12) keV, 1084.1 (15) keV and 1620.7 (21) keV also could not be assigned a place in the level scheme, due to them not appearing in the coincidence gatings. It should be noted however, that the 799 keV γ ray does indeed fit in the level scheme, decaying from the 4624 keV to the 3826 keV state. As does the 1084 keV γ ray, which could be located between 3826 keV and 4909 keV excited states. However, as these γ rays were not observed to be in coincidence with any other transitions, they could not be placed in the level scheme, regardless of how well they fit numerically. The new level scheme, in addition to a summary table of the states and transitions, are presented in section 3.3.4.

3.3.3 γ-ray Angular Distribution Results

The γ-ray angular distributions were measured by dividing the angular detection range into six regions and then fitting the simulations to the resulting spectra. From the parameters of the fit, the intensities of the transitions in each angular interval were extracted. As a consequence of the division into the smaller angular ranges, only the distributions of the strongest transitions could be extracted. In the case of the weaker transitions, the errors in the intensity measurements were often greater than the fluctuations in the distributions. The distributions were normalised across the detection range and the angles were converted from the laboratory frame θ, to the centre-of-mass frame $\theta_{\text{c.m.}}$ by equation 3.14, so they could be compared to the calculations.

$$\cos(\theta_{\text{c.m}}) = \frac{\cos(\theta) - \beta}{1 - \beta\cos(\theta)} \tag{3.14}$$

The m-substate populations of the excited states in ^{23}F, after the neutron removal reactions of a 95 AMeV ^{24}F beam on a ^{9}Be target, were calculated by Jeff Tostevin from the nuclear theory group in the University of Surrey. The population calculations assumed a ^{24}F ground state of 3^{+}, which was inferred by the longitudinal momentum distribution measurements in Sauvan [98]. In the neutron knockout reactions, the production of the ^{23}F was dominated by the removal of the $s_{1/2}$ and $d_{5/2}$ neutrons. However, since the removal of an $s_{1/2}$ neutron directly populates the ground state of ^{23}F, only the $d_{5/2}$ removals were considered for the calculations.

As a result of the angular momentum coupling of $^{24}\mathrm{F}(3^+) \otimes \nu\mathrm{d}_{5/2}$, the neutron knockout reactions of ^{24}F could populate excited states ranging from $1/2^+$ to $11/2^+$ in ^{23}F. Therefore, the γ-ray angular distributions were calculated for a range of M1 and E2 transitions, between these spins, using the m-substate populations and assuming direct population to the excited states. The calculated distributions, in the centre-of-mass frame, were fitted to the experimental distributions with two free parameters, equation 3.15, to adjust for the different normalisations and to mitigate for the assumptions of total direct populations and pure multipolarities.

$$\alpha W(\theta_{\mathrm{c.m.}}) + \nu \tag{3.15}$$

The γ-ray angular distribution analysis entailed the fitting of the calculated distributions, with all possible combinations of initial and final spins between the limits of 1/2 and 11/2, to each of the experimental distributions. In each case a χ^2 value was extracted to quantify the goodness-of-fit. It was apparent that each experimental distribution could have more than one calculated transitions that statistically fit well. However, by using the γ-ray coincidences in table 3.2 to deduce the cascades, the combination of transitions could be reduced to a single unique solution, which had the best fits and fit together into the new level scheme, see figure 3.31. These best fits are displayed in figure 3.30.

The fitting of the γ-ray angular distributions enabled the assignment of spins to the states, from which the transitions decay. The top six plots in figure 3.30 present the γ-ray angular distributions of the transitions in the strong cascades originating from the 5534 keV state. The level of anisotropy in the distribution of a transition is due to a mixture of the intrinsic alignment of the state, the m-substate populations caused by the reaction, and the amount of direct population and feeding. Starting with a ground state of $5/2^+$, which was determined by the fragment longitudinal momentum distributions in [98], the only distribution that could be fitted for the 2909 keV γ ray was the 7/2 to 5/2. As the 2909 keV transition lies at the bottom of several cascades, the shape of the distribution can be seen to be reduced due to the large amount of feeding. Similarly, the 917 keV transition which feeds to the 2909 keV level, had to have a final spin of 7/2. The only distribution where this could be the case, which fitted the experimental distribution, was from an initial spin of 9/2. This assignment was reinforced by the fitting of the 9/2 to 5/2 distribution to the 3826 keV transition. This process was applied to the rest of the transitions in these cascades, so that the spins of the states could be determined. The initial and final spin of each transition is summarised in table 3.3, along with the fitting parameters and the χ^2 of each fit. The assigned spins are labelled on the complete level scheme in figure 3.31.

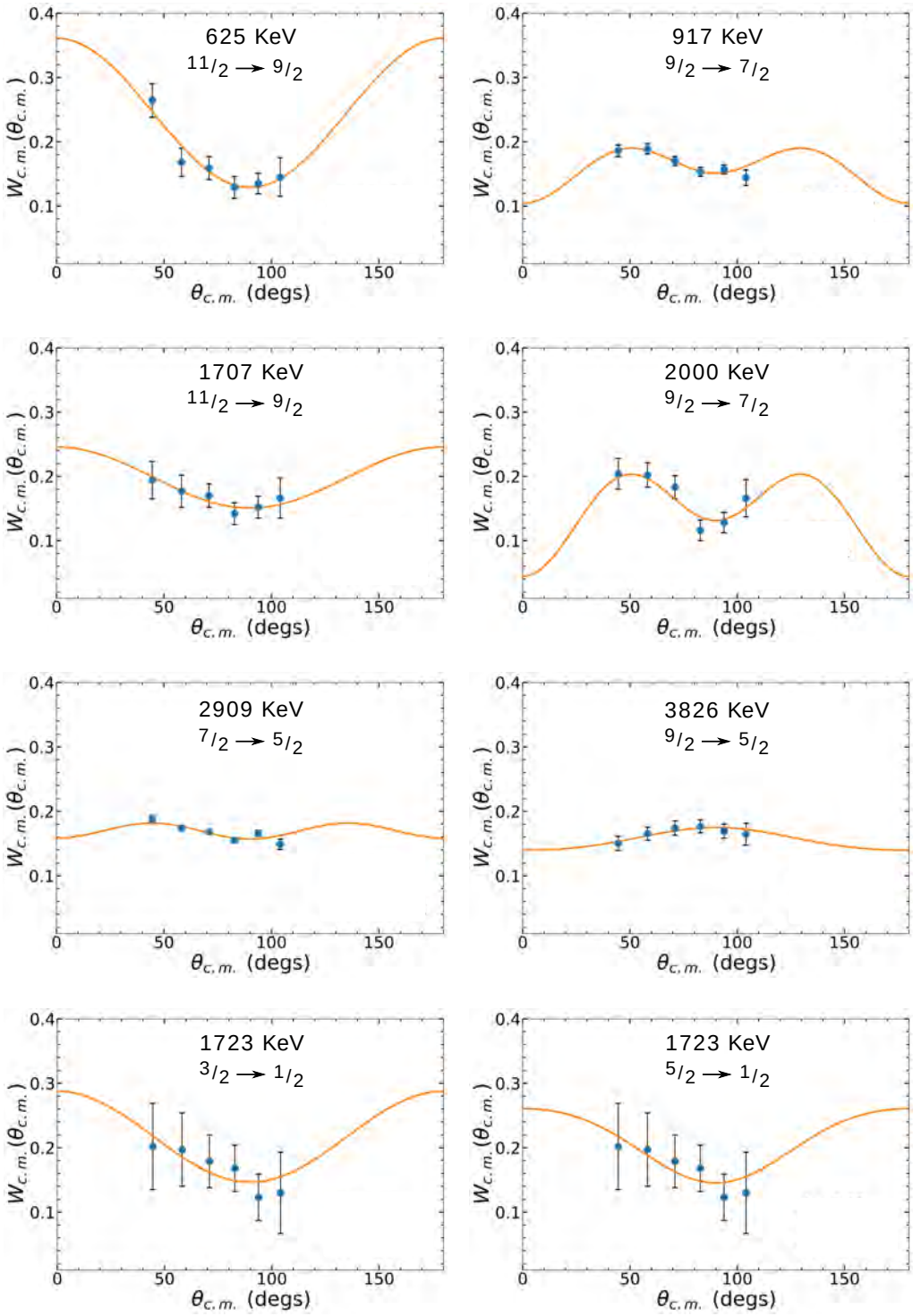

Figure 3.30: The γ-ray angular distribution fits, in the centre-of-mass frame, for strongest transitions on the γ-ray spectrum. The initial and final spins of the transitions are labelled on each plot.

E_γ (keV)	I_i	I_f	α	ν	χ^2
625	11/2	9/2	6.16	-2.26	2.02
917	9/2	7/2	13.46	-5.22	2.87
1707	11/2	9/2	2.51	-0.82	0.75
1723	3/2	1/2	2.81	-0.93	1.17
	5/2	1/2	3.25	-1.11	1.11
2000	9/2	7/2	24.98	-9.84	3.26
2909	7/2	5/2	9.86	-3.77	7.91
3826	9/2	5/2	1.82	-0.57	0.84

Table 3.3: Summary of the γ-ray angular distribution fits, displayed in figure 3.30, for the spin assignments of the excited states in ^{23}F. The initial and final spins of the transitions are presented alongside the fitting parameters and χ^2 of each fit.

The plots on the bottom of figure 3.30 display the angular distribution fits for the 1723 keV γ ray, which is coincident with the 2241 keV transition. Previous experimental works on the nuclear structure of ^{23}F [68], tentatively assigned the 2241 keV state to be the single-particle proton state from the occupation of the $s_{1/2}$ orbital. As such, if this were a pure proton state, there would be no direct population via the one-neutron removal reactions on the ^{24}F. In this case, any apparent direct population would in fact be due to feeding from higher energy excited states. The alternative scenario is this state has a more mixed character, with a non-negligible neutron contribution. Either way, from the results of the γ-γ coincidence analysis, only the 1723 keV transition was observed to be in coincidence with the 2241 keV. Taking the final spin-parity of this transition to be $1/2^+$, from the proton occupation of the $s_{1/2}$ orbital [68], the spin of the 3964 keV excited state could be assigned to either 3/2 or 5/2, as the γ-ray angular distributions were essentially indistinguishable.

The spin assignments here show strong agreement with the results of the previous experimental works and the shell-model calculations, detailed in section 3.4.2. The assignments of all known states were correctly reproduced, however the transition intensities were too low to deduce the assignments of any new states. The 5534 keV level was assigned to be $11/2^+$ in the previous experiment [68], via comparison of the shell-model energies. Here, in the present results, this assignment has been confirmed by the measurement of the γ-ray angular distributions. As the *sd*-model space Hamiltonians could only predict positive parity states, the parity assignments of the excited states in ^{23}F were inferred through the comparison of the experimental levels, to the shell-model calculations. The deduced spins and parities are labelled on the full level scheme, displayed in figure 3.31 and table 3.4.

3.3.4 Summary

The outcome of the analysis of the Doppler corrected γ-ray spectrum of ^{23}F and the γ-γ coincidences, was the identification and measurement of seven new transitions and two new excited states. In addition, there were several transitions that were from states that were observed for the first time to be populated via the one-neutron removal reactions. This indicated that there could be weaker, unobserved transitions feeding these states, particularly in the case of the single-particle proton states, which should if they were pure protons states, have a negligible direct population. The new level scheme constructed from this analysis is displayed in figure 3.31, with the colours highlighting the new transitions and states. The green lines indicate states and transitions that are new, whereas the blue represents those that have been observed for the first time in this reaction. The black lines denote the states and transitions that were known and expected. The spin-parity assignments from the γ-ray angular distribution analysis are also present on the level scheme.

After the identification of the cascades in the γ-γ analysis, the branching ratios of the transitions from a state could be accessed, which was an important observable for the comparison to the shell-model calculations. Additionally, the individual cascades could then be simulated and fitted to the data, in the same way the transitions were in section 3.2.8, in order to extract the relative populations of the excited states in ^{23}F. A complete summary of the results from this analysis is displayed in table 3.4, with the energies, spins and relative populations of the states presented alongside the branching ratios and relative intensities of the γ-ray transitions. Table 3.4 also includes the new transitions that were unable to be placed in the level scheme, due to low intensities in the γ-γ coincidence analysis.

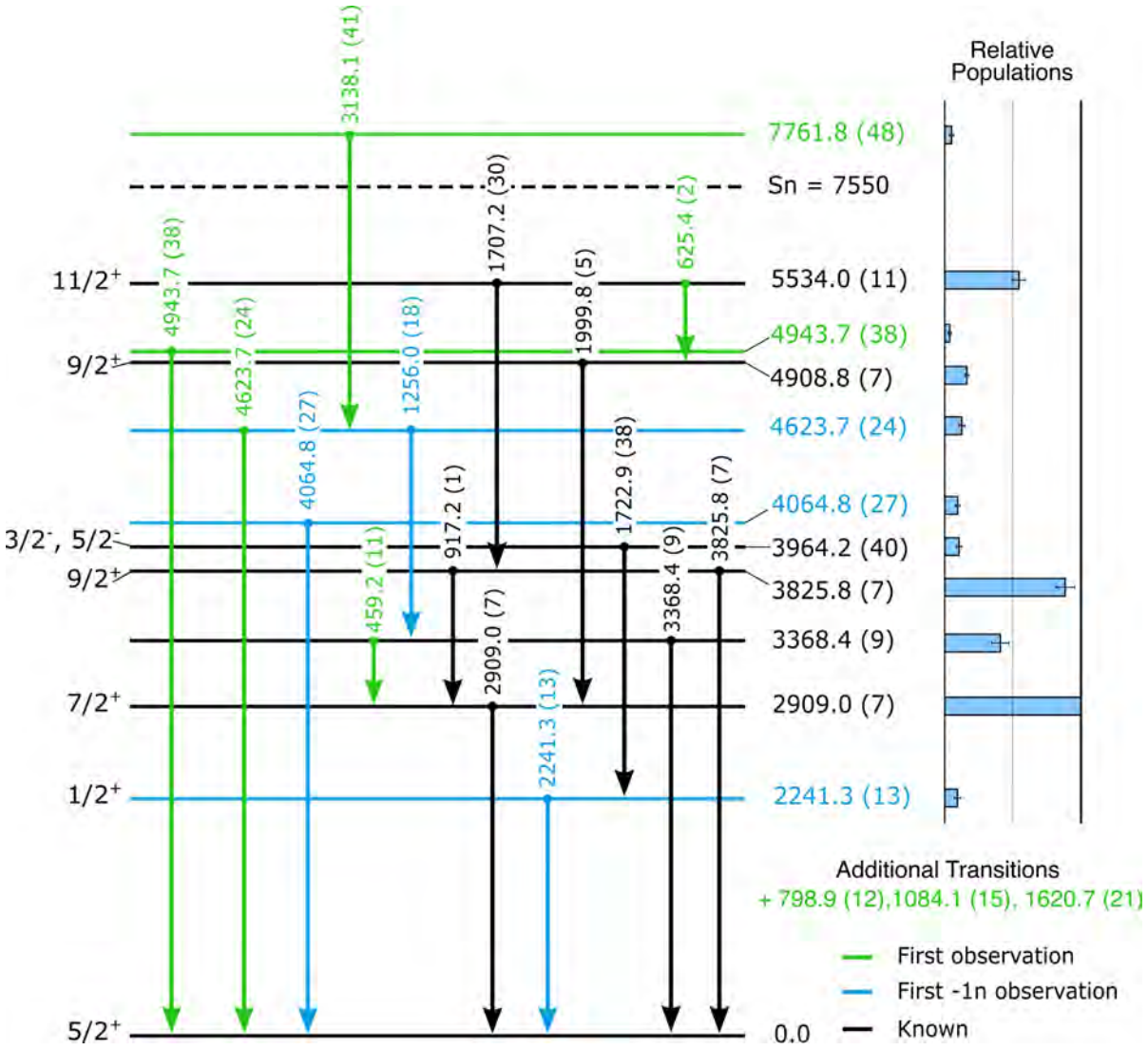

Figure 3.31: New level scheme of the excited states of ^{23}F, with the spin assignments from the γ-ray angular distribution analysis. The populations of the excited states relative to the 2909 keV are displayed to the right of the plot, and the additional transitions that could not be placed in the level scheme are noted. The green lines denote the states and transitions that are new, whilst blue highlights those that were observed for first time in the one-neutron removal reaction. The black lines indicate the states and transitions that have previously been identified.

E_{level} (keV)	J^{π}	Pop. $_{Rel.}$ (%)	E_{γ} (keV)	Int. $_{Rel.}$ (%)	B. R. (%)
2241.3 (13)	$1/2^{+}$	10.0 (18)	2241.3 (13)	10.7 (6)	100
2909.0 (7)	$7/2^{+}$	100	2909.0 (7)	100	100
3368.4 (9)	-	41.6 (59)	459.2 (11)	1.3 (3)	5.3 (14)
			3368.4 (9)	22.6 (7)	94.7 (62)
3825.8 (7)	$9/2^{+}$	89.3 (63)	917.2 (1)	30.3 (5)	50.9 (15)
			3825.8 (7)	29.3 (7)	49.1 (19)
3964.2 (40)	$3/2^{-}, 5/2^{-}$	11.2 (15)	1722.9 (38)	4.9 (8)	100
4064.8 (27)	-	10.2 (10)	4064.8 (27)	5.4 (6)	100
4623.7 (24)	-	13.2 (16)	1256.0 (18)	1.9 (4)	21.3 (57)
			4623.7 (24)	7.1 (5)	78.7 (111)
4908.8 (7)	$9/2^{+}$	16.9 (12)	1999.8 (5)	15.8 (6)	100
4943.7 (38)	-	4.4 (7)	4943.7 (38)	2.2 (4)	100
5534.0 (11)	$11/2^{+}$	55.3 (52)	625.4 (2)	7.6 (3)	28.1 (21)
			1707.2 (30)	19.5 (8)	71.9 (52)
7761.8 (48)	-	5.7 (13)	3138.1 (41)	3.2 (7)	100
-	-	-	798.9 (12)	2.4 (3)	-
-	-	-	1084.1 (15)	0.8 (3)	-
-	-	-	1620.7 (21)	2.0 (4)	-

Table 3.4: The full summary of the measurements from this analysis. The energies, spin-parity assignments and relative populations of the excited states are displayed alongside the energies, relative intensities and branching ratios of the transitions. The three γ rays at the bottom of the table could not be observed in the γ-γ coincidence analysis and consequently were not placed on the level scheme.

3.4 Discussion

The following sections discuss the experimental results of the ^{23}F, populated by the one-neutron removal reactions. Section 3.4.1 provides a brief overview of the prior experimental works studying the nuclear structure of ^{23}F. This is followed by a summary of the shell-model calculations in section 3.4.2. The key cascades in ^{23}F are then categorised and discussed, with reference to the previous experimental works and each of the shell-model calculations. A summary of the discussion can then be found in section 3.4.6, with the final remarks on the results.

3.4.1 Previous Experimental Works

The nuclear structure of ^{23}F has been studied previously, notably by Michimasa et al [68], via in-beam γ-ray spectroscopy following a variety of population reactions. Through the use of a cocktail secondary beam, the ^{23}F was populated by the α-inelastic scattering, proton transfer, one-neutron and two-nucleon knockout reactions. The population strengths for the excited states in ^{23}F were compared for each of these reactions, in order to deduce the nature of the excited states [99]. The experiment took place at the RIPS spectrometer of RIKEN, using the DALI2 scintillator array [100], for the detection of the γ rays.

An additional recent experiment on the nuclear structure of ^{23}F is presented in B. Pietras' doctoral thesis [69]. In this experiment, taking place at GANIL, the ^{23}F was also populated via one-neutron knockout reactions. Here, the γ rays were detected by a hybrid array of germanium EXOGAM [101] and NaI detectors. Additionally, in this experiment, the fragment longitudinal momentum distributions were measured in coincidence with select γ-ray energies, in order to determine the single-particle shell structures. The level schemes for these two experiments are displayed in figure 3.32, with the relative cross sections of the excited states from each reaction in Michimasa's experiment, displayed on the right. A comparison of the relative populations of the levels from the neutron knockout reactions, compared to the values of the present analysis, can be found in figure 3.33. The nuclear structure of ^{23}F has also been studied following the β decay of ^{23}O, which is reported in [67].

The notable difference between the experiment presented in this thesis and the previous experiments, besides the greater statistics, is the use of the GRETINA for the γ-ray detection. The tracking capabilities of GRETINA enabled a superior Doppler correction to be performed on the data, significantly improving the energy resolution of the Doppler corrected spectrum. This was of particular importance for the higher energy γ rays, which

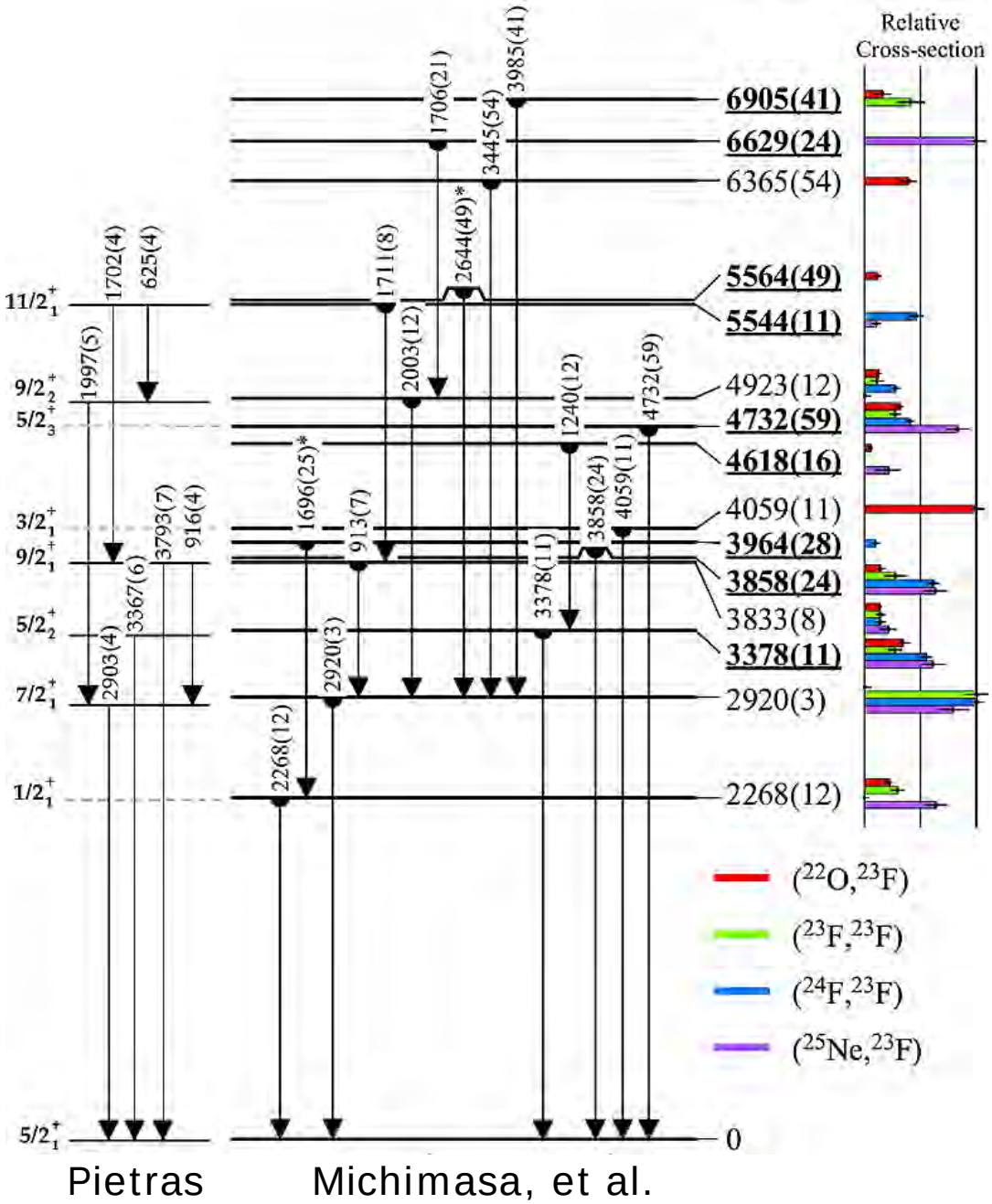

Figure 3.32: Comparison of the level schemes of two previous experiments studying nuclear structure of ^{23}F, adopted from [69] and with data incorporated from [99]. The spin-parity assignments of the previous analyses are labelled on the left, with the relative cross sections from each reaction, from Michimasa's data, shown on the right.

were more sensitive to the Doppler correction, and is the primary reason why several of the newly observed transitions were greater than 3.5 MeV. These high-energy γ rays were generally the direct transition to the ground state from many of the high-energy states in ^{23}F. These γ rays, in addition to the detection of the weaker, lower energy transitions, enabled the determination of the branching ratios, which were previously unable to be measured by Michimasa. The branching ratios were crucial observables for the comparison of the data to the shell-model calculations.

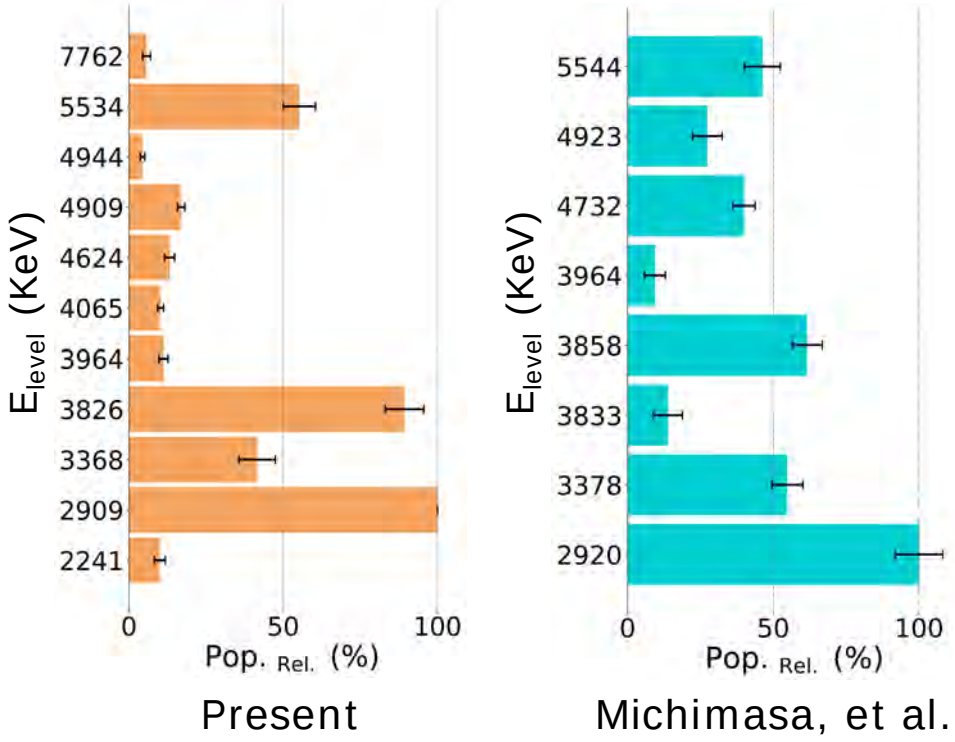

Figure 3.33: Comparison of the relative populations of the excited states in ^{23}F via the one-neutron removal reactions. Both sets of data display the populations as relative to the 2909 keV state. The plot on the right uses the level energies and relative populations from Michimasa's analysis, taken from table 5.3 in [99].

As can be seen from the comparison of the level schemes in figures 3.31 and 3.32, and the relative populations of the excited states following the one-neutron removal reactions, figure 3.33, the present data has several differences from that of Michimasa. Some notable differences include the excited states at 3858 keV and 4732 keV that were unable to be reproduced. Additionally, the 2241 keV and 4065 keV states were measured by Michimasa to have no population in the neutron removal channel, whilst having strong cross sections in the proton transfer channel. Thus these levels were assigned to be the single-particle proton states, corresponding to proton occupation in the $s_{1/2}$ and $d_{3/2}$ orbitals respectively. The apparent direct population of these two states in the present data could perhaps be indicative of unobserved feeding transitions, or of a more mixed character for these states,

with non-negligible neutron contributions. However in general, the relative populations of the excited states that were detected, were in broad agreement. The populations of 5.5 MeV states are just about within error of each other, as are the 3.8 MeV states, with the assumption that the two 3.8 MeV levels detected by Michimasa are the same state. The 3.3 MeV and 4.9 MeV states are slightly outside of the error ranges, whilst there is a strong agreement between the 3.9 MeV states.

3.4.2 Shell-Model Calculations

In addition to being compared with the previous experimental works, the present data was also compared to the phenomenological shell-model calculations of the nuclear structure of ^{23}F. The theoretical predictions for the excited state energies and γ-ray transitions were computed using the universal sd-shell ($0d_{5/2}$, $0d_{3/2}$, $1s_{1/2}$) Hamiltonians USD, USDA and USDB, which have provided realistic wavefunctions for nuclear structure models for a number of years [12, 13]. The calculations were also carried out using the new USDC interactions [102], to examine the predictive power of this revised Hamiltonian in the neutron-rich region of the nuclear chart. The calculations for each of the four interactions were carried out by Alex Brown [103], using the shell-model code NuShellx [104], with the proton and neutron effective charges of e_π = 1.36 and e_ν = 0.45 respectively [14]. Only the positive parity excited states could be computed via these calculations, due to the sd-model space.

The theoretical predictions of the excited state energies were compared to the experimental data, with the full range of calculated levels being displayed in the plots in figure 3.34. The levels that could be associated with an experimental excited state, via comparison of the energies, transitions, branching ratios and spins, are summarised in table 3.5. From these levels, the root mean squared (rms) of the difference between the theoretical and experimental excitation energies were computed, in order to assess the accuracy of each Hamiltonian [105]. The rms values for the USD, USDA, USDB and USDC Hamiltonians, with and without the inclusion of the 7762 keV state, are displayed below in table 3.6. The 7762 keV state was tentatively associated with the $1/2^+_4$ state in the shell-model calculations, via the comparison of the excitation energies and the strong branch to the 4624 keV state. However, as this isn't a definitive assignment, the rms values with the exclusion of this state are also presented in table 3.6.

Examination of the rms values presented in the table above, shows that the calculations using the USDA and USDB interactions were the most consistent with the experimental energy levels. The USD calculations produced the least accurate results, with the results from the new USDC Hamiltonian in the middle. This represents a slight step back in the

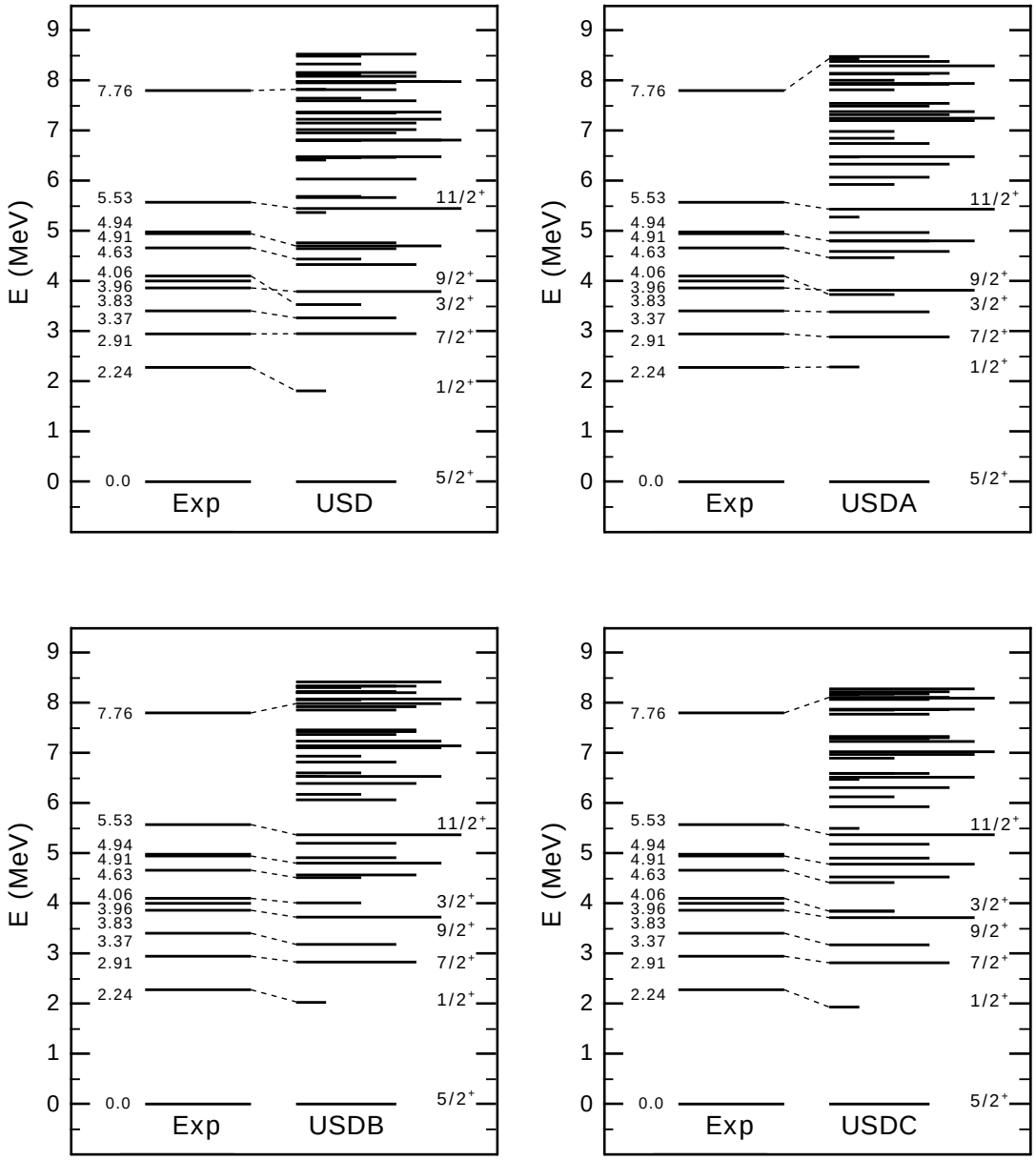

Figure 3.34: The theoretical excited states for each USD-type Hamiltonian, under 8.5 MeV, compared to the experimental energy levels. The cases where the experimental states could be associated with a theoretical level, are highlighted by the dotted lines.

Exp				USD				USDA				USDB				USDC			
E_{level} (MeV)	J^{π}	E_{γ} (MeV)	B. R. (%)	E_{level} (MeV)	J^{π}	E_{γ} (MeV)	B. R. (%)	E_{level} (MeV)	J^{π}	E_{γ} (MeV)	B. R. (%)	E_{level} (MeV)	J^{π}	E_{γ} (MeV)	B. R. (%)	E_{level} (MeV)	J^{π}	E_{γ} (MeV)	B. R. (%)
2241.3 (13)	$1/2^+$	2241.3 (13)	100	1776	$1/2^+$	1776	100	2253	$1/2^+$	2253	100	1991	$1/2^+$	1991	100	1898	$1/2^+$	1898	100
2909.0 (7)	$7/2^+$	2909.0 (7)	100	2916	$7/2^+$	2916	100	2852	$7/2^+$	2852	100	2796	$7/2^+$	2798	100	2781	$7/2^+$	2781	100
3368.4 (9)	-	459.2 (11)	5.3 (14)	3231	$5/2^+$	315	35.7	3352	$5/2^+$	500	28.3	3148	$5/2^+$	352	12.2	3139	$5/2^+$	358	15.9
		3368.4 (9)	94.7 (62)			3231	63.5			3352	71.7			3148	87.7			3139	83.9
3825.8 (7)	$9/2^+$	917.2 (1)	50.9 (15)	3757	$9/2^+$	841	34.1	3783	$9/2^+$	931	49.8	3692	$9/2^+$	896	54.2	3682	$9/2^+$	901	53.7
		3825.8 (7)	49.1 (19)			3757	65.9			3783	50.2			3692	45.8			3682	46.3
3964.2 (40)	$3/2^-, 5/2^-$	1722.9 (38)	100	-	-	-	-	-	-	-	-	-	-	-	-	-	-	-	-
4064.8 (27)	-	4064.8 (27)	100	3497	$3/2^+$	3497	100	3698	$3/2^+$	3698	99.9	3976	$3/2^+$	3976	100	3811	$3/2^+$	3811	100
4623.7 (24)	-	1256.0 (18)	21.3 (57)	4404	$3/2^+$	1173	14.1	4433	$3/2^+$	1081	43.2	4480	$3/2^+$	1332	64.1	4381	$3/2^+$	1242	50
		4623.7 (24)	78.7 (111)			4404	74			4433	37.2			4480	11.2			4381	27.9
						2628	10.9			2180	18.3			2489	24.1			2483	21.4
4908.8 (7)	$9/2^+$	1999.8 (5)	100	4664	$9/2^+$	1748	90.5	4767	$9/2^+$	1915	91	4769	$9/2^+$	1973	89.4	4748	$9/2^+$	1967	89.2
						907	2.5			984	3			1077	4.1			1066	4.1
						4464	5.8			4767	5.8			4796	6.3			4748	4.7
5534.0 (11)	$11/2^+$	625.4 (2)	28.1 (21)	5413	$11/2^+$	749	73.8	5400	$11/2^+$	633	51.1	5334	$11/2^+$	565	32.2	5335	$11/2^+$	587	34.6
		1707.2 (30)	78.9 (52)			1656	26.1			1617	48.2			1642	67.4			1653	65
7761.8 (48)	-	3138.1 (41)	100	7790	$1/2^+$	3386	76.2	8402	$1/2^+$	3969	40.8	8172	$1/2^+$	3692	32.1	8130	$1/2^+$	3749	42.6

Table 3.5: Comparison of the experimental excited state energies, spin-parity assignments, γ-ray energies and branching ratios, compared to the phenomenological shell-model calculations, for each interaction. In this table, the theoretical branching ratios are computed using the calculated γ-ray energies for each respective interaction. Only the theoretical states that could be associated with the experimental levels, see figure 3.34, are included here. The rms values of the differences between the experimental and computed energies are summarised in table 3.6.

	USD (keV)	USDA (keV)	USDB (keV)	USDC (keV)
Incl. 7762 keV	276.1	263.4	210.2	243.1
Excl. 7762 keV	292.7	163.9	169.3	222.6

Table 3.6: Root mean square analysis of the theoretical and experimental excited state energies, to assess the consistency of each Hamiltonian to the experimental data. The values with and without the inclusion of the 7762 keV level are displayed, due to the tentative association of this level with the $1/2^+_4$ state, see text.

predictive power of the new Hamiltonian in this region of the nuclear chart, compared to the older USDA and USDB interactions. All four of the Hamiltonians matched the spin assignments of the γ-ray angular distribution analysis and there was no clear interaction that best reproduced the experimental branching ratios.

In the sections below, each of the excited states are categorised according to the strongest cascades, or their apparent single-particle natures. The transitions, spin assignments and branching ratios are then discussed, with reference to the shell-model calculations and the previous experimental works.

3.4.3 The 2909 keV, 3826 keV, 4908 keV and 5534 keV States

The 2909 keV, 3826 keV, 4908 keV and 5534 keV states were among the most strongly populated excited states in the neutron removal reactions, the transition from which constitute the dominant cascades observed in the γ-ray spectrum. The 2909 keV state had the greatest the direct population by the reaction, and was observed to decay only through the direct transition to the ground state, in agreement with all four of the Hamiltonians. This 2909 keV γ ray was the final transition in many of the observed cascades, and was the most intense transition observed on the spectrum. Consequently, the populations and intensities of the other states and transitions are presented as relative to the 2909 keV. The γ-ray angular distribution analysis assigned this state to be $7/2^+$, which is in agreement with the shell-model predictions of the $7/2^+_1$ state at 2.9 MeV. The strong population of this state in the one-neutron removal reaction, coupled with the hindered population in the proton transfer reaction of Michimasa's data, suggests this is a neutron excitation.

The 3826 keV state was also observed to have a direct transition to the ground state, in addition to the 917 keV γ ray in coincidence with the 2909 keV transition. As a result of the

comparatively high resolution of the Doppler corrected γ-ray spectrum, an intensity measurement of the ground state transition could be performed. This enabled the calculation of the branching ratios to be 50.9 (15)% to the $7/2^+_2$ state and 49.1 (19)% to the ground state. This was in best agreement with the USDA calculations, which predict branching ratios of 49.8% and 50.2% respectively, followed by the USDB and USDC, with the USD calculations showing the greatest deviation from the data. Additionally, the angular distribution analysis of both of these γ rays, results in the assignment of $9/2^+_1$ to this state, which corroborates with all four of the Hamiltonians. The level scheme of Michimasa's data, figure 3.32, shows there to be two excited states at 3.8 MeV. Neither the present data nor the shell-model calculations can support this, with just the single 3826 keV state being observed. The relative population of this state is in agreement with Michimasa's, with the assumption that the two 3.8 MeV states are the same state, thus summing the populations. This 3826 keV level has already been discussed in [106], to be one of the excited states in ^{23}F that may be interpreted as the coupling of the single $1d_{5/2}$ proton to the 2^+ phonon state in ^{22}O.

The 4909 keV state was identified through the observation of the 2000 keV γ ray in coincidence with the 2909 keV transition. In the shell-model calculations, additional transitions to the 3826 keV level, as well as the ground state were predicted, which could be the observed 1084 keV and 4944 keV transitions respectively. The 1084 keV γ ray however, was not assigned to the level scheme as a consequence of it not being observed in coincidence with another transition. Whereas the 4944 keV transition was assigned to be from a distinct level from the 4909 keV state, due to the unexplained 35 keV energy difference and the fact that it was not observed to be in coincidence with the 625 keV transition. The measurements of the angular distributions of the 2000 keV γ ray suggests an assignment of $9/2^+_2$ to the 4909 keV state, which agrees with the shell-model calculations. The relative population of this state measured by Michimasa falls slightly out of error of the present value. Summing the values of the two 4.9 MeV states in this data (i.e assuming they are the same state) still does not quite cover this gap.

The final state in this section is the 5534 keV level, which has a significant population resulting from the neutron removal reactions, with comparable values in the present data and Michimasa's. This level constitutes the first state in several of the strongest cascades observed on the γ-ray spectrum. It decays via two pathways, the 1707 keV transition to the 3826 keV state and the 625 keV transition feeding the 4909 keV state, and was identified by the γ-γ coincidence measurements. The measured branching ratios for these transitions were 71.9 (52)% to the $9/2^+_1$ and 28.1 (21)% to the $9/2^+_2$, which show strong agreement with the USDB shell-model predictions of 67.4% and 32.2% respectively. The angular distributions of both of these γ rays and all four of the shell-model Hamiltonians, assign this level

to be the $11/2^+_1$ state.

3.4.4 The 2241 keV, 3964 keV States and 4065 keV States

The 2241 keV and 4065 keV states were considered by Michimasa et al. [68] to be the single-particle proton states for the $s_{1/2}$ and $d_{3/2}$ shells respectively, via the comparison of the population strengths of each reaction. As the ground state structure of ^{24}F has a single valence proton in the $\pi d_{5/2}$ shell, the population strengths of the proton single-particle states in $d_{3/2}$ and $s_{1/2}$, by the neutron knockout reactions, are expected to be significantly hindered. However in the present data, both of these states were populated and the transitions to the ground states were observed. As can be seen in figure 3.33, neither of these states were recorded to have any significant population in the previously measured neutron knockout reactions. This apparent direct population to these states in the present data, can be attributed either to the feeding from higher energy excited states that were not observed in the γ-γ coincidence analysis, or to a more mixed nature of the states, with a non-negligible neutron contribution.

The 3964 keV state was identified through the observation of the 1723 keV γ ray in coincidence with the 2241 keV transition. This state decays only to the first excited state and therefore contributes to the strength of the 2241 keV transition, observed on the γ-ray spectrum. However, the intensity of the 2241 keV transition cannot be solely accounted for by the 1723 keV feeding alone, which is why the plot in figure 3.33 displays some direct population to the state. As per the discussion above, this is either due to the indirect population from unobserved feeding transitions, or the mixed nature of the states. The angular distribution analysis was carried out for the 1723 keV γ ray, assuming the first excited state to be $1/2^+$, from the proton occupation of the $s_{1/2}$ orbital. From this, the 3964 keV state was deduced to be either 3/2 or 5/2, as the calculated angular distributions were essentially indistinguishable. As was discussed in [105], a negative parity is inferred for this state due to it not being reproduced by the shell-model calculations.

The $3/2^+$ assignment of the 4065 keV state from the proton occupation of the $d_{3/2}$ could not be confirmed in this analysis, due to the transition intensity being too weak for an angular distribution measurement. Nevertheless, the results do support this assignment due to the dominant branch to the ground state, when comparing to the shell-model calculations. However, all four of the Hamiltonians show a systematic underestimation of the energies of both of these states, where only the USDB and USDC calculations correctly reproduce the order of the $9/2^+_1$ and $3/2^+_1$ states.

3.4.5 The 3368 keV, 4624 keV and 7762 keV States

The final set of states to be discussed, the 3368 keV, 4624 keV and 7762 keV levels, contain cascades with several transitions that were observed for the first time in this analysis. These first time measurements enabled the identification of a new excited state and the calculation of branching ratios, which were compared with the shell-model predictions.

The first excited state to be discussed here, the 3368 keV level, was identified by the direct decay to the ground state. Additionally, the γ-γ coincidence analysis of the 2909 keV transition, enabled the observation of the 459 keV γ ray, decaying to the $7/2^+_1$ state. This transition was predicted by the shell-model calculations, but never before observed. The branching ratios of these transitions were measured to be 5.3 (14)% to the $7/2^+_1$ state and 94.7 (62)% to the ground state, which is in best agreement with the theoretical values predicted by the USDB calculations, 12.2% and 87.7% respectively. Through the comparison of the level energies and branching ratios to the shell-model calculations, this state could be associated with the $5/2^+_2$ level. This however, could not be experimentally verified by the angular distribution analysis of either γ ray, due to the low intensities.

The 4624 keV state, identified by the decay to the ground state and the 1256 keV γ ray in coincidence with the 3368 keV transition, was observed to be populated for the first time via the neutron knockout reaction. However, unlike the assumed single-particle proton states, the 2241 keV and 4065 keV levels discussed above, this state was expected to have some direct population. The reason why both of the decaying transitions were observed here for the first time, was likely the higher statistics for the weak 1256 keV transition, and the better Doppler correction provided by GRETINA, for the 4624 keV transition. The energy and transitions of this state are consistent with the $3/2^+_2$ predicted by the shell-model calculations, where the branching ratios of the two transitions are sensitive to which interaction was used. The experimental branching ratios were measured to be 78.7 (111)% to the ground state and 21.3 (57)% to the first excited $5/2^+$ state, showing best agreement with the USD calculations. Notably, in the shell-model calculations, there is an additional transition predicted by all four of the Hamiltonians to the $1/2^+_1$ level. This could be one of the unobserved transitions feeding the single-particle proton state, that was hypothesised above. The $3/2^+_2$ assignment inferred by the comparison to the shell-model calculations, could not be experimentally verified via the angular distribution measurements, due to the low intensities of both transitions.

The final excited state to be discussed is the 7762 keV level, which lies above the neutron separation energy of 7550 keV. This state was identified for the first time in the present data, through the observation of the new 3138 keV γ ray in coincidence with the 4624 keV tran-

sition. The 3138 keV transition was measured in the subtracted coincidence gating of 4624 keV, figure 3.29, to a confidence level of only 2.8σ. However, by gating on the 3138 keV region, the 4624 keV transition could be observed and fitted to approximately 3σ, therefore the transition was accepted. The 3138 keV transition was not observed to be in coincidence with the 1256 keV γ ray, though this was expected due to the low intensity of the 1256 keV transition. Clearly, the angular distribution measurements could not be performed for the 3138 keV γ ray. Nevertheless, through comparison to the shell-model calculations, the 7762 keV level is tentatively associated with the $1/2^+_4$ state, due to the energies and the strong branch to the $3/2^+_2$ state, see table 3.5. The possibility also exists however, that this could in fact be a negative parity state, and thus not reproduced in the *sd*-model space calculations.

3.4.6 Summary

In summary, the results of the present analysis contains many new features that were measured for the first time in this experiment, which are important for the detailed understanding of the nuclear structure of ^{23}F. The high-resolution Doppler corrected γ-ray spectrum, obtained through the tracking capabilities of GRETINA, together with the high statistics on the spectrum, enabled the measurement of several new γ-ray transitions and the identification of two new excited states. The new transitions allowed for the determination of the branching ratios for the first time, which were compared to the shell-model calculations. Additionally, several of the excited states were observed for the first time to be populated in the neutron removal reactions, including the $s_{1/2}$ and $d_{3/2}$ single-particle proton states of 2241 keV and 4065 keV respectively. The apparent direct population to these states could be indicative of unobserved feeding transitions, or suggests a more mixed nature for these states, with a non-negligible neutron contribution.

A new level scheme has been constructed using the analysis of the γ-ray spectrum and γ-γ coincidences. In general, the new level scheme in strong agreement with the shell-model calculations, spin-parity assignments from the γ-ray angular distribution analysis all being correctly reproduced. From the evaluation of the root mean square of the measurements and the predictions, it was determined that the calculations using the USDA and USDB interactions most correctly replicated the experimental energy levels, with the new USDC Hamiltonian performing slightly better than the USD interactions. However, it was clear that all four of the calculations systematically under predicted the excited state energies of the single-particle proton states, with only the USDB and USDC interaction correctly reproducing the order of the $9/2^+_1$ and $3/2^+_1$ states.

Finally, three of the newly identified transitions, the 799 keV, 1084 keV and 1621 keV, could

not be assigned to the new level scheme, due to not being observed in the γ-γ coincidence analysis. The limited geometrical coverage of GRETINA, resulting in the reduced γ-γ efficiency, constitutes one of the primary limitations in this analysis. If this experiment were to be repeated in the future, a greater γ-γ efficiency would be crucial to solving many of the remaining questions in the data set. These include the apparent direct population of the single-particle proton states via the neutron removal reactions, the placement of the new 799 keV, 1084 keV and 1620 keV transitions into the level scheme, and the question over whether the two 4.9 MeV states are indeed distinct levels. Additionally, a further experiment that could help unravel the mysteries of ^{23}F, would be the high-precision measurement of the γ-ray spectrum, using GRETINA, following a proton transfer or knockout reaction. This would enable a more thorough understanding of the nature of the assumed single-particle proton states and help to refine the predictive capabilities of the shell-model calculations in this region of the nuclear chart.

Chapter 4

Measurement of the Electromagnetic Transition Rates of ^{22}O

The neutron-rich oxygen isotopes, as was discussed in section 1.2, have proven to be effective for benchmarking the nuclear many-body methods using the chiral NN+3N interactions. The sensitivity to the inclusion of the 3N forces was demonstrated by the successful description of the anomalous location of the neutron drip line at ^{24}O, first by valence-space calculations [48], followed by the ab initio approaches [49, 50, 51]. Additionally, the recent report on the electromagnetic transition rates of ^{21}O confirms further sensitivities to these nuclear interactions, as well as examining the shell-model effective charges [55]. Figure 4.1, taken from the report, compares the experimental B(E2) transition strengths of the neutron-rich oxygen nuclei, to the calculations using the phenomenological USDB interactions and the VS-IMSRG method.

The shell-model calculations using the neutron effective charge of e_n = 0.45, obtained by fitting the experimental B(E2) values of *sd*-shell nuclei between A = 17-38, overestimate the transition strength of ^{21}O, suggesting a smaller than average effective charge. Using the reduced neutron effective charges detailed in [55], the calculations have significantly better agreement with the experimental B(E2) values for ^{21}O, but appear to disagree with the available data on the transition rates of ^{22}O. The electromagnetic transition strengths of ^{22}O have been measured only once before via a Coulomb excitation experiment, indirectly inferring the lifetime of the 2^+ 3199 keV state to be 690 ± 280 fs [56]. Consequently, the direct measurement of the lifetime of this state via DSAM, to both reduce the uncertainty and extract the B(E2) value without any model dependency, constitutes the primary objective of the experiment detailed in this chapter. This measurement would not only provide a key observable for testing the ab initio theories, but also the phenomenological approaches,

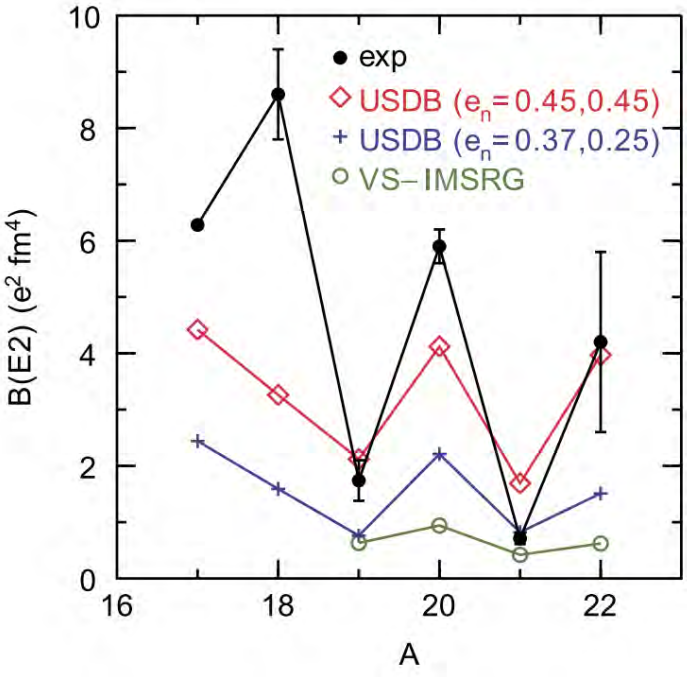

Figure 4.1: Comparison of the experimental B(E2) transition strengths ($1/2^+ \rightarrow 5/2^+$ and $2^+ \rightarrow 0^+$ for odd and even isotopes, respectively) of the neutron-rich oxygen nuclei, to those calculated using the phenomenological USDB interactions and the VS-IMSRG method. The improved reproduction of the experimental B(E2) value for ^{21}O is shown with the reduced neutron effective charges. The plot is taken from [55].

helping to improve the predictive capabilities of these methods in the vicinity of the neutron drip line.

The following sections present a detailed discussion of the measurement. Section 4.1 outlines the experimental setup, providing a brief review of the key components, how they function and why they were required for the measurement. Section 4.2 details the development and preparation of the novel ^{10}Be target, necessary to populate the ^{22}O via the fusion-evaporation reactions. The results of the experiment are then presented in section 4.3, with an in-depth discussion in section 4.4.

4.1 Experimental Details

The experiment to measure the lifetimes of the excited states of ^{22}O was carried out at Argonne National Laboratory (ANL), in April/May 2021. The technique that was employed to measure the lifetimes was the Doppler shift attenuation method (DSAM), which is de-

scribed in detail in section 2.4.1. DSAM was selected due to the technique's sensitive range of lifetimes overlapping with the expected lifetime of the first 2^+ state, which was indirectly inferred from the Coulomb excitation experiment to be 690 ± 280 fs [56]. At the velocities required for a sensitive DSAM measurement, the only feasible way to populate the excited states in ^{22}O was via the two-proton exit channel of the fusion-evaporation reaction of a ^{14}C beam on a ^{10}Be target. The ATLAS facility was able to provide the ^{14}C beam, see section 4.1.1, however this experiment necessitated the development of a novel ^{10}Be target, outlined in section 4.2. The γ rays emitted in-flight by the decay of the excited ^{22}O recoils, were detected by the tracking γ-ray detector array GRETINA, which was coupled to the FMA, to unambiguously tag onto the recoils of interest. A simple schematic drawing of the setup is illustrated below in figure 4.2.

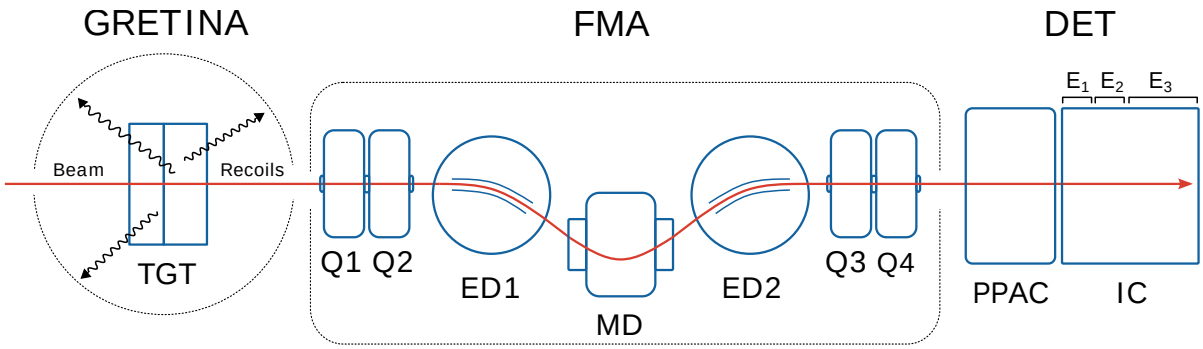

Figure 4.2: Schematic drawing of the experimental setup, demonstrating the positions and key components of GRETINA, the FMA and the recoil detectors.

The kinematics and cross sections of the fusion-evaporation residues for a range of ^{14}C beam energies, were studied using the PACE4 (Projection Angular-momentum Coupled Evaporation) fusion-evaporation code [107, 108]. As the plot in figure 4.3 suggests, the cross section for the population of the ^{22}O, indicated by the bold red line, was expected to peak with a ^{14}C beam energy of approximately 65 MeV. Thus, a ^{14}C beam was produced and accelerated by ATLAS to energies between 50-80 MeV, to find the optimum beam energy, and impinged upon the ^{10}Be target. The beams had an average current of 100 enA and were approximately 90 % pure, with an estimated 10 % ^{14}N contaminant. As can be expected from the fusion-evaporation reaction of two neutron-rich isotopes, the two-proton evaporation from the compound ^{24}Ne nucleus, to populate ^{22}O, was one of the weaker reaction channels. Indeed, the Monte Carlo cross-section calculations carried out using PACE4, indicates that across the optimum beam energies, the maximum yield of ^{22}O accounted for only 0.043% of the total residues. This highlights the necessity of the FMA to separate and identify the recoiling reaction products, so that the γ rays of interest could be measured.

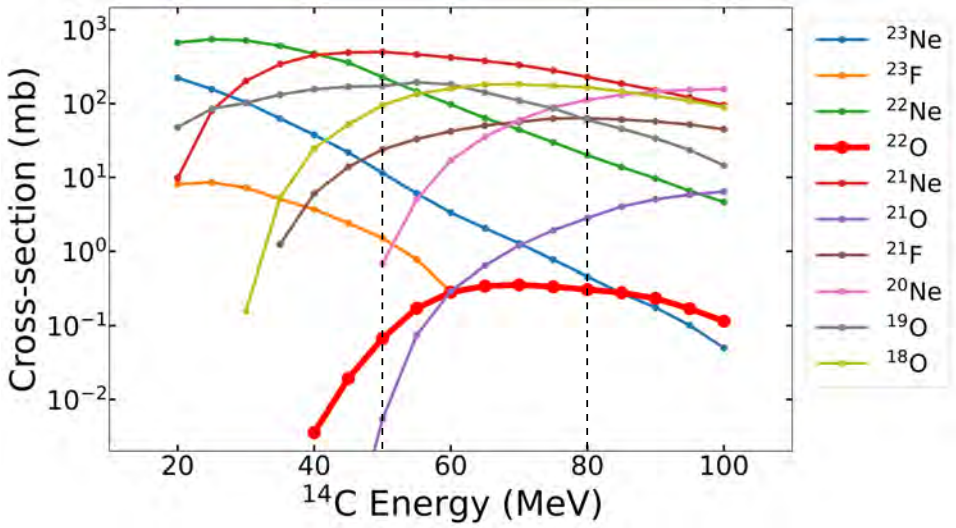

Figure 4.3: The cross sections of a selection of the strongest channels resulting from the fusion-evaporation reaction of a ^{14}C beam on a ^{10}Be target, calculated using the PACE4 code, across a range of beam energies. The ^{22}O cross sections are denoted by the bold red line, with the optimum beam energies highlighted by the dotted black lines.

The ^{22}Ne recoils, which were strongly populated via the neutron exit channels of the fusion-evaporation reactions on both the ^{9}Be and ^{10}Be in the target, were expected to dominate the focal plane of the FMA. Therefore, it was crucial that the recoils entered the detectors at the focal plane with sufficient energy for an effective separation according to their atomic number, via the E/ΔE measurement in the segmented ionisation chamber. Thus, a delicate balance had to be found in regards to the thickness of the target backing. The platinum backing, functioning as the degrader in the DSAM experiment, had to be thick enough to induce a lifetime-sensitive lineshape on the Doppler corrected γ-ray spectrum, whilst allowing the recoils to pass through with sufficient energy for the separation in the ionisation chamber. In addition, there was also a need for a degree of flexibility in the setup, as the experiment ran on several settings, scanning across the optimum ^{14}C beam energy range discussed above. On account of this, the targets were produced with a selection of three different backing thicknesses of 1 μm, 1.5 μm and 2 μm, which could be switched out during the experiment to a more optimal setting. However, in the course of the experiment, only the target with the 1 μm platinum backing was used, in order to enable an easier identification of the ^{22}O γ rays, see section 4.3.1.

4.1.1 ATLAS

The Argonne Tandem Linac Accelerator System (ATLAS) is a collection of superconducting linear accelerators (linacs) that has delivered heavy-ion beams up to uranium, with energies up to 17 MeV/u, for almost 50 years [109, 110]. The present ATLAS configuration that was used to deliver the ^{14}C beam to the target chamber, is illustrated by the floor plan in figure 4.4. The ^{14}C ions were produced in the electron cyclotron resonance (ECR) plasma ion source [111, 112], in which a neutral gas is fed in to a magnetically confined plasma chamber, then heated by microwave radiation. The microwaves generate a rapidly varying electric field which, when the frequency is equal to the electron gyration frequency ($\omega_g = eB/m_e$, where e and m_e are the electron charge and mass respectively and B is the magnetic field strength), results in the free electrons gaining energy [113]. Consequently, the energetic free electrons begin to ionise the neutral gas atoms, which in turn causes an avalanche of ionisation events, as more and more free electrons are generated. The ^{14}C ions were then extracted from the plasma chamber using a 350 kV platform and directed towards the next stages of acceleration.

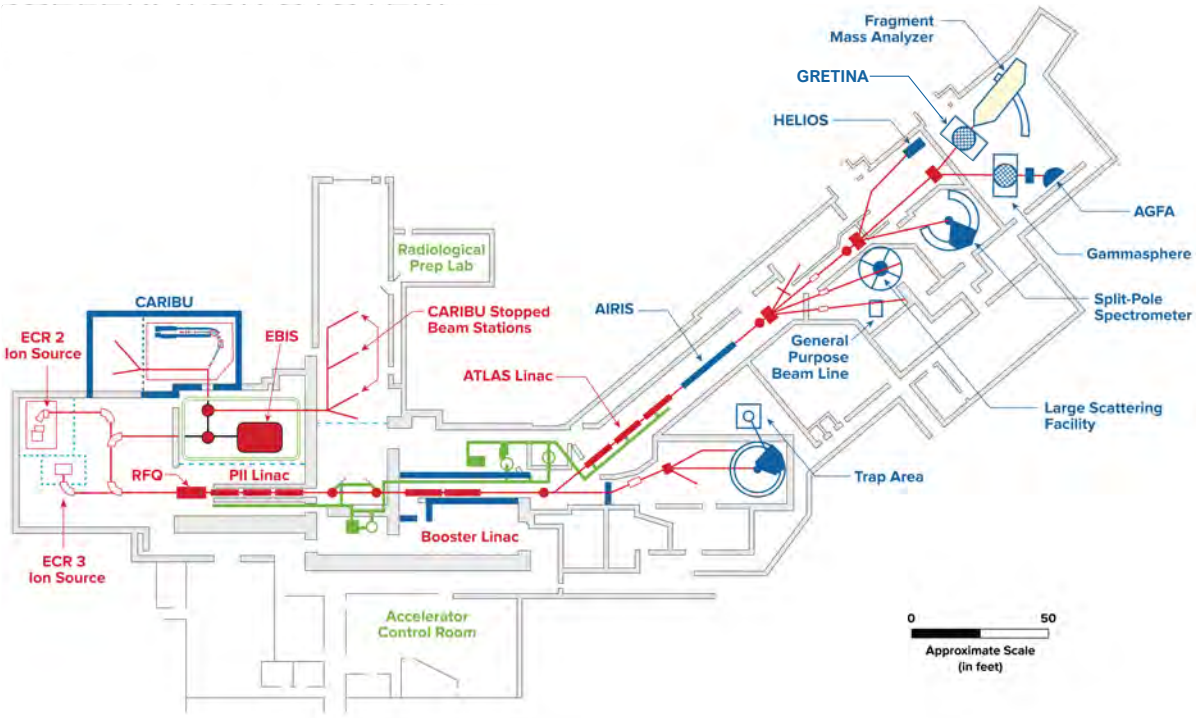

Figure 4.4: Schematic drawing of the ATLAS floor plan, modified to be up to date from [114], illustrating the positions of the ERC ion sources and linacs in relation to GRETINA and the FMA, in the experimental area.

After extraction, the ^{14}C ions were passed through the bunching system, to restrict energy spreading in the main linac system. A 12 MV preliminary accelerator, the Positive Ion Injec-

tor (PII), was then used to 'inject' the ions into the main linac system using 18 quarter-wave resonators, with 11 superconducting solenoids for focusing [115]. The main linac system comprises of the 20 MV 'booster' linac, followed by the 20 MV 'ATLAS' linac, consisting of 24 and 18 split-ring resonators respectively, and a total of 33 focusing solenoids [116]. These resonators are constructed from niobium, for the superconducting qualities, and cooled to 4.5 K using liquid helium [117]. Each of the resonators in the superconducting linac system can be phased independently, in order to allow for the selection of a range of beam energies. The ^{14}C ion beam, which was selected to have energies between 50 MeV to 80 MeV, was then directed to the experimental hall using ion optics, and impinged upon the target wherein the reactions took place.

4.1.2 GRETINA

The tracking γ-ray detector array, GRETINA, was again used for the detection of the γ rays emitted in-flight by the recoils. An in-depth overview of GRETINA and its operation has already been discussed in section 3.1.3. For this experiment, twelve detector modules were available, resulting in a solid angle coverage of approximately 1.6 π sr. As was previously discussed in section 2.4.1, the sensitivity of DSAM lifetime measurements are maximised at the forward and backward detection angles. However, the positioning of the FMA blocked the forward angles slots, so only the backward angles were available for use. With respect to the nominal target position, four of the GRETINA modules were placed at 148 degrees, another four at 122 degrees, with the final four mounted at the 90 degree position. One of the detector crystals in a 90 degree module was malfunctioning during the experiment, and so was switched off. Each detector crystal had a copper and tantalum absorber mounted to the face, to mitigate for the high rates of low-energy γ rays produced during the experiment.

4.1.3 FMA

The Fragment Mass Analyzer (FMA) is a recoil mass spectrometer at the ATLAS facility, that separates the recoiling reaction products from the unreacted beam and disperses them by their mass-to-charge ratios (A/q) at the focal plane [118, 119]. A set of recoil detectors enable the event-by-event identification of the reaction products, in order to tag onto the reaction channels of interest [110]. This is of particular importance for experiments studying weak reaction channels when there is a large background component present, as is the case with the ^{22}O. The FMA was positioned to be immediately following GRETINA, and was oriented to zero degrees with respect to the beam axis. In the schematic illustration in fig-

ure 4.2, the layout of the FMA is demonstrated, highlighting the positions of the ion optical-elements and recoils detectors.

The FMA is comprised of two electric dipoles and a magnetic dipole, which constitute the primary ion-optical elements, and a pair of quadrupole doublets for focusing and second-order corrections. The magnetic and electric dipoles are arranged symmetrically, with the magnetic dipole in the middle, so that both the position-energy dispersion and the angle-energy dispersion cancel, leaving only the dispersion in the A/q [118]. The electric and magnetic fields of these components are set so that the recoils of interest with an energy E_0, mass A_0 and charge q_0 are transmitted and focused to centre of the focal plane [113]. Mass selection can be provided through the use of adjustable mass slits, to select a range of A/Q to be transmitted. The FMA has a nominal energy acceptance of ± 20% around the E_0 and an angular coverage of approximately 8 msr [120]. After passing through the ion-optical elements, the reaction products enter the recoil detectors at the focal plane, which are outlined in the subsection below.

Recoil Detectors

A number of different detectors may be placed at the focal plane of the FMA, for the measurement of the outgoing particles. For the experiment described in this chapter, a multi-wired proportional counter (colloquially referred to as the PPAC) and an ionisation chamber (IC), were used for the event-by-event identification of the outgoing recoils. The dispersion of the reaction products at the focal plane of the FMA, according to their A/q, was measured by the PPAC, which enabled the identification of the recoil-mass groups [121]. The PPAC consists of a 15×5 cm isobutane gas chamber held at approximately 3 Torr and is bounded by two 0.8 μm mylar windows. Within the chamber are two mutually orthogonal wire grids, corresponding to the $x-$ and $y-$ directions, with the $x-$ grid in the direction of the recoil dispersion at the focal plane [122]. As the recoils pass through the PPAC, the gas within the chamber becomes ionised. The newly liberated electrons accelerate to the closest wire with sufficient energy to trigger additional ionisation events, resulting in an avalanche. The amount of charge collected by the wires is proportional to the energy loss of the recoil as it transits the target. However, in this analysis, the PPAC was primarily used for the positional information, which can be derived from the delay line readout of both ends of the two wire grids. In this way the 2-dimensional positions of the recoils at the focal plane of the FMA, can be measured to a resolution of approximately 1.2 mm.

After passing through the PPAC, the recoils immediately entered the ionisation chamber (IC). The IC is another isobutane gas chamber, with a depth of 30 cm, that measures the

energy loss of the recoils passing through it [123]. Similarly to the PPAC, when reaction products pass through the chamber they ionise the gas, producing electron-ion pairs. The electron and ions accelerate in an applied electric field toward the anode and cathode respectively. The charge collected at the electrodes is proportional to the energy deposited by the recoil moving through the gas, which itself is proportional to the square of the charge Z, as is specified by the Bethe formula in equation 2.9. Thus, by measuring the energy loss of the recoils, the atomic number Z, can be derived. The pressure of the isobutane gas can be set to be between 10-50 Torr to alter the energy loss characteristics of the recoils and maximise the efficiency of the IC. To reduce pile-up at high count rates, the anode has three segments along the beam direction, as can be seen in figure 4.2, and several perpendicular. Additionally, a Frisch grid is placed parallel to the anode to reduce the signal rise time and increases the pulse height, thus improving the quality of the measured signals [113]. By using the energy losses measured by the IC to get the atomic number, in tandem with the positional data from the PPAC to get the mass, the recoils could be identified and used for recoil-γ coincidences, to tag onto the reaction channels of interest.

4.2 Development of a Novel ^{10}Be Target

To populate the excited ^{22}O recoils, via the ^{14}C(^{10}Be,2p)^{22}O reaction, it became necessary to develop a novel ^{10}Be target, on a thin backing. In general, the use of a radioactive target in an experiment can introduce a number of challenges, particularly when used in conjunction with a radioactive beam, as is the case in this DSAM measurement. However, the ^{10}Be constitutes an appealing target material, in part due to its neutron-rich composition, with four protons and six neutrons, but also as a result of its longevity, with a half-life of 1.39×10^{6} years. Needless to say, the successful development and manufacture of this target would have applications beyond just this experiment, with an improved experimental accessibility to the light neutron-rich region of the nuclear chart. This could lead to applications in other high-precision nuclear structure measurements, as well as in nuclear astrophysics experiments, studying reactions on light neutron-rich nuclei. Therefore, the development and subsequent characterisation of this target, became an additional focus for this work.

In the following sections the development of the new target is outlined. Section 4.2.1 begins with an overview of the source and extraction of the ^{10}Be, followed by a discussion of the general requirements of the target and the different manufacturing techniques in section 4.2.2. The final target preparation procedure is then outlined in section 4.2.3.

4.2.1 Extraction and Isolation of ^{10}Be

The production of the ^{10}Be target was undertaken as part of a collaboration with the Isotope and Target Chemistry group of the Paul Scherrer Institut (PSI), in Switzerland. At PSI, a wide variety of rare and exotic radionuclides are produced in the components of the 590 MeV proton cyclotron facility, that are in many cases difficult to produce via other means [124]. The ongoing project ERAWAST (Exotic Radionuclides from Accelerator Waste for Science and Technology) at PSI, aims to identify and separate the radioisotopes that are scientifically relevant, for use in research and technology. The ^{10}Be is produced in large quantities at the PSI muon production facility, the Swiss Muon Source (SμS), via high-energy proton spallation in polycrystalline graphite wheels [125]. The irradiated graphite wheels typically have lifetimes of approximately 3-4 years, after which they are decommissioned and sent for chemical separation and disposal.

The most dominant radioisotope produced by the fast proton spallation in the graphite wheel is ^{7}Be, with a half-life of 53.3 days and a nominal activity in the TBq range after irradiation. The wheels are left for approximately 3 years, so that the ^{7}Be decays to levels safe for handling, then transferred to the radioactive laboratory for chemical separation. The graphite is cut into smaller chunks and burned in a stream of oxygen at 1000 °C, incinerating roughly 25 grams of irradiated carbon every 6 hours. After the combustion, the solid residues of the spallation products, including Li_2O, BeO, B_2O_3, are recovered from the carbon. A complete overview of the procedure to separate the residues can be found in [126], however in brief, it involves the complete dissolution of the residues into nitric acid. The beryllium, in the form of $Be(NO_3)_2$ can then extracted from the other impurities, through the use of resins. This process enables a near total recovery of the beryllium from the carbon, extracting up to 40 μg of Be per gram of C. The isotopic ratio of the recovered beryllium was measured via inductively coupled plasma mass spectrometry (ICP-MS) in 2017, to be ^{9}Be/^{10}Be = 2.110 ± 0.063, corresponding to a ^{10}Be enrichment of 32 ± 1%. At the time of writing, this constitutes the highest quality source, with the greatest quantity, of ^{10}Be available for research. The task therefore, was to develop a method of depositing the beryllium onto a substrate backing, in order to construct a target suitable for the DSAM experiment at ANL.

4.2.2 Target Development

To prepare a target of suitable quality for the high-precision DSAM experiment, a number of requirements had to be considered. First, the target must consist two layers; the "target

layer" or excitation layer, in which the reactions on the ^{10}Be take place, and the backing or degrader, which induces the energy loss of the recoils for the DSAM measurement. The target layer should be of sufficient thickness to produce the statistics necessary for an accurate measurement, whilst being thin enough so that most of the recoil energy loss takes place in the degrader, to induce the lineshapes. A target layer that is too thick will result in ^{22}O recoils being produced with a larger energy spread, which will make the DSAM measurement more difficult. In addition to producing the recoils of interest, and degrading their velocity, both layers must also allow the recoils to pass through and enter the FMA with sufficient energy, greater than approximately 0.75 MeV/u, for a good separation via the E/ΔE measurement in the IC.

Another property of the target to be considered, is the material enrichment. Ideally the target should be as chemically pure as possible, as any impurities in the target layer represent a "wasted thickness", and impurities in the backing make the velocity degradation of the recoils harder to predict. Inline with the previous point, the energy loss of the beam and recoils through both layers of the target should be predictable, which means that in addition to being pure, the target material must be homogeneous and have a uniform distribution. Any surface roughness of the target material, would again increase the energy spread of the ^{22}O recoils, reducing the precision with which the lifetime can be extracted. The final, and perhaps less apparent property of the target to take into account, is the mechanical stability. The target material must adhere well to the substrate backing and be able to withstand the thermal stresses of the beam, to avoid the wasting of material and the accidental contamination of the experimental area. In addition, the target must also be durable enough to survive minor handling and the shipment to the experimental facility.

The different target preparation techniques can be generally be grouped into three distinct categories: mechanical, chemical and physical [127]. The mechanical techniques are usually suitable for self-supporting thin metal targets, via cold rolling, or for targets made from a powder material, via tablet pressing or powder compacting. The physical techniques typically involve the physical deposition or implantation of the target material onto a backing, via physical vapour deposition (PVD), droplet deposition or ion-beam sputtering, and so could be suited for the production of the ^{10}Be target. The chemical methods could also be suitable, depositing the target material on a substrate backing from aqueous media, as in electrodeposition, or from an organic solvent, as in the molecular plating technique. Each of these methods produce targets with different characteristics, have varying yields and are effective with different types of materials. During the early development of the target, a number of these methods were tested, in order to devise an appropriate procedure which prepares the targets according to the criteria required for the experiment [128].

Two of the most direct methods of depositing the target material on to the backing are the physical vapour deposition (PVD) and the droplet deposition. The PVD technique is based upon the evaporation of the target material from a heated crucible, in a high vacuum (10^{-5} mbar), and the subsequent collection onto a substrate placed above the vapour source [129]. The advantage of this method is the creation of a thin, uniform and homogeneous layer on the substrate backing, where the amount of material deposited can be precisely measured using a quartz balance. This method does however come with a significant drawback of a very low deposition yield, which would mean the wasting of valuable target material, as well as the contamination of the equipment with ^{10}Be. Consequently, this technique was ruled out. The droplet deposition method, which involves the deposition of the target material in an aqueous solution via a droplet, had no such disadvantage, with an almost 100% yield barring the traces of material residue left behind on the equipment.

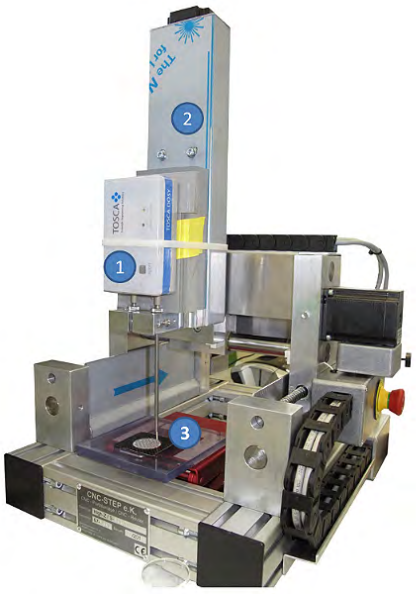

Figure 4.5: Photograph of the setup used for the droplet deposition tests, taken from [130]. The DOSTAL DOSY device (1) [131] was mounted on a 3D positioning system (2), in order to precisely deposit a known quantity of the target material onto the backing (3), in a controlled manner.

The droplet deposition method was extensively tested by depositing droplets of aqueous $Be(NO_3)_2$ onto a selection of carbon backings, using ^{9}Be spiked with ^{7}Be, to test the yield, adherence and spatial distributions of the residues after evaporation. The deposition was carried out using a DOSTAL DOSY device [131], pictured in figure 4.5, which was mounted on a 3D positioning system to enable the precise positioning of the droplets, as well as control over the amount of material deposited [132]. These early tests were characterised using

α spectroscopy to measure the target thicknesses and radiographic imaging to monitor the residue distributions. It was clear from these tests that once the droplets had evaporated, the residues that were left behind were not uniform, forming the characteristic "coffee ring" structures illustrated by figure 4.6 [133, 134]. The formation of the residue structures were also particularly sensitive to the ambient conditions during the deposition, resulting in an unpredictable distribution of target material on the substrate backings.

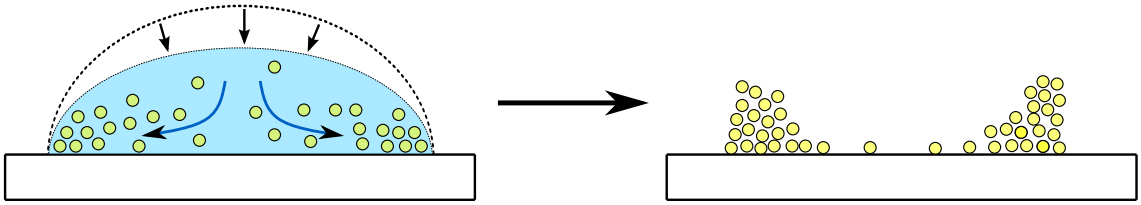

Figure 4.6: Illustration of the formation of the characteristic coffee ring residue structure, caused by suspended material in an evaporating droplet. The effect was first understood by Deegan et al. [133] to be caused by an outward capillary flow of the solvent during evaporation, resulting in the transport and accumulation of the suspended material at the droplet edge. Thus, a non-uniform and inhomogeneous distribution of target material is deposited on the backing.

An additional complication with the droplet deposition method was that the $Be(NO_3)_2$ residues did not solidify upon drying, instead forming a polymeric jelly which did not adhere well to the backing. This raised concern over the durability of the target material in the beam and during handling. The final problem with this method was the low chemical purity of the deposited residue. The beryllium constitutes just 6.7% of the material mass of $Be(NO_3)_2$, which when coupled with the ^{10}Be enrichment of 32%, results in just over 2% of the deposited material being useful to the experiment. Therefore, to deposit enough ^{10}Be for a sufficient production of ^{22}O, an impractical quantity of the $Be(NO_3)_2$ solution would need to be deposited onto the backing, further exacerbating the issues discussed above. Consequently, it became clear that the physical deposition techniques were unsuitable for the preparation of the target, and that the chemical deposition methods would be required.

As was previously mentioned, these early tests were carried out using thin amorphous carbon foils as the substrate backings. The reasoning was that due to the low atomic number and density of the carbon, the ^{22}O recoils would lose energy over a greater distance, increasing the sensitivity of the setup for lifetimes over 1 ps. This approach was revised when switching to the electrodeposition techniques, that are described below, in favour of heavier metal foils, such as platinum. These new foils were more durable, giving them a

better chance of surviving the deposition process, as a frequent issue with the carbon foils was their fragility leading to breakages during preparation. An additional advantage of the platinum foils was that the ^{14}C beam energy would be below the coulomb barrier, thus significantly reducing the additional count rates resulting from the reactions in the backing.

The technique selected for the preparation of the final target was the molecular plating method, in which the target material is electrodeposited onto a substrate, from an organic solvent [135]. The deposition is usually carried out in a two-electrode cell, where the material is deposited onto a backing on the cathode surface, as is demonstrated by the schematic in figure 4.7. The use of an organic solvent during molecular plating, compared to standard electrodeposition from an aqueous solution, has the advantage of lower current densities, reducing the rate of production of H_2 near the cathode, which could interfere with the layer formation on the substrate surface [136]. In general, targets produced via molecular plating have a structurally stable, uniform and homogeneous layer, with a high attainable deposition yield of 85-95%, depending on the conditions during deposition. Despite being a widely used technique for the production of nuclear physics targets, there has been remarkably little work studying the electrochemical processes in the vicinity cathode, or on the characterisation of the deposited layers. However, a recent study by Vascon et al. [137], suggested that the elements of interest are rarely deposited in their original compounds, instead being deposited in their hydroxide or possibly carboxylate or oxide species. This would represent a significant improvement of the chemical purity of the deposited material, over the $Be(NO_3)_2$.

4.2.3 Final Target Preparation

The targets used in the experiment were prepared by Emilio Andrea Maugeri at PSI, by adding the aqueous $Be(NO_3)_2$ starting material to 10 ml of inorganic solvent, consisting of 90% isopropanol and 10% isobutanol, then loading the solution into the molecular plating cell. A constant 200 V was applied across the solvent, producing a current ranging from 0.45 mA to 0.13 mA. The generated electron flux results in the reduction (gaining electrons) of the water molecules in the vicinity of the cathode and the oxidation (loss of electrons) of the water near the anode, see figure 4.7. The OH^- (aq) near the cathode reacts with the Be^{++}, produced by the complete dissociation of the $Be(NO_3)_2$ in H_2O, to Be^{++} and $2NO_3^-$, to form $Be(OH)_2$. Once the $Be(OH)_2$ reaches saturation in the organic solvent, it precipitates onto the cathode where the platinum backing is placed. As has been previously mentioned, the exact processes of the deposition near the cathode are not entirely understood, however these reactions for the molecular plating of beryllium hydroxide onto the platinum backing,

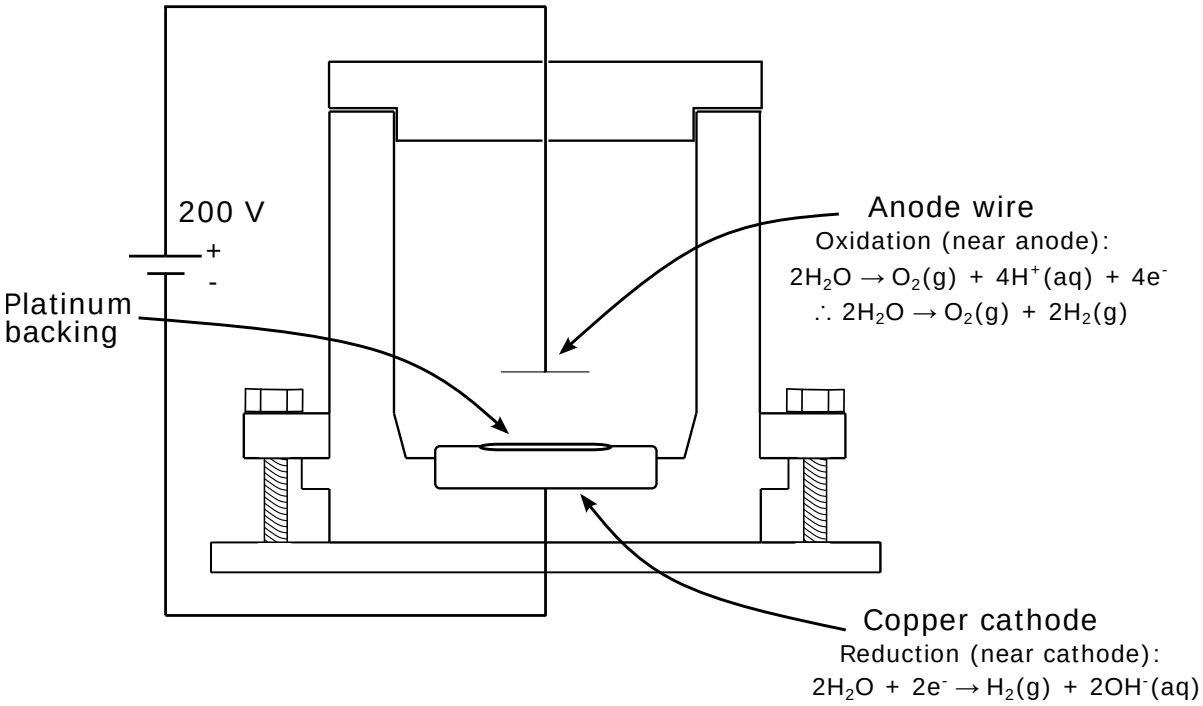

Figure 4.7: Schematic illustration of the molecular plating chamber, in which the $Be(OH)_2$ was deposited onto the platinum backings. The chemical reactions in the vicinity of the anode and cathode are annotated.

are expected to be the most likely [138].

Using the method described above, 192 μg of beryllium, in the form of $Be(OH)_2$, was deposited onto a selection of thin platinum foils with thicknesses of 1 μm, 1.5 μm and 2 μm, to provide some flexibility in the setup, during the experiment. The rolled platinum foils were provided by Goodfellow, with a quoted purity of 99.95% and a thickness tolerance of $\pm$ 25% the nominal values [139]. The depositions were over an approximately 7 mm diameter area on the platinum backings, resulting in a rough beryllium thickness of 500 $\mu g/cm^2$, corresponding to 160 $\mu g/cm^2$ of ^{10}Be. This amount of deposited material with these backings, was calculated using detailed GEANT4 simulations of the setup, to be sensitive to the expected lifetime of the first 2^+ of ^{22}O, whilst allowing the recoils to enter the FMA with sufficient energy for a good separation.

The yield of the beryllium deposition was estimated, via activity monitoring, to be between 30-40%. Consequently, the areal density of the ^{10}Be in the target area, was reduced to approximately 50 $\mu g/cm^2$, a quantity which challenged the viability of the experiment. The deposition yield of the molecular plating technique is sensitive to a number of conditions, such as the pH, voltage, current and deposition time [130]. Therefore it is clear this procedure requires further refinement in order to optimise these parameters, maximising the yield for future target preparations. Additionally, the unknown composition of the target

Figure 4.8: Images of the final targets that are being prepared to be irradiated by the ^{14}C beam at ATLAS.

layer, namely the quantities of the deposited oxygen and hydrogen, density of the material, and whether additional contaminants were introduced during the deposition, also posed significant challenges to the experiment. The characterisation of the new ^{10}Be target was therefore performed after the experiment, see section 4.4.1, to address these issues and help steer the future developments of the target. These results could assist in the development a more robust procedure for the preparation of the radioactive ^{10}Be target, which could prove to be a useful tool in the study of light neutron-rich nuclei.

4.3 Results

The experiment was carried out using six primary run settings, outlined below in table 4.1, with a range of ^{14}C beam and FMA parameters, to maximise the production and acceptance of the ^{22}O recoils. Despite scanning across the optimum beam energies calculated by PACE4, no γ rays originating from ^{22}O were observed during the course of the experiment. However, after a thorough analysis and careful gating of the data, discussed in the following sections, a weak peak structure that could correspond to the expected 3199 keV γ ray was observed exclusively in experiment setting 2. This observed γ ray, if it was indeed from the decay of the 2_1^+ state in ^{22}O, had too few statistics for the DSAM measurement to be performed. To understand why the observed rates of the ^{22}O γ rays were several orders of magnitude below what would be expected with the setting parameters in table 4.1 and the PACE4 cross sections in figure 4.3, a selection of other channels populated by the fusion-

Setting	E_{Beam} (MeV)	I_{Beam} (enA)	Target	Q_0	A_0	E_0 (MeV)	Run Time (hrs:mins)
1	80	24	^{10}Be	7	22	30	9:32
2	60	75	^{10}Be	7	22	24.2	17:12
3	60	150	^{9}Be	7	21	33	15:42
4	60	100	^{10}Be*	7	22	26	22:47
5	50	75	^{10}Be	6	22.5	21	12:46
6	50	90	^{10}Be	7	23	21	43:50

Table 4.1: The major run settings used during the experiment, detailing the beam current and energies, target configuration, FMA setting and run time for each setting. The ^{10}Be refers to settings that were using the novel ^{10}Be target, the ^{9}Be refers to the setting where a pure 100 μg/cm^2 ^{9}Be target was switched in and the asterisk indicates that the target was flipped so that the beam encountered the platinum backing first.

evaporation reactions were analysed. The results of this analysis and the implications on the novel ^{10}Be target and the future of this experiment are discussed in section 4.4.

The GRETINA array was calibrated by measuring the ^{56}Co, ^{152}Eu, ^{88}Y and ^{16}O sources, that were placed in the target position, see the spectra in figure 4.9. By calculating the relative deviations of the measured energies from the expected γ-ray energies, across all of the γ rays from the sources, the quality of the calibration can be inferred. From figure 4.10, it can be seen that the energy measurements are generally within 0.1% of the expected values, across the measured energy range, suggesting a good calibration. In this experiment, a ^{16}O source was included, so that the calibration could be performed up to 6.1 MeV, preventing the introduction of the systematic uncertainty when measuring higher energy γ rays, as was the case with the NSCL experiment in the previous chapter. The relative γ-ray detection efficiencies were again determined by fitting the fifth order of efficiency curve equation 3.4 to the ^{56}Co and ^{152}Eu sources, using the 846.7 keV γ ray as the reference energy. The fitted efficiency curve is displayed on the right of figure 4.10, with the optimum coefficients of a_1 = 0.0202, a_2 = -0.4332, a_3 = -0.0980, a_4 = -0.0746 and a_5 = 0.0138.

The GEBSort package was used for the initial unpacking of the data, with the rest of the analysis performed using ROOT [85]. Most of the techniques that were employed for the analysis of this data set have already been discussed in the previous sections, however any deviations from those methods will be highlighted in the following discussions. The analysis of the ^{22}O data is presented first in section 4.3.1, emphasising the particle identification and the gates required to observe the potential 3199 keV peak. This is followed by a dis-

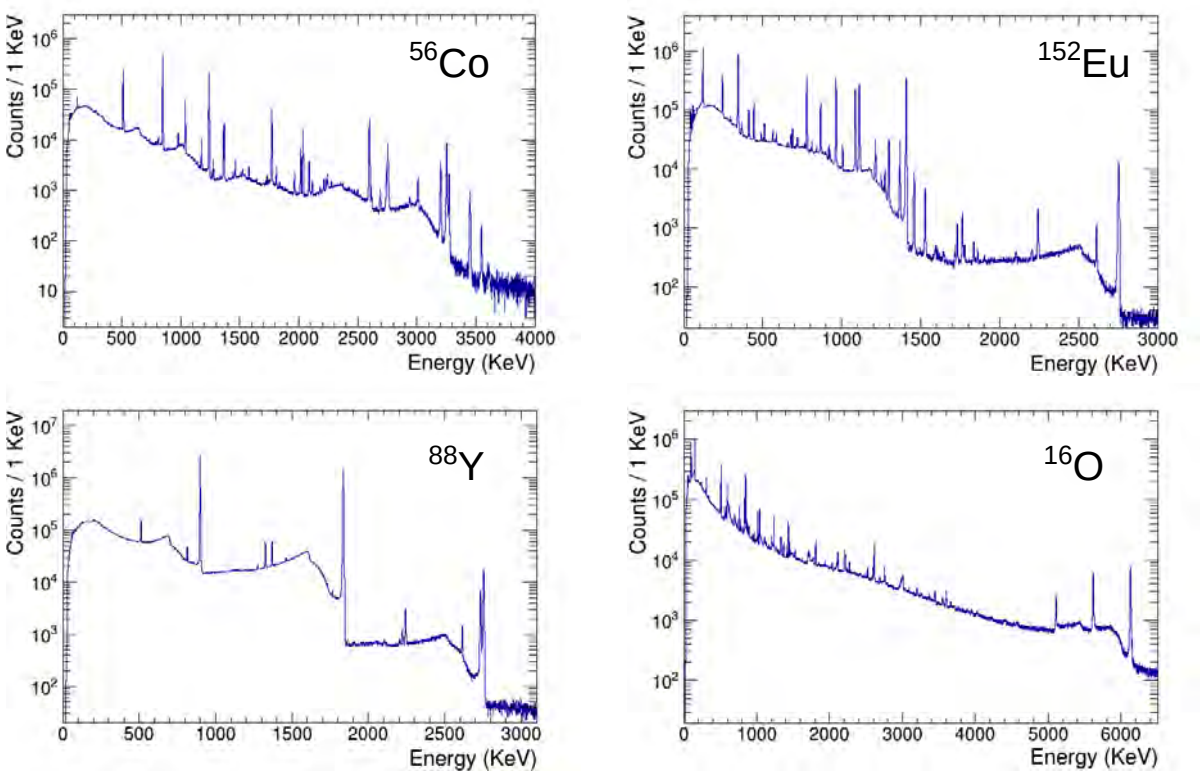

Figure 4.9: ^{56}Co (top left), ^{152}Eu (top right), ^{88}Y (bottom left) and ^{16}O (bottom right) source measurements for the energy and efficiency calibration of GRETINA.

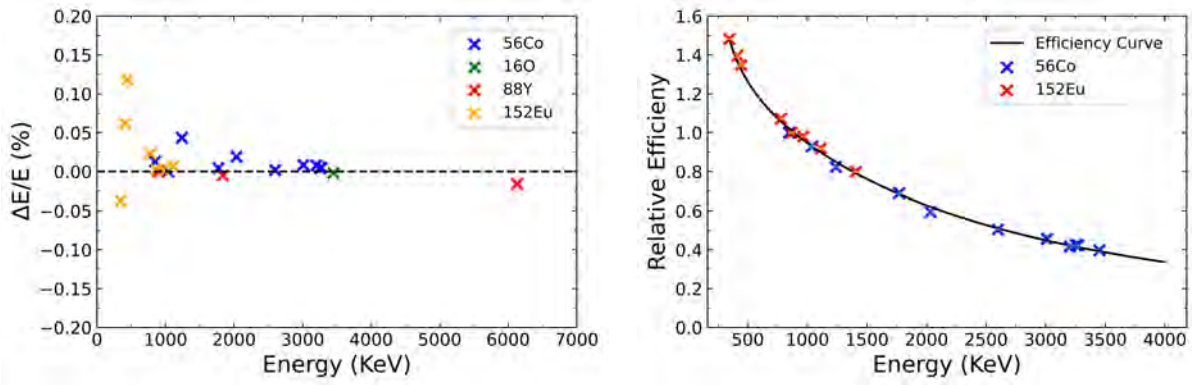

Figure 4.10: The plot on the left is the relative deviations of the measured energies from the expected γ-ray energies of the ^{56}Co, ^{152}Eu, ^{88}Y, ^{16}O sources, for each transition. It demonstrates a good quality calibration across the measured energy range, from 300 keV to 6.1 MeV, with most of the measurements within 0.1% of the expected values. The right plot is the relative detection efficiencies plotted against the γ-ray energies for the ^{56}Co and ^{152}Eu sources, normalised to the 846.7 keV γ ray and fit with equation 3.4. The parameters of the fit are shown in text.

cussion on the low rates in section 4.4, evaluating the novel ^{10}Be target material content and analysing the ^{22}Ne and ^{21}O channels, to determine the recoil acceptance into the FMA. Finally the future of the novel ^{10}Be target and of the DSAM measurement are considered in section 4.4.4.

4.3.1 Search for ^{22}O

A peak structure that could correspond to the 3199 keV γ ray, from the 2_1^+ of ^{22}O, was only observed in a single experimental setting. This setting was with an incoming ^{14}C beam energy of 60 MeV and was with the FMA set to an E_0 of 24.2 MeV, a q_0 of 7^+ and an A_0 of 22, which ran for approximately 17 hours. The gatings on the outgoing reaction recoils, to tag onto the ^{22}O, are demonstrated in the particle identification plots presented in figures 4.11 and 4.12. The Doppler correction of the spectra was carried out using the positional information from the PPAC to determine the beam direction and the A_0 and E_0 settings of the FMA to calculate the correction velocity of $\beta = 0.0486$. This is not a perfect assumption, as it requires a uniform velocity distribution across the ± 20% E_0 energy acceptance of the FMA. However, as the kinematics plot in figure 4.16 (page 134) shows, the recoil velocity distributions were expected to be broad, and with the FMA being set to the centre of the expected energy distributions, this was a reasonable first approximation.

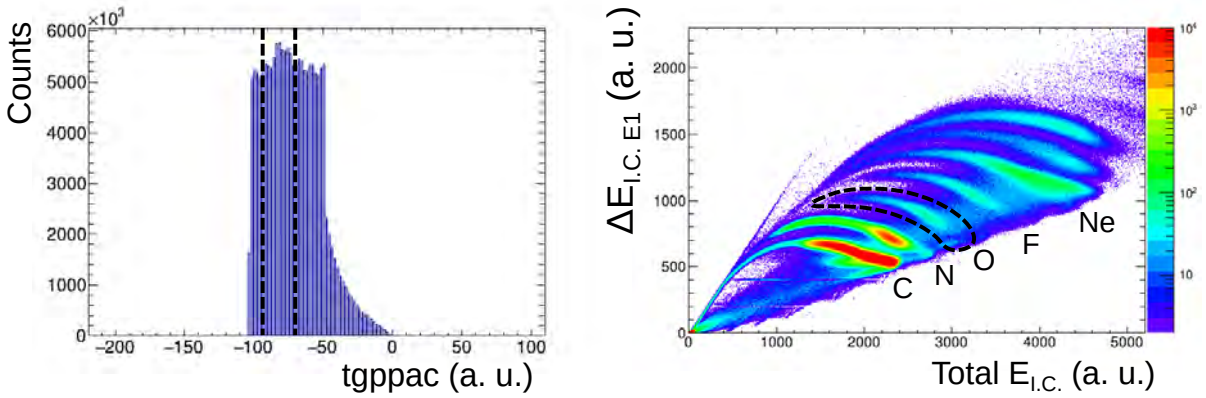

Figure 4.11: The plot on the left shows the gating on the timestamp difference between the PPAC and GRETINA events (tgppac). The right plot displays the energy loss of the recoils passing through the E1 segment of the IC, plotted against the total energy deposited, for the atomic number separation of the outgoing recoils. The gate around the oxygen isotopes is indicated by the dotted black line.

The gates shown in figure 4.11 are on the tgppac (left) and on the recoil atomic number separation in the segmented ionisation chamber (right). The tgppac is defined as the subtraction of the timestamps recorded by the PPAC from the GRETINA timestamps. The time

gating was selected and adjusted to maximise the peak to total ratio of the γ-ray spectrum, via the suppression of the background events. The plot on the right shows the energy loss of the recoils passing through the segment E1 of the IC, see the schematic in figure 4.2, against the total energy deposited in the IC. As was explained in section 4.1.3, the energy loss of the recoils passing through the IC is described by the Bethe formula in equation 2.9, to be proportional to the square of the atomic number. Hence, the recoils are separated according to their Z values. The events that form the straight line that can be observed on the right side of the plot, are known as the punch-throughs. These are where the recoils pass through the active area of the IC without depositing their total energy. The Z-gating to select the oxygen isotopes is denoted by the dotted black line on the plot.

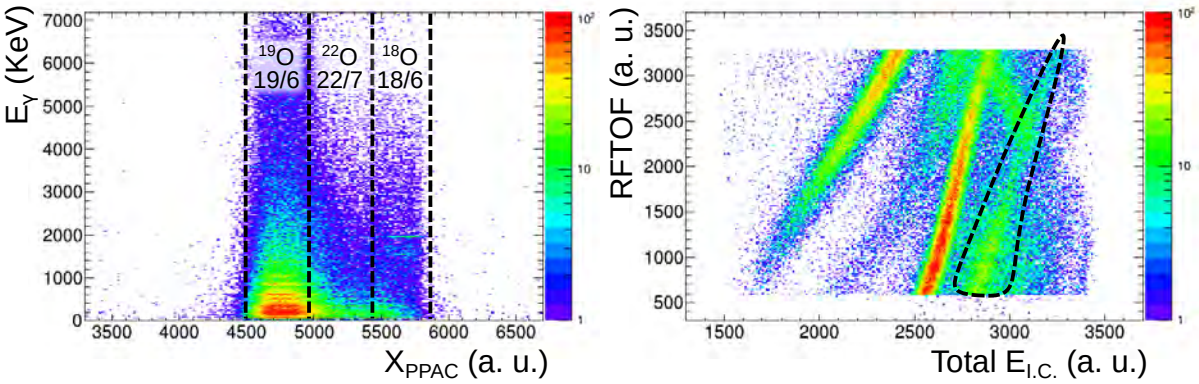

Figure 4.12: On the left, the Doppler corrected γ-ray energies are plotted against the x-positions of the recoils, measured by the PPAC, at the focal plane of the FMA. The separation of the oxygen isotopes according to their A/q is indicated by the regions bounded by the dotted black line. On the right is the gate on the TOF between the PPAC and the RF signal from the accelerator, plotted against the deposited recoil energy in the IC, to remove the more dominant ^{18}O and ^{19}O isotopes, leaking into the ^{22}O gate.

The next gates shown in figure 4.12, aim to separate the oxygen isotopes according their masses. The plot on the left shows the γ-ray energies plotted against the x-positions of the recoils at the focal plane of the FMA, measured by the PPAC. As was discussed in section 4.1.3, the recoils are dispersed at the FMA focal plane according to their mass-to-charge ratios, where the set A_0 and q_0 values are centred, with an increasing A/q to the left of the plot. The general regions of each isotope are denoted by the black dotted lines, with the A/q values labelled. The ^{18}O and ^{19}O recoils, which according to the PACE4 calculations in figure 4.3, have cross sections of approximately three orders of magnitude greater than ^{22}O, can be seen to be "leaking" into the ^{22}O gate. Therefore, an additional gate on the TOF between the PPAC and the RF signal from the accelerator, against the energy deposited in the IC,

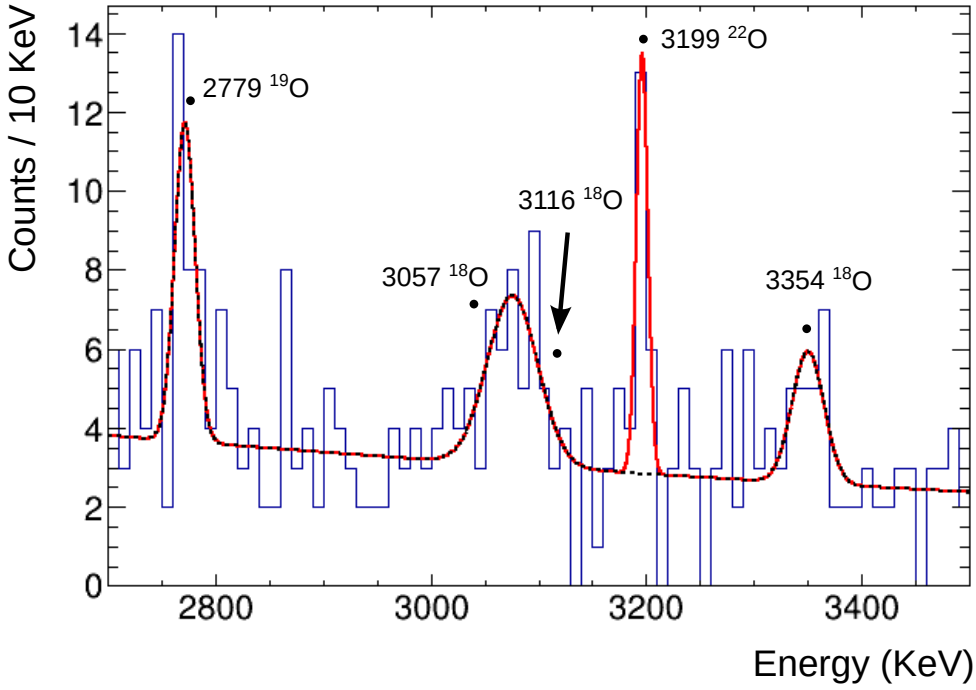

Figure 4.13: Doppler corrected γ-ray spectrum for the ^{22}O recoils, from experimental setting 2. The ^{18}O and ^{19}O γ rays were observed in addition to the potential 3199 keV transition from the 2_1^+ state of ^{22}O, which was fit to a confidence level of 2 σ, with an integral of 14 $\pm$ 5 counts.

was used to remove any ambiguities in the mass arising from overlapping A/q values at the focal plane. The plot of this is shown to the right of figure 4.12, where the gated region is again highlighted by the dotted black line. Using all of the gates discussed here, the Doppler corrected γ-ray spectrum in figure 4.13 was plotted.

The spectrum displayed in figure 4.13 constitutes the best case for the observation of the 3199 keV γ ray, from the 2_1^+ state of ^{22}O, as this structure was not observed in any other setting. Despite the extensive gatings discussed above, the ^{18}O and ^{19}O γ rays can still be observed on the spectrum. However, here they don't entirely wash out the 3199 keV peak, as they did without the gates in figure 4.12. The fitting of the peaks was carried out using the least squared method that was discussed in section 3.2.4, for the fitting of the Gaussian curves to the ^{23}F data. The difference here is that over the larger range, the linear component was replaced with an exponential background with four other Gaussians for the ^{18}O and ^{19}O peaks, to obtain a more complete description of the background.

The peak was observed to have a centroid energy of 3196.5 $\pm$ 2.5 keV, with an integral of 14 $\pm$ 5 and was fit to confidence level of only 2σ. It is therefore difficult to definitively determine whether this structure is indeed the transition from the 2_1^+ state of ^{22}O, or whether

it is due to statistical fluctuations in the background. Regardless of its veracity, the peak had too few statistics for the DSAM measurement, which was the original objective of the experiment.

4.4 Discussion

It is clear from the best-case γ-ray spectrum presented in figure 4.13, that the rates of the 3199 keV γ rays, from the decay of the first excited state of ^{22}O, were significantly lower than first anticipated. Indeed, with the observed statistics it is difficult to verify the authenticity of the peak, let alone perform the DSAM measurement to extract the lifetime of the 2^+ state. There are several possible reasons for the lower than expected statistics; such as the 0.268 mb cross section for the population of ^{22}O, given by the PACE4 codes, being an overestimation, or an insufficient ^{10}Be content in the excitation layer of the target, or simply that the recoils of interest were not accepted by the FMA. The following sections evaluate each of these possibilities, with the implications of the results for the future work being discussed in section 4.4.4.

4.4.1 Target Composition

It was expected after the molecular plating of the target material onto the platinum backing, that the yield of the deposition was low. Activity measurements on target enabled a rough estimation of the deposition yield to be between 30-40%, resulting in an expected ^{10}Be content of approximately 50 μg/cm^2. In order to more accurately quantify the elemental composition of the target, and to gain a clearer understanding of any contaminants in the excitation layer, the target was sent for a Rutherford Backscattering Spectrometry (RBS) measurement.

RBS is a technique that is frequently used for the characterisation of the structures and compositions of materials [140, 141]. By measuring the elastically backscattered ions impinged upon the sample, at a fixed detection angle, the elemental composition and depth distributions of a material can be determined. The elemental make-up of the sample is extracted by measuring the ion energy lost in the backscattering events on the sample nuclei, whilst the depth is inferred from the energy lost as the ion traverses the material, via the ion-electron interactions. Although this technique is able to precisely identify and quantify the sample elements, the chemical structures of the atoms cannot be ascertained.

The RBS measurement was performed by the Dalton Nuclear Institute [142], in which protons accelerated to 2 MeV were impinged upon the 1 μm platinum backing targets used during the experiment, with a detector placed at a fixed scattering angle of 168 degrees. The measurements were performed upon two locations on the target face, the results from which are presented in table 4.2, with estimated uncertainties of between 5-10%. It was found that other light elements, namely ^{12}C, ^{14}N and ^{16}O were unambiguously mixed within the beryllium layer. There were also likely to be small quantities of hydrogen mixed within this layer, however this could not be quantified. Hydrogen cannot be directly measured by such experiments, as they cannot backscatter the incoming ions, so its presence and quantity have to be inferred by the apparent density of the sample.

In addition to the material content, results of the RBS measurement also determined that the excitation layer had a depth of 0.85 ± 0.15 μm in position 1, and a depth of 1.1 ± 0.2 μm in position 2. This is almost double the thickness that would be expected for a solid deposited residue with the amount of material displayed in table 4.2, indicating a lower than expected average density of the deposited material ($\rho_{\text{avg.}}$ = 0.9-1.0 g/cm^3 compared to ρ_{BeO} = 3.02 g/cm^3 or $\rho_{\text{Be(OH)2}}$ = 1.92 g/cm^3). This could be due to the chemical processes involved in the deposition of the target material, or due to an uneven distribution of material, potentially as a consequence of micro-cracking in the surface of the deposited layer. Further work, discussed in section 4.4.4, is required to understand this effect, in order to continue the development of the target.

	^{9}Be (μg/cm^2)	^{10}Be (μg/cm^2)	^{12}C (μg/cm^2)	^{14}N (μg/cm^2)	^{16}O (μg/cm^2)
Pos 1	34.18	22.79	2.53	4.31	24.42
Pos 2	40.27	32.95	2.1	2.43	21.39

Table 4.2: Target composition results from the RBS measurement. The measurement was carried out upon two locations of the target face [143].

The beryllium content from the results of the RBS measurement, shown in table 4.2, confirms the predicted low deposition yield from the molecular plating of the target material onto the platinum substrate. Approximately 20% of the intended material in the solution was deposited onto the platinum backing, with a ^{10}Be enrichment of around 40%. The low ^{10}Be content would have certainly had a negative impact on the rates of the 3199 keV γ rays, from the decay of the ^{22}O recoils. However, the very low rates observed during the experiment, demonstrated in the spectrum in figure 4.13, cannot be solely accounted for by a 20% reduction in target material. As the estimated γ-ray yield in equation 4.1 shows, with an irradiation time of 17.2 hours and beam current of 75 enA in experimental setting

2, a reasonable number of γ rays would be expected to be detected, unless the PACE4 cross sections are incorrect or the recoils acceptance into the FMA is particularly low.

$$\text{Yield} = \frac{I}{Ze10^{11}} \frac{xN_A}{M} \sigma T \varepsilon_\alpha \varepsilon_\gamma \tag{4.1}$$

Where I is the beam current in enA and Z is the atomic number of the ion beam, x is the target material thickness in μg/cm^2, M is the molar mass of the target material and N_A is Avogadro's constant. The reaction cross section is denoted by σ in m^2 and the irradiation time in seconds by T. The ε_γ parameter represents the γ-ray detection efficiency and ε_α is the acceptance of the recoil of interest into the FMA.

To understand the origin of the low statistics of the 3199 keV γ ray, and to evaluate the possibilities of an overestimation of the cross sections by PACE4, or a low recoil acceptance into the FMA, it useful to survey at some of the other isotopes that were strongly populated in the fusion-evaporation reactions.

4.4.2 ^{22}Ne Discussion

The ^{22}Ne isotope was a good starting point for the investigation into the low rates, as it constitutes the dominant reaction recoil at the focal plane of the FMA, and is strongly populated by a variety of different reaction pathways available to the setup, see table 4.3. The ^{22}Ne data that is discussed in this section, was also observed in experimental setting 2, the same setting as the best-case ^{22}O γ-ray spectrum in figure 4.13. As the beam current, irradiation time and target are the same, comparisons between the cross sections and measured statistics of the ^{22}O and ^{22}Ne recoils can be made to deduce the reason for the observed low rates of the ^{22}O γ rays.

PACE4 ^{22}Ne cross sections (mb)					
Projectile	Target				
	^{9}Be	^{10}Be	^{12}C	^{14}N	^{16}O
^{14}C	2.42	96.7	56.8	96.6	43.1
^{14}N	-	32.95	-	2.43	-

Table 4.3: Reaction pathways and cross sections calculated using PACE4, for the population of the ^{22}Ne recoils.

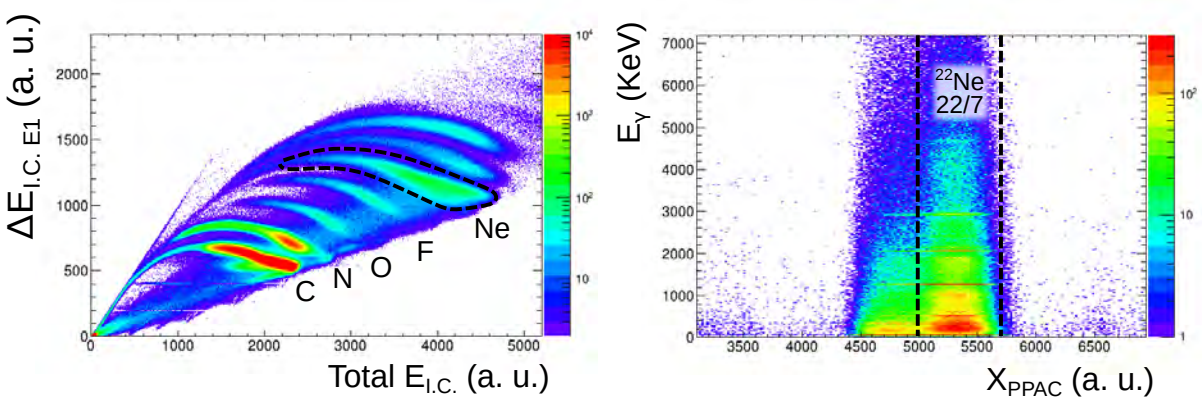

Figure 4.14: On the left, the atomic number gate for the neon isotopes is highlighted by the dotted black line, which are separated by the energy loss characteristics of the recoils in the IC. On the right is the gate on the A/q dispersion of the recoils, measured by the PPAC. As is displayed on the plot, the ^{22}Ne dominated the focal plane of the FMA so no other gates were required.

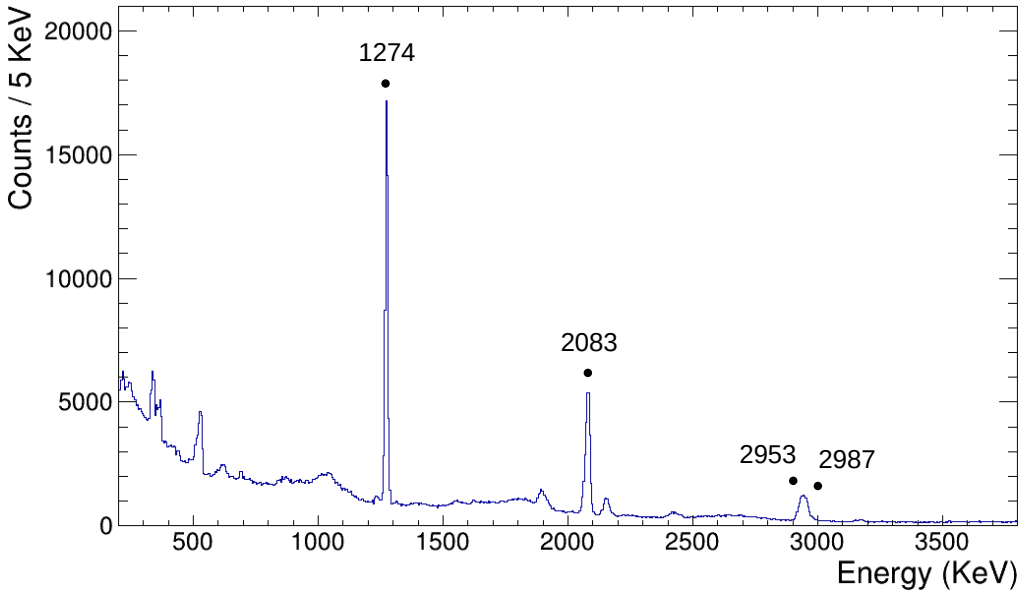

Figure 4.15: Doppler corrected ^{22}Ne γ-ray spectrum.

The PID plots for the ^{22}Ne recoils are illustrated in figure 4.14, where the gates used are denoted by the dotted black lines. The plot on the left again displays the energy loss profiles of the recoils passing through the IC, for the atomic number separation, whilst the plot on the right shows the transmitted recoils, separted by their mass-to-charge ratios at the focal plane of the FMA. As the ^{22}Ne was the dominant isotope at the focal plane, with total cross sections several orders of magnitude greater than other neon isotopes, further gates on the RFTOF were not required to resolve any A/q overlaps, as was the case for the ^{22}O. The Doppler corrected γ-ray spectrum for ^{22}Ne is displayed in figure 4.15.

Despite being the isotope with the strongest population in the experimental setting, the statistics observed on the ^{22}Ne γ-ray spectrum in figure 4.15, were significantly below what was anticipated. Calculating the expected γ-ray yield, using equation 4.1, with the parameters of the experimental setting in table 4.1 and reaction cross section in table 4.3, it is clear that only a fraction of the expected γ rays were being detected. As ^{22}Ne is populated via multiple reaction pathways, to account for the difference between the expected and observed γ-ray statistics, the PACE4 calculations would have to systematically overestimate the cross sections for each of the reactions, by several orders of magnitude. Thus, this indicates that the low rates that were observed during the experiment, were in fact due to low recoil acceptances into the FMA.

To understand the apparent low acceptances, the Monte Carlo PACE4 codes were used to calculate the kinematics of the outgoing recoils. The energy and angular distributions of the ^{22}Ne recoils, from the dominant two-neutron exit channel of the fusion-evaporation reaction of ^{14}C on ^{10}Be, are plotted in figure 4.16. The plot demonstrates that the recoils have the greatest chance of emission at an angle of approximately 7 degrees, with respect to the incoming ^{14}C beam direction, falling rapidly towards the smaller angles. This can be understood as both neutrons needing to be emitted in such a way that any momentum components perpendicular to the direction of the beam are cancelled out, for the ^{22}Ne recoils to not be significantly deflected. Clearly this is quite rare, as just over 1% of the outgoing recoils have an angle under 1 degree. These calculated angular distributions, coupled with a nominal FMA acceptance of 8 msr, indicate a particularly low recoil acceptance.

Using the PACE4 cross sections summarised in table 4.3, the target material content in table 4.2 and accounting for the estimated 10% ^{14}N beam contaminant, the ^{22}Ne should be produced, via all of the reactions, approximately 575 times greater than the ^{22}O in the experimental same setting. After correcting for the detection efficiency of the ^{22}Ne γ rays in figure 4.15, and the absolute efficiency of the expected 3199 keV γ ray of 4.5%, via measurement of the ^{56}Co source, simply scaling the measured statistics by the cross sections suggests there should only be 90 γ rays at 3199 keV from the 2_1^+ state of ^{22}O, on the spectrum in figure 4.13. Of course this is not a perfect comparison as the ^{22}Ne had less restrictive and fewer gates than the ^{22}O, as it dominated the other neon isotopes at the FMA focal plane. It was also populated via several reactions, each with different recoil angular distributions, and therefore different acceptances into the FMA. However despite this, the comparison does illustrate the low expected yields when taking the low acceptances into account, and provides some insight into the limiting factor of the experiment.

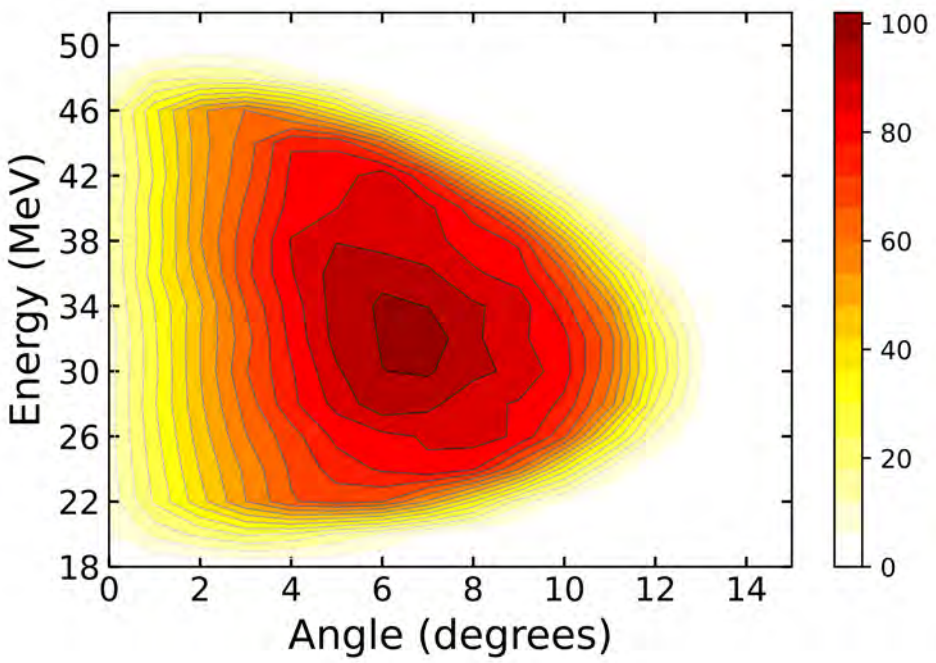

Figure 4.16: Kinematics of the ^{22}Ne recoils populated by the two-neutron exit channel of the fusion-evaporation reaction of a ^{14}C beam on a ^{10}Be target, calculated using PACE4. The energy and angular distributions of the recoils are expressed as a fraction of the maximum values at 7 degrees with 32 MeV.

4.4.3 ^{21}O Discussion

An additional useful isotope to investigate the apparent low acceptance of the recoils into the FMA is ^{21}O. The ^{21}O data that is discussed in this section was populated exclusively via the two-proton exit channel of the fusion-evaporation reaction of the ^{14}C beam on the ^{9}Be, in experimental setting 3, where the novel ^{10}Be target was replaced by a 100 μg/cm^2 pure ^{9}Be target. As the reactions to populate the ^{21}O and ^{22}O are the same, just on different beryllium isotopes, the data can be directly compared to deduce the recoil acceptance and expected statistics of the ^{22}O γ rays.

The PID plots and the gates to tag onto the ^{21}O recoils in experimental setting 3 are shown in figures 4.17 and 4.18. The atomic number separation via the recoil energy loss through the IC is displayed in figure 4.17, and the recoil dispersion measured by the PPAC is presented on the left of figure 4.18. As is demonstrated on the plot, there is a direct A/q overlap of the ^{21}O recoils with the ^{18}O, which have calculated cross sections of 1.61 mb and 151 mb respectively. Therefore to resolve this overlap, an additional gate on the RFTOF against the total energy deposited in the IC is once again required, illustrated on the right. The Doppler corrected ^{21}O γ-ray spectrum is displayed in figure 4.19.

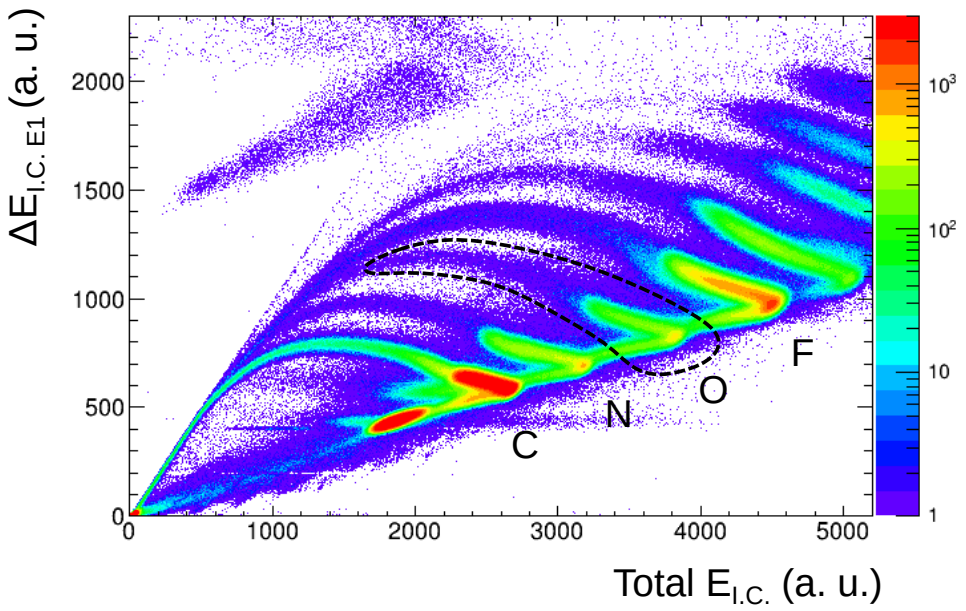

Figure 4.17: The atomic number gate for the ^{21}O recoils is indicated by the dotted black line, for experimental setting 3 in table 4.1, with the ^{9}Be target.

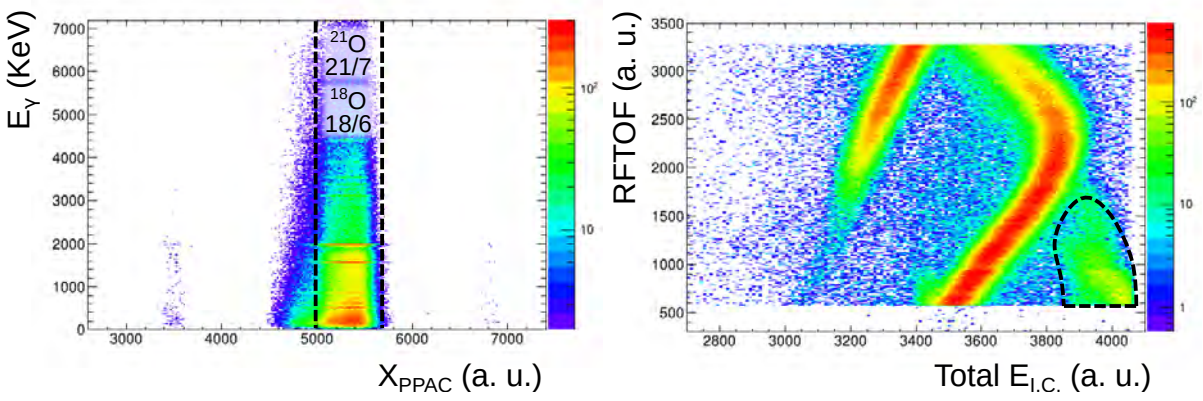

Figure 4.18: The mass gates for the ^{21}O recoils, indicated by the dotted black lines. The plot on the left demonstrates the A/q overlap of the ^{18}O and ^{21}O recoils at the focal plane of the FMA, so that the gate on the RFTOF, right plot, is required to separate the two.

The ^{21}O γ-ray spectrum shown in figure 4.19 once again displays fewer statistics than would be expected from the parameters of the experimental setting, shown in table 4.1. By comparing the efficiency corrected measured statistics to the expected yield from equation 4.1, the acceptance of the ^{21}O recoils was deduced to be 0.01%, assuming that the PACE4 cross section of 1.61 mb is correct. This low acceptance can again be understood using the recoil kinematics illustrated in figure 4.20. The recoils have the greatest chance of emission at an angle of 3 degrees, which decreases rapidly towards the smaller angles to just 3% of

the recoils emitted an angle of 1 degree or under, relative to the incoming beam direction.

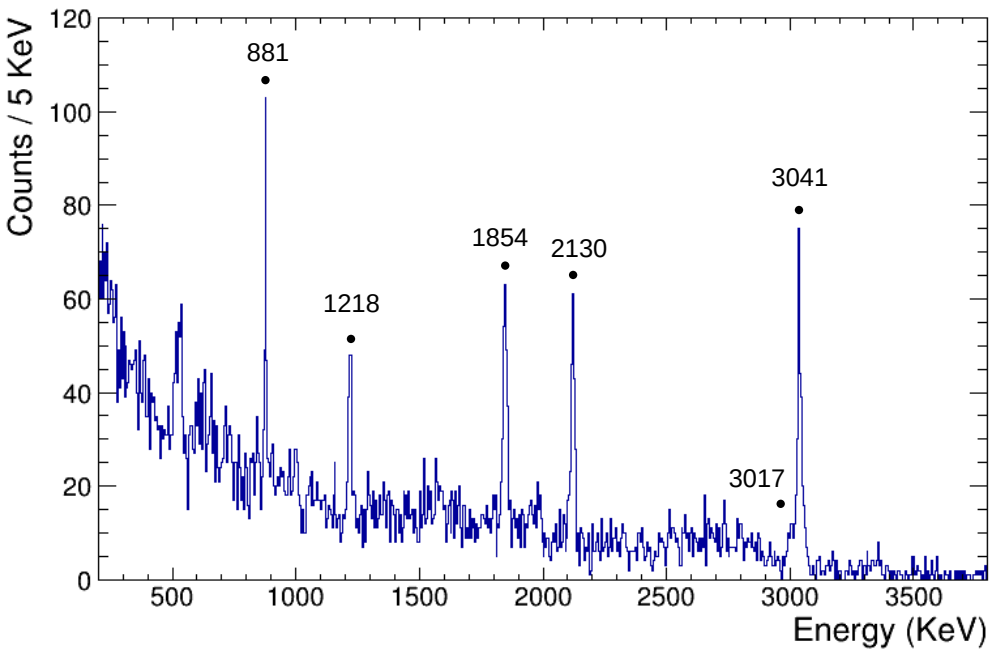

Figure 4.19: Doppler corrected ^{21}O γ-ray spectrum.

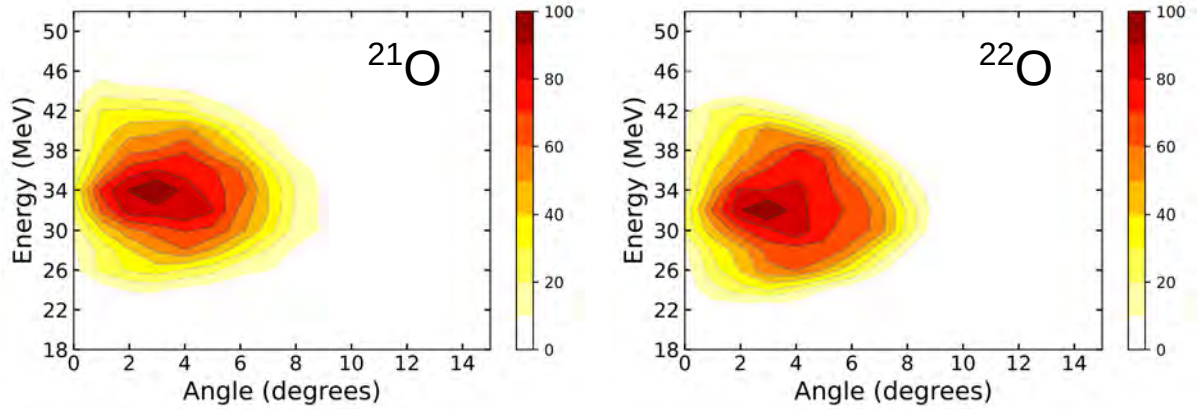

Figure 4.20: Comparison of the kinematics of the ^{21}O and ^{22}O recoils, populated by the two-proton exit channels of the fusion-evaporation reactions of a ^{14}C beam on a ^{9}Be and ^{10}Be target respectively, calculated using PACE4.

As the reactions to populate the ^{21}O and ^{22}O are essentially identical, barring the beryllium isotopes, with similar recoil energy and angular distributions shown in figure 4.20, the ^{22}O acceptance was assumed to be comparable to that of the ^{21}O. Thus, calculating the estimated yield of the 3199 keV γ rays from ^{22}O, with the parameters in table 4.1, an acceptance of 0.01%, a cross section of 0.268 mb and accounting for the detection efficiencies, results in an expected peak of 15 γ rays. This result appears to corroborate with the 14 $\pm$ 5 count peak structure that was fit in figure 4.13, in addition to demonstrating that the origin of the

observed low rates during the experiment, can be attributed to the low recoil acceptance into the FMA.

4.4.4 Future Work

The development of a novel ^{10}Be target to probe the nuclear structure of ^{22}O, was an ambitious project with a number of challenges that have yet to be overcome. The work that has been presented within this chapter of the thesis, has laid the groundwork for the future developments of a radioactive ^{10}Be target, that could improve the experimental accessibility to the light neutron-rich region of the nuclear chart. The successful development and characterisation of such a target could have applications within both nuclear astrophysics experiments as well as other high-precision nuclear structure measurements.

It is clear from the RBS results, that the production of the ^{10}Be target on the platinum backing saw some limited success, albeit with a lower than desired deposition yield. For the future developments of the target, the molecular plating procedure should be refined to optimise the deposition parameters, including the type of solvent, deposition time and current, to achieve higher yields. Additionally, specialist characterisation techniques such as scanning electron microscopy (SEM) or atomic force microscopy (AFM) should be employed, to characterise the surface structure of the target. With the material content data from the RBS, this would enable a more complete understanding of the deposition process, to guide the development of a radioactive ^{10}Be target, that is suitable for high-precision nuclear physics experiments.

In regards to the future iterations of the experiment to measure the lifetime of the 2_1^+ state of ^{22}O via DSAM, a target with a greater ^{10}Be content would clearly be beneficial. However, as has been discussed in the previous sections, the limiting factor for the measurement was the acceptance of the recoils into the FMA. Therefore, any future experiment should seek to address this issue as a priority. The simplest solution would be to shift the target downstream, to be closer to the entrance to the FMA, to improve acceptance, whilst also improving the effectiveness of the DSAM by increasing the γ-ray detection angles. The FMA could also be turned about 3 degrees relative to the beam direction, to cover the peak angular range of the ^{22}O. Otherwise, a different direction for the recoil separation would need to be taken, such as by using ringed silicon detectors placed downstream of the target, to exploit the different angles with which the recoils are emitted.

4.4.5 Summary

In summary, a novel ^{10}Be target was developed to populate the excited ^{22}O recoils, via the two-proton exit channel of the fusion-evaporation reaction of a ^{14}C beam on a ^{10}Be target. The preparation of the target was a partial success, with the Rutherford Backscattering Spectrometry measurement demonstrating the deposition of the ^{10}Be target material onto the platinum backings, albeit with a lower than desired yield and an unknown surface structure. Further work is require to improve the yield of the molecular plating deposition and to fully characterise the distribution and structure of the deposited material.

The experiment to measure the electromagnetic transition rates in ^{22}O was carried out at ANL, using the tracking detector array GRETINA, coupled to the FMA. Several experimental settings, with a range of ^{14}C beam energies, were used in order to find the optimum parameters for the production and acceptance of the ^{22}O recoils. A candidate 3199 keV peak structure was observed on the Doppler corrected γ-ray spectrum, in a single experimental setting, to have an integral of 14 ± 5 counts and was fitted to a confidence level of 2σ. Thus, this structure was too weak for the DSAM measurement. Through the analysis of the ^{21}O and ^{22}Ne recoils, which were populated via the other channels in the fusion-evaporation reaction, it was inferred that the low rates of the ^{22}O could be primarily attributed to the low recoil acceptance into the FMA.

Chapter 5

Conclusion

The first part of this thesis presented work on the measurement of the nuclear structure of the light neutron-rich ^{23}F nucleus, following a one-neutron removal reaction. The high-resolution Doppler corrected γ-ray spectrum, measured by the state-of-the-art tracking γ-ray detector array, GRETINA, with the available high statistics, enabled the observation of several new γ-ray transitions and the identification of two new excited states. Additionally, three of the measured excited states were observed for the first time to be populated in the one-neutron removal reaction, including the $s_{1/2}$ and $d_{3/2}$ single-particle proton states of 2241 keV and 4065 keV, respectively. The apparent direct population to these states could be indicative of unobserved feeding transitions, or suggests a more mixed nature for these states, with a non-negligible neutron contribution. Further investigations of the structure of ^{23}F following a proton transfer or knockout reaction, using GRETINA, could shed more light on the nature of these states.

The γ-γ coincidence analysis enabled the construction of an extended level scheme for ^{23}F. The relative intensities of the transitions, relative population and branching ratios, many of which were predicted by theory but were experimentally unobserved, were measured through the fitting of detailed Monte Carlo GEANT4 simulations to the γ-ray spectrum. Furthermore, the spins and parities of the excited states were assigned by analysing the angular distributions of the γ-ray transition. Through the evaluation of the root mean square of the measurements and theoretical predictions, it was shown that the calculations using the USDB Hamiltonian were the most consistent with the experimental data, on the structure of ^{23}F.

The second part of this thesis was primarily focused on the experiment to measure the electromagnetic transition rates in ^{22}O. The measurement necessitated the development of a novel ^{10}Be target on a thin platinum backing, for the population of the excited ^{22}O recoils

via the ^{14}C(^{10}Be,2p)^{22}O reaction. The target was successfully prepared using the molecular plating technique, however a low deposition yield of about 20% significantly reduced the ^{10}Be content to be between 22-32 μg/cm^2. Further work on the target preparation procedure is required in order to to improve the deposition yield and produce thicker targets. Furthermore, through the use of precision characterisation techniques such as SEM or AFM, the surface structure of the deposited layer could be analysed. This would assist in the development of a more robust procedure for the preparation of a radioactive ^{10}Be target, that is suitable for high-precision nuclear physics measurements.

In the experiment to measure the electromagnetic transition rates in ^{22}O, GRETINA was coupled to the FMA at ANL, for the identification and separation of the outgoing recoils. Several ^{14}C beam energies were scanned across during the course of the experiment, to search for the optimum parameters for the production of the ^{22}O recoils. A candidate 3199 keV peak was observed in a single experimental setting, which was measured to have an integral of 14 ± 5 counts and fit to a confidence level of 2σ. The analysis of the stronger exit channels of the fusion-evaporation reaction, namely ^{21}O and ^{22}Ne, suggested that the low rates of the ^{22}O recoils could be primarily attributed to the low acceptance into the FMA. Therefore, the most obvious adjustments for future iterations of the experiment would be to improve the ^{22}O recoil acceptance into the FMA. This could be achieved by shifting the target downstream and rotating the FMA to be approximately 3 degrees relative to the beam axis direction, to cover the peak angles. This change alongside a thicker ^{10}Be target, would result in the larger yield and acceptance of ^{22}O recoils, so that the DSAM measurement of the lifetime of the first 2^+ state could be performed.

Bibliography

[1] E. Rutherford, "The scattering of and particles by matter and the structure of the atom," *Philosophical Magazine*, vol. 6, no. 21, pp. 669–688, 1911.

[2] N. R. Council *et al.*, *Nuclear physics: exploring the heart of matter*. National Academies Press, 2013.

[3] C. F. v. Weizsäcker, "On the theory of nuclear masses," *Journal of Physics*, vol. 96, pp. 431–458, 1935.

[4] M. Wang, W. Huang, F. G. Kondev, G. Audi, and S. Naimi, "The ame 2020 atomic mass evaluation (ii). tables, graphs and references," *Chinese Physics C*, vol. 45, no. 3, p. 030003, 2021.

[5] K. S. Krane, *Introductory nuclear physics*. John Wiley & Sons, 1991.

[6] R. D. Woods and D. S. Saxon, "Diffuse surface optical model for nucleon-nuclei scattering," *Physical Review*, vol. 95, no. 2, p. 577, 1954.

[7] M. Goeppert-Mayer, "On closed shells in nuclei," *Phys. Rev*, vol. 74, no. 1, pp. 235–239, 1948.

[8] O. Haxel, J. H. D. Jensen, and H. E. Suess, "On the" magic numbers" in nuclear structure," *Physical Review*, vol. 75, no. 11, p. 1766, 1949.

[9] O. Sorlin and M.-G. Porquet, "Nuclear magic numbers: New features far from stability," *Progress in Particle and Nuclear Physics*, vol. 61, no. 2, pp. 602–673, 2008.

[10] C. A. Bertulani, "Nuclear physics in a nutshell," in *Nuclear Physics in a Nutshell*. Princeton University Press, 2007.

[11] B. Wildenthal, "Empirical strengths of spin operators in nuclei," *Progress in particle and nuclear physics*, vol. 11, pp. 5–51, 1984.

[12] B. A. Brown and B. Wildenthal, "Status of the nuclear shell model," *Annual Review of Nuclear and Particle Science*, vol. 38, no. 1, pp. 29–66, 1988.

[13] B. A. Brown and W. Richter, "New "usd" hamiltonians for the sd shell," *Physical Review C*, vol. 74, no. 3, p. 034315, 2006.

[14] W. Richter, S. Mkhize, and B. A. Brown, “sd-shell observables for the usda and usdb hamiltonians,” *Physical Review C*, vol. 78, no. 6, p. 064302, 2008.

[15] A. Magilligan and B. A. Brown, “New isospin-breaking "USD" Hamiltonians for the sd shell,” *Physical Review C*, vol. 101, no. 6, pp. 1–15, 2020.

[16] E. Epelbaum, “Few-nucleon forces and systems in chiral effective field theory,” *Progress in Particle and Nuclear Physics*, vol. 57, no. 2, pp. 654–741, 2006.

[17] E. Epelbaum, H. W. Hammer, and U. G. Meißner, “Modern theory of nuclear forces,” *Reviews of Modern Physics*, vol. 81, no. 4, pp. 1773–1825, 2009.

[18] S. Weinberg, “Effective chiral lagrangians for nucleon-pion interactions and nuclear forces,” *Nuclear Physics B*, vol. 363, no. 1, pp. 3–18, 1991.

[19] H. Hergert, “A Guided Tour of ab initio Nuclear Many-Body Theory,” *Frontiers in Physics*, vol. 8, 2020.

[20] R. Machleidt and D. R. Entem, “Chiral effective field theory and nuclear forces,” *Physics Reports*, vol. 503, no. 1, pp. 1–75, 2011. [Online]. Available: http://dx.doi.org/10.1016/j.physrep.2011.02.001

[21] P. Navrátil, S. Quaglioni, G. Hupin, C. Romero-Redondo, and A. Calci, “Unified ab initio approaches to nuclear structure and reactions,” *Physica Scripta*, vol. 91, no. 5, 2016.

[22] H. Hergert, S. Bogner, T. Morris, A. Schwenk, and K. Tsukiyama, “The in-medium similarity renormalization group: A novel ab initio method for nuclei,” *Physics reports*, vol. 621, pp. 165–222, 2016.

[23] V. Somà, “Self-consistent green’s function theory for atomic nuclei,” *Frontiers in Physics*, vol. 8, p. 340, 2020.

[24] G. Hagen, T. Papenbrock, M. Hjorth-Jensen, and D. J. Dean, “Coupled-cluster computations of atomic nuclei,” *Reports on Progress in Physics*, vol. 77, no. 9, p. 096302, 2014.

[25] B. R. Barrett, P. Navrátil, and J. P. Vary, “Ab initio no core shell model,” *Progress in Particle and Nuclear Physics*, vol. 69, pp. 131–181, 2013.

[26] T. Motobayashi, Y. Ikeda, K. Ieki, M. Inoue, N. Iwasa, T. Kikuchi, M. Kurokawa, S. Moriya, S. Ogawa, H. Murakami, S. Shimoura, Y. Yanagisawa, T. Nakamura, Y. Watanabe, M. Ishihara, T. Teranishi, H. Okuno, and R. Casten, “Large deformation of the very neutron-rich nucleus 32mg from intermediate-energy coulomb excitation,” *Physics Letters B*, vol. 346, no. 1, pp. 9–14, 1995. [Online]. Available: https://www.sciencedirect.com/science/article/pii/037026939500012A

[27] N. Fukunishi, T. Otsuka, and T. Sebe, "Vanishing of the shell gap in n = 20 neutron-rich nuclei," *Physics Letters B*, vol. 296, no. 3, pp. 279–284, 1992. [Online]. Available: https://www.sciencedirect.com/science/article/pii/0370269392913209

[28] C. Thibault, R. Klapisch, C. Rigaud, A. Poskanzer, R. Prieels, L. Lessard, and W. Reisdorf, "Direct measurement of the masses of li 11 and na 2 6- 3 2 with an on-line mass spectrometer," *Physical Review C*, vol. 12, no. 2, p. 644, 1975.

[29] C. Détraz, D. Guillemaud, G. Huber, R. Klapisch, M. Langevin, F. Naulin, C. Thibault, L. Carraz, and F. Touchard, "Beta decay of na 2 7- 3 2 and their descendants," *Physical Review C*, vol. 19, no. 1, p. 164, 1979.

[30] G. Huber, F. Touchard, S. Büttgenbach, C. Thibault, R. Klapisch, H. Duong, S. Liberman, J. Pinard, J. Vialle, P. Juncar *et al.*, "Spins, magnetic moments, and isotope shifts of na 2 1-3 1 by high resolution laser spectroscopy of the atomic d 1 line," *Physical Review C*, vol. 18, no. 5, p. 2342, 1978.

[31] B. Bastin, S. Grévy, D. Sohler, O. Sorlin, Z. Dombrádi, N. Achouri, J. Angélique, F. Azaiez, D. Baiborodin, R. Borcea *et al.*, "Collapse of the n= 28 shell closure in s 42 i," *Physical review letters*, vol. 99, no. 2, p. 022503, 2007.

[32] C. Campbell, N. Aoi, D. Bazin, M. Bowen, B. A. Brown, J. Cook, D.-C. Dinca, A. Gade, T. Glasmacher, M. Horoi *et al.*, "Measurement of excited states in si 40 and evidence for weakening of the n= 28 shell gap," *Physical review letters*, vol. 97, no. 11, p. 112501, 2006.

[33] D. Sohler, Z. Dombradi, J. Timár, O. Sorlin, F. Azaiez, F. Amorini, M. Belleguic, C. Bourgeois, C. Donzaud, J. Duprat *et al.*, "Shape evolution in heavy sulfur isotopes and erosion of the n= 28 shell closure," *Physical Review C*, vol. 66, no. 5, p. 054302, 2002.

[34] M. Stanoiu, F. Azaiez, Z. Dombrádi, O. Sorlin, B. Brown, M. Belleguic, D. Sohler, M. Saint Laurent, M. Lopez-Jimenez, Y. Penionzhkevich *et al.*, "N= 14 and 16 shell gaps in neutron-rich oxygen isotopes," *Physical Review C*, vol. 69, no. 3, p. 034312, 2004.

[35] C. Hoffman, T. Baumann, D. Bazin, J. Brown, G. Christian, P. A. DeYoung, J. Finck, N. Frank, J. Hinnefeld, R. Howes *et al.*, "Determination of the n= 16 shell closure at the oxygen drip line," *Physical Review Letters*, vol. 100, no. 15, p. 152502, 2008.

[36] A. Huck, G. Klotz, A. Knipper, C. Miehé, C. Richard-Serre, G. Walter, A. Poves, H. Ravn, and G. Marguier, "Beta decay of the new isotopes k 52, ca 52, and sc 52; a test of the shell model far from stability," *Physical Review C*, vol. 31, no. 6, p. 2226, 1985.

[37] D. Steppenbeck, S. Takeuchi, N. Aoi, P. Doornenbal, M. Matsushita, H. Wang, H. Baba, N. Fukuda, S. Go, M. Honma *et al.*, "Evidence for a new nuclear 'magic number'from the level structure of 54ca," *Nature*, vol. 502, no. 7470, pp. 207–210, 2013.

[38] E. Caurier, G. Martínez-Pinedo, F. Nowacki, A. Poves, and A. Zuker, "The shell model as a unified view of nuclear structure," *Reviews of modern Physics*, vol. 77, no. 2, p. 427, 2005.

[39] D. S. Ahn, N. Fukuda, H. Geissel, N. Inabe, N. Iwasa, T. Kubo, K. Kusaka, D. J. Morrissey, D. Murai, T. Nakamura, M. Ohtake, H. Otsu, H. Sato, B. M. Sherrill, Y. Shimizu, H. Suzuki, H. Takeda, O. B. Tarasov, H. Ueno, Y. Yanagisawa, and K. Yoshida, "Location of the Neutron Dripline at Fluorine and Neon," *Physical Review Letters*, vol. 123, no. 21, p. 212501, 2019. [Online]. Available: https://doi.org/10.1103/PhysRevLett.123.212501

[40] T. Frederico, A. Delfino, L. Tomio, and M. T. Yamashita, "Universal aspects of light halo nuclei," *Progress in Particle and Nuclear Physics*, vol. 67, no. 4, pp. 939–994, 2012.

[41] I. Tanihata, "Neutron halo nuclei," *Journal of Physics G: Nuclear and Particle Physics*, vol. 22, no. 2, p. 157, 1996.

[42] Z. Kohley, T. Baumann, D. Bazin, G. Christian, P. A. DeYoung, J. Finck, N. Frank, M. Jones, E. Lunderberg, B. Luther *et al.*, "Study of two-neutron radioactivity in the decay of o 26," *Physical review letters*, vol. 110, no. 15, p. 152501, 2013.

[43] L. Grigorenko, I. Mukha, and M. V. Zhukov, "Lifetime and fragment correlations for the two-neutron decay of o 26 ground state," *Physical review letters*, vol. 111, no. 4, p. 042501, 2013.

[44] K. Hagino and H. Sagawa, "Correlated two-neutron emission in the decay of the unbound nucleus 26 o," *Physical Review C*, vol. 89, no. 1, p. 014331, 2014.

[45] B. A. Brown, "The oxygen isotopes," *International Journal of Modern Physics E*, vol. 26, no. 01n02, p. 1740003, 2017.

[46] W.-T. Chou, E. Warburton, and B. A. Brown, "Gamow-teller beta-decay rates for a 18 nuclei," *Physical Review C*, vol. 47, no. 1, p. 163, 1993.

[47] M. Langevin, E. Quiniou, M. Bernas, J. Galin, J. Jacmart, F. Naulin, F. Pougheon, R. Anne, C. Détraz, D. Guerreau *et al.*, "Production of neutron-rich nuclei at the limits of particles stability by fragmentation of 44 mevu 40ar projectiles," *Physics Letters B*, vol. 150, no. 1-3, pp. 71–74, 1985.

[48] T. Otsuka, T. Suzuki, J. D. Holt, A. Schwenk, and Y. Akaishi, "Three-body forces and the limit of oxygen isotopes," *Physical Review Letters*, vol. 105, no. 3, pp. 14–17, 2010.

[49] H. Hergert, S. Bogner, S. Binder, A. Calci, J. Langhammer, R. Roth, and A. Schwenk, "In-medium similarity renormalization group with chiral two-plus three-nucleon interactions," *Physical Review C*, vol. 87, no. 3, p. 034307, 2013.

[50] A. Cipollone, C. Barbieri, and P. Navrátil, "Isotopic chains around oxygen from evolved chiral two-and three-nucleon interactions," *Physical Review Letters*, vol. 111, no. 6, p. 062501, 2013.

[51] K. Hebeler, J. D. Holt, J. Menéndez, and A. Schwenk, "Nuclear Forces and Their Impact on Neutron-Rich Nuclei and Neutron-Rich Matter," *Annual Review of Nuclear and Particle Science*, vol. 65, no. 1, pp. 457–484, 2015.

[52] S. Bogner, H. Hergert, J. Holt, A. Schwenk, S. Binder, A. Calci, J. Langhammer, and R. Roth, "Nonperturbative shell-model interactions from the in-medium similarity renormalization group," *Physical Review Letters*, vol. 113, no. 14, p. 142501, 2014.

[53] G. Jansen, J. Engel, G. Hagen, P. Navratil, and A. Signoracci, "Ab initio coupled-cluster effective interactions for the shell model: Application to neutron-rich oxygen and carbon isotopes," *Physical Review Letters*, vol. 113, no. 14, p. 142502, 2014.

[54] J. Holt, J. Menéndez, and A. Schwenk, "Chiral three-nucleon forces and bound excited states in neutron-rich oxygen isotopes," *The European Physical Journal A*, vol. 49, no. 3, pp. 1–6, 2013.

[55] S. Heil, M. Petri, K. Vobig, D. Bazin, J. Belarge, P. Bender, B. A. Brown, R. Elder, B. Elman, A. Gade, T. Haylett, J. D. Holt, T. Hüther, A. Hufnagel, H. Iwasaki, N. Kobayashi, C. Loelius, B. Longfellow, E. Lunderberg, M. Mathy, J. Menéndez, S. Paschalis, R. Roth, A. Schwenk, J. Simonis, I. Syndikus, D. Weisshaar, and K. Whitmore, "Electromagnetic properties of 21O for benchmarking nuclear Hamiltonians," *Physics Letters, Section B: Nuclear, Elementary Particle and High-Energy Physics*, vol. 809, pp. 1–2, 2020.

[56] P. G. Thirolf, B. V. Pritychenko, B. A. Brown, P. D. Cottle, M. Chromik, T. Glasmacher, G. Hackman, R. W. Ibbotson, K. W. Kemper, T. Otsuka, L. A. Riley, and H. Scheit, "Spectroscopy of the 2 1/ + state in 22O and shell structure near the neutron drip line," *Physics Letters, Section B: Nuclear, Elementary Particle and High-Energy Physics*, vol. 485, no. 1-3, pp. 16–22, 2000.

[57] A. N. Bohr and B. R. Mottelson, *Nuclear Structure (in 2 volumes)*. World Scientific Publishing Company, 1998.

[58] G. F. Knoll, *Radiation detection and measurement*. John Wiley & Sons, 2010.

[59] J. F. Ziegler, M. D. Ziegler, and J. P. Biersack, "SRIM - The stopping and range of ions in matter (2010)," *Nuclear Instruments and Methods in Physics Research, Section B: Beam Interactions with Materials and Atoms*, vol. 268, no. 11-12, pp. 1818–1823, 2010. [Online]. Available: http://dx.doi.org/10.1016/j.nimb.2010.02.091

[60] NIST XCOM Photon Attenuation Database. [Online]. Available: https://physics.nist.gov/PhysRefData/Xcom/html/xcom1.html

[61] O. Klein and Y. Nishina, "The scattering of light by free electrons according to dirac's new relativistic dynamics," *Nature*, vol. 122, no. 3072, pp. 398–399, 1928.

[62] H. J. Wollersheim, D. E. Appelbe, A. Banu, R. Bassini, T. Beck, F. Becker, P. Bednarczyk, K. H. Behr, M. A. Bentley, G. Benzoni, C. Boiano, U. Bonnes, A. Bracco, S. Brambilla, A. Brünle,

A. Bürger, K. Burkard, P. A. Butler, F. Camera, D. Curien, J. Devin, P. Doornenbal, C. Fahlander, K. Fayz, H. Geissel, J. Gerl, M. Górska, H. Grawe, J. Grbosz, R. Griffiths, G. Hammond, M. Hellström, J. Hoffmann, H. Hübel, J. Jolie, J. V. Kalben, M. Kmiecik, I. Kojouharov, R. Kulessa, N. Kurz, I. Lazarus, J. Li, J. Leske, R. Lozeva, A. Maj, S. Mandal, W. Mczyński, B. Million, G. Münzenberg, S. Muralithar, M. Mutterer, P. J. Nolan, G. Neyens, J. Nyberg, W. Prokopowicz, V. F. Pucknell, P. Reiter, D. Rudolph, N. Saito, T. R. Saito, D. Seddon, H. Schaffner, J. Simpson, K. H. Speidel, J. Styczeń, K. Sümmerer, N. Warr, H. Weick, C. Wheldon, O. Wieland, M. Winkler, and M. Zibliński, "Rare ISotopes INvestigation at GSI (RISING) using gamma-ray spectroscopy at relativistic energies," *Nuclear Instruments and Methods in Physics Research, Section A: Accelerators, Spectrometers, Detectors and Associated Equipment*, vol. 537, no. 3, pp. 637–657, 2005.

[63] P. Doornenbal, P. Reiter, H. Grawe, T. Saito, A. Al-Khatib, A. Banu, T. Beck, F. Becker, P. Bednarczyk, G. Benzoni, A. Bracco, A. Bürger, L. Caceres, F. Camera, S. Chmel, F. C. Crespi, H. Geissel, J. Gerl, M. Górska, J. Gre bosz, H. Hübel, M. Kavatsyuk, O. Kavatsyuk, M. Kmiecik, I. Kojouharov, N. Kurz, R. Lozeva, A. Maj, S. Mandal, W. Meczynski, B. Million, Z. Podolyák, A. Richard, N. Saito, H. Schaffner, M. Seidlitz, T. Striepling, J. Walker, N. Warr, H. Weick, O. Wieland, M. Winkler, and H. J. Wollersheim, "Lifetime effects for high-resolution gamma-ray spectroscopy at relativistic energies and their implications for the RISING spectrometer," *Nuclear Instruments and Methods in Physics Research, Section A: Accelerators, Spectrometers, Detectors and Associated Equipment*, vol. 613, no. 2, pp. 218–225, 2010.

[64] P. J. Nolan and J. F. Sharpey-Schafer, "The measurement of the lifetimes of excited nuclear states," 1979.

[65] C. Stahl, J. Leske, M. Lettmann, and N. Pietralla, "APCAD—Analysis program for the continuous-angle DSAM," *Computer Physics Communications*, vol. 214, pp. 174–198, 2017.

[66] M. Shamsuzzoha Basunia and A. Chakraborty, "Nuclear data sheets for a=23," *Nuclear Data Sheets*, vol. 171, pp. 1–252, 2021. [Online]. Available: https://www.sciencedirect.com/science/article/pii/S0090375220300582

[67] C. S. Sumithrarachchi, D. J. Morrissey, B. A. Brown, A. D. Davies, D. A. Davies, M. Fancina, E. Kwan, P. F. Mantica, M. Portillo, Y. Shimbara, J. Stoker, and R. R. Weerasiri, "Structure of F23 via β decay of O23," *Physical Review C - Nuclear Physics*, vol. 75, no. 2, pp. 1–8, 2007.

[68] S. Michimasa, S. Shimoura, H. Iwasaki, M. Tamaki, S. Ota, N. Aoi, H. Baba, N. Iwasa, S. Kanno, S. Kubono, K. Kurita, M. Kurokawa, T. Minemura, T. Motobayashi, M. Notani, H. J. Ong, A. Saito, H. Sakurai, E. Takeshita, S. Takeuchi, Y. Yanagisawa, and A. Yoshida, "Proton single-particle states in the neutron-rich 23F nucleus," *Physics Letters, Section B: Nuclear, Elementary Particle and High-Energy Physics*, vol. 638, no. 2-3, pp. 146–152, 2006.

[69] B. Pietras, "Spectroscopy of neutron-rich oxygen and fluorine nuclei via single-neutron knockout reactions," *Thesis*, 2009.

[70] S. Heil, "Electromagnetic Properties of O and the Self-Calibration of Compton Tracking Arrays," *Thesis*, 2019.

[71] D. J. Morrissey, B. M. Sherrill, M. Steiner, A. Stolz, and I. Wiedenhoever, "Commissioning the A1900 projectile fragment separator," *Nuclear Instruments and Methods in Physics Research, Section B: Beam Interactions with Materials and Atoms*, vol. 204, pp. 90–96, 2003.

[72] A. Stolz, T. Baumann, T. N. Ginter, D. J. Morrissey, M. Portillo, B. M. Sherrill, M. Steiner, and J. W. Stetson, "Production of rare isotope beams with the NSCL fragment separator," *Nuclear Instruments and Methods in Physics Research, Section B: Beam Interactions with Materials and Atoms*, vol. 241, no. 1-4, pp. 858–861, 2005.

[73] D. Bazin, J. A. Caggiano, B. M. Sherrill, J. Yurkon, and A. Zeller, "The S800 spectrograph," *Nuclear Instruments and Methods in Physics Research, Section B: Beam Interactions with Materials and Atoms*, vol. 204, pp. 629–633, 2003.

[74] J. Yurkon, D. Bazin, W. Benenson, D. J. Morrissey, B. M. Sherrill, D. Swan, and R. Swanson, "Focal plane detector for the S800 high-resolution spectrometer," *Nuclear Instruments and Methods in Physics Research, Section A: Accelerators, Spectrometers, Detectors and Associated Equipment*, vol. 422, no. 1-3, pp. 291–295, 1999.

[75] S800 documentation. [Online]. Available: https://wikihost.nscl.msu.edu/S800Doc

[76] D. Weisshaar, D. Bazin, P. C. Bender, C. M. Campbell, F. Recchia, V. Bader, T. Baugher, J. Belarge, M. P. Carpenter, H. L. Crawford, M. Cromaz, B. Elman, P. Fallon, A. Forney, A. Gade, J. Harker, N. Kobayashi, C. Langer, T. Lauritsen, I. Y. Lee, A. Lemasson, B. Longfellow, E. Lunderberg, A. O. Macchiavelli, K. Miki, S. Momiyama, S. Noji, D. C. Radford, M. Scott, J. Sethi, S. R. Stroberg, C. Sullivan, R. Titus, A. Wiens, S. Williams, K. Wimmer, and S. Zhu, "The performance of the γ-ray tracking array GRETINA for γ-ray spectroscopy with fast beams of rare isotopes," *Nuclear Instruments and Methods in Physics Research, Section A: Accelerators, Spectrometers, Detectors and Associated Equipment*, vol. 847, no. November 2016, pp. 187–198, 2017. [Online]. Available: http://dx.doi.org/10.1016/j.nima.2016.12.001

[77] T. Lauritsen, A. Korichi, S. Zhu, A. N. Wilson, D. Weisshaar, J. Dudouet, A. D. Ayangeakaa, M. P. Carpenter, C. M. Campbell, E. Clément, H. L. Crawford, M. Cromaz, P. Fallon, J. P. Greene, R. V. Janssens, T. L. Khoo, N. Lalović, I. Y. Lee, A. O. Macchiavelli, R. M. Perez-Vidal, S. Pietri, D. C. Radford, D. Ralet, L. A. Riley, D. Seweryniak, and O. Stezowski, "Characterization of a gamma-ray tracking array: A comparison of GRETINA and Gammasphere using a 60Co source," *Nuclear Instruments and Methods in Physics Research, Section A: Accelerators, Spectrometers, Detectors and Associated Equipment*, vol. 836, pp. 46–56, 2016.

[78] S. Paschalis, I. Y. Lee, A. O. MacChiavelli, C. M. Campbell, M. Cromaz, S. Gros, J. Pavan, J. Qian, R. M. Clark, H. L. Crawford, D. Doering, P. Fallon, C. Lionberger, T. Loew, M. Petri, T. Stezelberger, S. Zimmermann, D. C. Radford, K. Lagergren, D. Weisshaar, R. Winkler,

T. Glasmacher, J. T. Anderson, and C. W. Beausang, "The performance of the Gamma-Ray Energy Tracking In-beam Nuclear Array GRETINA," *Nuclear Instruments and Methods in Physics Research, Section A: Accelerators, Spectrometers, Detectors and Associated Equipment*, vol. 709, pp. 44–55, 2013. [Online]. Available: http://dx.doi.org/10.1016/j.nima.2013.01.009

[79] S. Akkoyun, A. Algora, B. Alikhani, F. Ameil, G. de Angelis, L. Arnold, A. Astier, A. Ataç, Y. Aubert, C. Aufranc, A. Austin, S. Aydin, F. Azaiez, S. Badoer, D. Balabanski, D. Barrientos, G. Baulieu, R. Baumann, D. Bazzacco, F. Beck, T. Beck, P. Bednarczyk, M. Bellato, M. Bentley, G. Benzoni, R. Berthier, L. Berti, R. Beunard, G. Lo Bianco, B. Birkenbach, P. Bizzeti, A. Bizzeti-Sona, F. Le Blanc, J. Blasco, N. Blasi, D. Bloor, C. Boiano, M. Borsato, D. Bortolato, A. Boston, H. Boston, P. Bourgault, P. Boutachkov, A. Bouty, A. Bracco, S. Brambilla, I. Brawn, A. Brondi, S. Broussard, B. Bruyneel, D. Bucurescu, I. Burrows, A. Bürger, S. Cabaret, B. Cahan, E. Calore, F. Camera, A. Capsoni, F. Carrió, G. Casati, M. Castoldi, B. Cederwall, J.-L. Cercus, V. Chambert, M. El Chambit, R. Chapman, L. Charles, J. Chavas, E. Clément, P. Cocconi, S. Coelli, P. Coleman-Smith, A. Colombo, S. Colosimo, C. Commeaux, D. Conventi, R. Cooper, A. Corsi, A. Cortesi, L. Costa, F. Crespi, J. Cresswell, D. Cullen, D. Curien, A. Czermak, D. Delbourg, R. Depalo, T. Descombes, P. Désesquelles, P. Detistov, C. Diarra, F. Didierjean, M. Dimmock, Q. Doan, C. Domingo-Pardo, M. Doncel, F. Dorangeville, N. Dosme, Y. Drouen, G. Duchêne, B. Dulny, J. Eberth, P. Edelbruck, J. Egea, T. Engert, M. Erduran, S. Ertürk, C. Fanin, S. Fantinel, E. Farnea, T. Faul, M. Filliger, F. Filmer, C. Finck, G. de France, A. Gadea, W. Gast, A. Geraci, J. Gerl, R. Gernhäuser, A. Giannatiempo, A. Giaz, L. Gibelin, A. Givechev, N. Goel, V. González, A. Gottardo, X. Grave, J. Gre¸bosz, R. Griffiths, A. Grint, P. Gros, L. Guevara, M. Gulmini, A. Görgen, H. Ha, T. Habermann, L. Harkness, H. Harroch, K. Hauschild, C. He, A. Hernández-Prieto, B. Hervieu, H. Hess, T. Hüyük, E. Ince, R. Isocrate, G. Jaworski, A. Johnson, J. Jolie, P. Jones, B. Jonson, P. Joshi, D. Judson, A. Jungclaus, M. Kaci, N. Karkour, M. Karolak, A. Kaşkaş, M. Kebbiri, R. Kempley, A. Khaplanov, S. Klupp, M. Kogimtzis, I. Kojouharov, A. Korichi, W. Korten, T. Kröll, R. Krücken, N. Kurz, B. Ky, M. Labiche, X. Lafay, L. Lavergne, I. Lazarus, S. Leboutelier, F. Lefebvre, E. Legay, L. Legeard, F. Lelli, S. Lenzi, S. Leoni, A. Lermitage, D. Lersch, J. Leske, S. Letts, S. Lhenoret, R. Lieder, D. Linget, J. Ljungvall, A. Lopez-Martens, A. Lotodé, S. Lunardi, A. Maj, J. van der Marel, Y. Mariette, N. Marginean, R. Marginean, G. Maron, A. Mather, W. Me¸czyński, V. Mendéz, P. Medina, B. Melon, R. Menegazzo, D. Mengoni, E. Merchan, L. Mihailescu, C. Michelagnoli, J. Mierzejewski, L. Milechina, B. Million, K. Mitev, P. Molini, D. Montanari, S. Moon, F. Morbiducci, R. Moro, P. Morrall, O. Möller, A. Nannini, D. Napoli, L. Nelson, M. Nespolo, V. Ngo, M. Nicoletto, R. Nicolini, Y. Le Noa, P. Nolan, M. Norman, J. Nyberg, A. Obertelli, A. Olariu, R. Orlandi, D. Oxley, C. Özben, M. Ozille, C. Oziol, E. Pachoud, M. Palacz, J. Palin, J. Pancin, C. Parisel, P. Pariset, G. Pascovici, R. Peghin, L. Pellegri, A. Perego, S. Perrier, M. Petcu, P. Petkov, C. Petrache, E. Pierre, N. Pietralla, S. Pietri, M. Pignanelli, I. Piqueras, Z. Podolyak, P. Le Pouhalec, J. Pouthas, D. Pugnére, V. Pucknell, A. Pullia, B. Quintana, R. Raine, G. Rainovski, L. Ramina, G. Rampazzo, G. La Rana, M. Rebeschini, F. Recchia,

N. Redon, M. Reese, P. Reiter, P. Regan, S. Riboldi, M. Richer, M. Rigato, S. Rigby, G. Ripamonti, A. Robinson, J. Robin, J. Roccaz, J.-A. Ropert, B. Rossé, C. Rossi Alvarez, D. Rosso, B. Rubio, D. Rudolph, F. Saillant, E. Şahin, F. Salomon, M.-D. Salsac, J. Salt, G. Salvato, J. Sampson, E. Sanchis, C. Santos, H. Schaffner, M. Schlarb, D. Scraggs, D. Seddon, M. Şenyiğit, M.-H. Sigward, G. Simpson, J. Simpson, M. Slee, J. Smith, P. Sona, B. Sowicki, P. Spolaore, C. Stahl, T. Stanios, E. Stefanova, O. Stézowski, J. Strachan, G. Suliman, P.-A. Söderström, J. Tain, S. Tanguy, S. Tashenov, C. Theisen, J. Thornhill, F. Tomasi, N. Toniolo, R. Touzery, B. Travers, A. Triossi, M. Tripon, K. Tun-Lanoë, M. Turcato, C. Unsworth, C. Ur, J. Valiente-Dobon, V. Vandone, E. Vardaci, R. Venturelli, F. Veronese, C. Veyssiere, E. Viscione, R. Wadsworth, P. Walker, N. Warr, C. Weber, D. Weisshaar, D. Wells, O. Wieland, A. Wiens, G. Wittwer, H. Wollersheim, F. Zocca, N. Zamfir, M. Zie¸bliński, and A. Zucchiatti, "Agata—advanced gamma tracking array," *Nuclear Instruments and Methods in Physics Research Section A: Accelerators, Spectrometers, Detectors and Associated Equipment*, vol. 668, pp. 26–58, 2012. [Online]. Available: https://www.sciencedirect.com/science/article/pii/S0168900211021516

[80] V. S. Prasher, M. Cromaz, E. Merchan, P. Chowdhury, H. L. Crawford, C. J. Lister, C. M. Campbell, I. Y. Lee, A. O. Macchiavelli, D. C. Radford, and A. Wiens, "Sensitivity of GRETINA position resolution to hole mobility," *Nuclear Instruments and Methods in Physics Research, Section A: Accelerators, Spectrometers, Detectors and Associated Equipment*, vol. 846, no. November 2016, pp. 50–55, 2017. [Online]. Available: http://dx.doi.org/10.1016/j.nima.2016.11.038

[81] A. Lopez-Martens, K. Hauschild, A. Korichi, J. Roccaz, and J. Thibaud, "γ-ray tracking algorithms: a comparison," *Nuclear Instruments and Methods in Physics Research Section A: Accelerators, Spectrometers, Detectors and Associated Equipment*, vol. 533, no. 3, pp. 454–466, 2004.

[82] G. Schmid, M. Deleplanque, I. Lee, F. Stephens, K. Vetter, R. Clark, R. Diamond, P. Fallon, A. Macchiavelli, and R. MacLeod, "A γ-ray tracking algorithm for the greta spectrometer," *Nuclear Instruments and Methods in Physics Research Section A: Accelerators, Spectrometers, Detectors and Associated Equipment*, vol. 430, no. 1, pp. 69–83, 1999.

[83] J. Van der Marel and B. Cederwall, "Backtracking as a way to reconstruct compton scattered γ-rays," *Nuclear Instruments and Methods in Physics Research Section A: Accelerators, Spectrometers, Detectors and Associated Equipment*, vol. 437, no. 2-3, pp. 538–551, 1999.

[84] GRETINA tools and resources. [Online]. Available: https://greta.lbl.gov/tools-etc

[85] R. Brun and F. Rademakers, "ROOT - An object oriented data analysis framework," *Nuclear Instruments and Methods in Physics Research, Section A: Accelerators, Spectrometers, Detectors and Associated Equipment*, vol. 389, no. 1-2, pp. 81–86, 1997.

[86] Nuclear data sheets. [Online]. Available: http://nucleardata.nuclear.lu.se/

[87] I. Abt, A. Caldwell, K. Kröninger, J. Liu, X. Liu, and B. Majorovits, "Neutron interactions as seen by a segmented germanium detector," *The European Physical Journal A*, vol. 36, no. 2, pp. 139–149, 2008.

[88] K. S. Krane, R. M. Steffen, and R. M. Wheeler, "Directional correlations of gamma radiations emitted from nuclear states oriented by nuclear reactions or cryogenic methods," *Nucl.Data Tables Ser.a*, vol. 11, no. 5, pp. 351–406, 1973.

[89] H. Olliver, T. Glasmacher, and A. E. Stuchbery, "Angular distributions of gamma- rays with intermediate-energy beams," *Physical Review C - Nuclear Physics*, vol. 68, no. 4, p. 14, 2003.

[90] A. E. Stuchbery, "Γ-Ray Angular Distributions and Correlations After Projectile-Fragmentation Reactions," *Nuclear Physics A*, vol. 723, no. 1-2, pp. 69–92, 2003.

[91] S. Stroberg, A. Gade, J. Tostevin, V. Bader, T. Baugher, D. Bazin, J. Berryman, B. Brown, C. Campbell, K. Kemper *et al.*, "Single-particle structure of silicon isotopes approaching si 42," *Physical Review C*, vol. 90, no. 3, p. 034301, 2014.

[92] A. Gade, D. Weisshaar, B. Brown, D. Bazin, K. Brown, R. Charity, P. Farris, A. Hill, J. Li, B. Longfellow *et al.*, "Exploiting dissipative reactions to perform in-beam γ-ray spectroscopy of the neutron-deficient isotopes ca 38, 39," *Physical Review C*, vol. 106, no. 6, p. 064303, 2022.

[93] H. Crawford, A. Macchiavelli, P. Fallon, M. Albers, V. Bader, D. Bazin, C. Campbell, R. Clark, M. Cromaz, J. Dilling *et al.*, "Unexpected distribution of ν 1 f 7/2 strength in ca 49," *Physical Review C*, vol. 95, no. 6, p. 064317, 2017.

[94] K. Yurkewicz, D. Bazin, B. Brown, J. Enders, A. Gade, T. Glasmacher, P. Hansen, V. Maddalena, A. Navin, B. Sherrill *et al.*, "One-neutron knockout from ni 57," *Physical Review C*, vol. 74, no. 2, p. 024304, 2006.

[95] M. Spieker, A. Gade, D. Weisshaar, B. Brown, J. Tostevin, B. Longfellow, P. Adrich, D. Bazin, M. Bentley, J. Brown *et al.*, "One-proton and one-neutron knockout reactions from n= z= 28 ni 56 to the a= 55 mirror pair co 55 and ni 55," *Physical Review C*, vol. 99, no. 5, p. 051304, 2019.

[96] S. Agostinelli, J. Allison, K. Amako, J. Apostolakis, H. Araujo, P. Arce, M. Asai, D. Axen, S. Banerjee, G. Barrand, F. Behner, L. Bellagamba, J. Boudreau, L. Broglia, A. Brunengo, H. Burkhardt, S. Chauvie, J. Chuma, R. Chytracek, G. Cooperman, G. Cosmo, P. Degtyarenko, A. Dell'Acqua, G. Depaola, D. Dietrich, R. Enami, A. Feliciello, C. Ferguson, H. Fesefeldt, G. Folger, F. Foppiano, A. Forti, S. Garelli, S. Giani, R. Giannitrapani, D. Gibin, J. J. Gomez Cadenas, I. Gonzalez, G. Gracia Abril, G. Greeniaus, W. Greiner, V. Grichine, A. Grossheim, S. Guatelli, P. Gumplinger, R. Hamatsu, K. Hashimoto, H. Hasui, A. Heikkinen, A. Howard, V. Ivanchenko, A. Johnson, F. W. Jones, J. Kallenbach, N. Kanaya, M. Kawabata, Y. Kawabata, M. Kawaguti, S. Kelner, P. Kent, A. Kimura, T. Kodama, R. Kokoulin, M. Kossov, H. Kurashige, E. Lamanna, T. Lampen, V. Lara, V. Lefebure, F. Lei, M. Liendl, W. Lockman, F. Longo, S. Magni, M. Maire, E. Medernach, K. Minamimoto, P. Mora de Freitas, Y. Morita, K. Murakami, M. Nagamatu, R. Nartallo, P. Nieminen,

T. Nishimura, K. Ohtsubo, M. Okamura, S. O'Neale, Y. Oohata, K. Paech, J. Perl, A. Pfeiffer, M. G. Pia, F. Ranjard, A. Rybin, S. Sadilov, E. di Salvo, G. Santin, T. Sasaki, N. Savvas, Y. Sawada, S. Scherer, S. Sei, V. Sirotenko, D. Smith, N. Starkov, H. Stoecker, J. Sulkimo, M. Takahata, S. Tanaka, E. Tcherniaev, E. Safai Tehrani, M. Tropeano, P. Truscott, H. Uno, L. Urban, P. Urban, M. Verderi, A. Walkden, W. Wander, H. Weber, J. P. Wellisch, T. Wenaus, D. C. Williams, D. Wright, T. Yamada, H. Yoshida, and D. Zschiesche, "GEANT4 - A simulation toolkit," *Nuclear Instruments and Methods in Physics Research, Section A: Accelerators, Spectrometers, Detectors and Associated Equipment*, vol. 506, no. 3, pp. 250–303, 2003.

[97] P. Adrich, D. Enderich, D. Miller, V. Moeller, R. P. Norris, K. Starosta, C. Vaman, P. Voss, and A. Dewald, "A simulation tool for Recoil Distance Method lifetime measurements at NSCL," *Nuclear Instruments and Methods in Physics Research, Section A: Accelerators, Spectrometers, Detectors and Associated Equipment*, vol. 598, no. 2, pp. 454–464, 2009.

[98] E. Sauvan, F. Carstoiu, N. A. Orr, J. C. Angélique, W. N. Catford, N. M. Clarke, M. Mac Cormick, N. Curtis, M. Freer, S. Grévy, C. Le Brun, M. Lewitowicz, E. Liégard, F. M. Marqués, P. Roussel-Chomaz, M. G. Saint Laurent, M. Shawcross, and J. S. Winfield, "One-neutron removal reactions on neutron-rich psd-shell nuclei," *Physics Letters, Section B: Nuclear, Elementary Particle and High-Energy Physics*, vol. 491, no. 1-2, pp. 1–7, 2000.

[99] Michimasa, "Michimasa PhD Thesis, "Proton Shell structure in Neutron-Rich Nucleus 23F", 2006."

[100] S. Takeuchi, T. Motobayashi, Y. Togano, M. Matsushita, N. Aoi, K. Demichi, H. Hasegawa, and H. Murakami, "Dali2: A nai (tl) detector array for measurements of γ rays from fast nuclei," *Nuclear Instruments and Methods in Physics Research Section A: Accelerators, Spectrometers, Detectors and Associated Equipment*, vol. 763, pp. 596–603, 2014.

[101] F. Azaiez, "Exogam: a γ-ray spectrometer for radioactive beams," *Nuclear Physics A*, vol. 654, no. 1, pp. 1003c–1008c, 1999.

[102] A. Magilligan and B. Brown, "New isospin-breaking "usd" hamiltonians for the sd shell," *Physical Review C*, vol. 101, no. 6, p. 064312, 2020.

[103] "Alex Brown, NSCL, private communications."

[104] B. Brown and W. Rae, "The shell-model code nushellx@ msu," *Nuclear Data Sheets*, vol. 120, pp. 115–118, 2014.

[105] A. Signoracci and B. A. Brown, "Proton single-particle energies in F23," *Physical Review C - Nuclear Physics*, vol. 75, no. 2, 2007.

[106] F. Azaiez, M. Belleguic, D. Sohler, M. Stanoiu, Z. Dombradi, O. Sorlin, J. Timar, F. Amorini, D. Baiborodin, A. Bauchet *et al.*, "Probing shell structure in neutron-rich nuclei with in-beam γ-spectroscopy," *The European Physical Journal A*, vol. 15, no. 1, pp. 93–97, 2002.

[107] A. Gavron, "Statistical model calculations in heavy ion reactions," *Phys. Rev. C*, vol. 21, pp. 230–236, 1980.

[108] O. B. Tarasov and D. Bazin, "LISE++: Radioactive beam production with in-flight separators," *Nuclear Instruments and Methods in Physics Research, Section B: Beam Interactions with Materials and Atoms*, vol. 266, no. 19-20, pp. 4657–4664, 2008. [Online]. Available: http://dx.doi.org/10.1016/j.nimb.2008.05.110

[109] L. M. Bollinger, "Argonne tandem-linac accelerator system," Argonne National Lab., IL (USA), Tech. Rep., 1983.

[110] W. F. Henning, "The ATLAS Facility at Argonne National Laboratory," *Nuclear Physics News*, vol. 5, no. 3, pp. 12–22, 1995.

[111] M. Paul, D. Berkovits, I. Ahmad, F. Borasi, J. Caggiano, C. N. Davids, J. P. Greene, B. Harss, A. Heinz, D. J. Henderson, W. Henning, C. L. Jiang, R. C. Pardo, K. E. Rehm, R. Rejoub, D. Seweryniak, A. Sonzogni, J. Uusitalo, and R. Vondrasek, "AMS of heavy elements with an ECR ion source and the ATLAS linear accelerator," *Nuclear Instruments and Methods in Physics Research, Section B: Beam Interactions with Materials and Atoms*, vol. 172, no. 1-4, pp. 688–692, 2000.

[112] D. P. Moehs, R. Vondrasek, R. H. Scott, R. C. Pardo, and J. M. Montgomery, "Completion of the ATLAS ECR-I ion source upgrade project," *Review of Scientific Instruments*, vol. 73, no. 2 II, p. 576, 2002.

[113] H. M. David, "Study of the N=Z nucleus Ga using a new fast beta-decay tagging system," 2013.

[114] ATLAS website. [Online]. Available: https://www.anl.gov/atlas/

[115] L. M. Bollinger, R. C. Pardo, K. W. Shepard, P. J. Billquist, J. M. Bogaty, B. E. Clifft, R. Harkewicz, F. H. Munson, J. A. Nolen, and G. P. Zinkann, "The positive-ion injector of ATLAS: design and operating experience," *Nuclear Inst. and Methods in Physics Research, B*, vol. 79, no. 1-4, pp. 753–757, 1993.

[116] M. Mathy, "Electromagnetic Properties of Light Neutron-Rich Nuclei - Lifetime Measurements of 16C and 23Ne," *Thesis*, 2020.

[117] R. Pardo and G. Zinkann, "Long-term operating experience for the atlas superconducting resonators," Argonne National Lab., IL (US), Tech. Rep., 1999.

[118] C. N. Davids and J. D. Larson, "The argonne fragment mass analyzer," *Nuclear Inst. and Methods in Physics Research, B*, vol. 40-41, no. PART 2, pp. 1224–1228, 1989.

[119] C. N. Davids, B. B. Back, K. Bindra, D. J. Henderson, W. Kutschera, T. Lauritsen, Y. Nagame, P. Sugathan, A. V. Ramayya, and W. B. Walters, "Startup of the Fragment Mass Analyzer at ATLAS," *Nuclear Inst. and Methods in Physics Research, B*, vol. 70, no. 1-4, pp. 358–365, 1992.

[120] B. B. Back, D. J. Blumenthal, C. N. Davids, D. J. Henderson, R. H. Hermann, C. L. Jiang, H. T. Penttilä, and A. H. Wuosmaa, "Transport efficiency of the Argonne fragment mass analyzer," *Nuclear Instruments and Methods in Physics Research, Section A: Accelerators, Spectrometers, Detectors and Associated Equipment*, vol. 379, no. 2, pp. 206–211, 1996.

[121] C. N. Davids, B. Back, M. Carpenter, M. Freer, D. Henderson, R. Henry, R. V. Janssens, T. Khoo, T. Lauritsen, Y. Liang *et al.*, "Research at the fragment mass analyzer at atlas," Argonne National Lab., IL (United States), Tech. Rep., 1993.

[122] FMA PPAC documentation. [Online]. Available: https://www.phy.anl.gov/fma/ppac.html

[123] FMA IC documentation. [Online]. Available: https://www.phy.anl.gov/fma/ic.html

[124] D. Schumann, T. Stowasser, R. Dressler, and M. Ayranov, "Possibilities of preparation of exotic radionuclide samples at PSI for scientific investigations," *Radiochimica Acta*, vol. 101, no. 8, pp. 501–508, 2013.

[125] D. Schumann, J. Neuhausen, S. Horn, P. W. Kubik, and I. Günther-Leopold, "Radiochemical separation and analytical determination of 10Be from proton-irradiated graphite targets," *Radiochimica Acta*, vol. 96, no. 1, pp. 31–34, 2008.

[126] S. Heinitz, D. Kiselev, N. Kivel, and D. Schumann, "Separation of weighable amounts of 10Be from proton irradiated graphite," *Applied Radiation and Isotopes*, vol. 130, no. July, pp. 260–263, 2017. [Online]. Available: https://doi.org/10.1016/j.apradiso.2017.10.012

[127] A. Stolarz, "Target preparation for research with charged projectiles," *Journal of Radioanalytical and Nuclear Chemistry*, vol. 299, no. 2, pp. 913–931, 2014.

[128] PSI target manufacturing documentation. [Online]. Available: https://www.psi.ch/en/lrc/target-manufacturing

[129] PSI PVD documentation. [Online]. Available: https://www.psi.ch/en/lrc/vapour-deposition

[130] E. A. Maugeri, S. Heinitz, R. Dressler, M. Barbagallo, N. Kivel, D. Schumann, M. Ayranov, A. Musumarra, M. Gai, N. Colonna, M. Paul, S. Halfon, L. Cosentino, P. Finocchiaro, and A. Pappalardod, "Preparation of 7Be targets for nuclear astrophysics research," *Journal of Instrumentation*, vol. 12, no. 2, 2017.

[131] DOSTAL DOSY documentation. [Online]. Available: http://www.dostal-gmbh.com/en/product/dostal-dosy

[132] PSI droplet deposition documentation. [Online]. Available: https://www.psi.ch/en/lrc/droplet-deposition

[133] R. D. Deegan, O. Bakajin, T. F. Dupont, G. Huber, S. R. Nagel, and T. A. Witten, "Capillary flow as the cause of ring stains from dried liquid drops," *Nature*, vol. 389, no. 6653, pp. 827–829, 1997.

[134] D. Zang, S. Tarafdar, Y. Y. Tarasevich, M. Dutta Choudhury, and T. Dutta, "Evaporation of a droplet: From physics to applications," *Physics Reports*, vol. 804, pp. 1–56, 2019, evaporation of a Droplet: From physics to applications. [Online]. Available: https://www.sciencedirect.com/science/article/pii/S0370157319300468

[135] W. Parker and R. Falk, "Molecular plating: A method for the electrolytic formation of thin inorganic films," *Nuclear Instruments and Methods*, vol. 16, no. C, pp. 355–357, 1962.

[136] PSI molecular plating documentation. [Online]. Available: https://www.psi.ch/en/lrc/molecular-plating

[137] A. Vascon, "Molecular plating of thin lanthanide layers with improved material properties for nuclear applications," p. 188, 2013.

[138] "Emilio A. Maugeri, PSI, private communications."

[139] Goodfellow foil specifications. [Online]. Available: https://www.goodfellow.com/uk/en-gb/foil

[140] J. Perrière, "Rutherford backscattering spectrometry," *Vacuum*, vol. 37, no. 5, pp. 429–432, 1987. [Online]. Available: https://www.sciencedirect.com/science/article/pii/0042207X87903277

[141] W. Chu and J. Liu, "Rutherford backscattering spectrometry: reminiscences and progresses," *Materials Chemistry and Physics*, vol. 46, no. 2, pp. 183–188, 1996. [Online]. Available: https://www.sciencedirect.com/science/article/pii/S0254058497800120

[142] Dalton nuclear institute. [Online]. Available: https://www.dalton.manchester.ac.uk/research/

[143] "Samir de Moraes Shubeita, Dalton, Private communications."